

---

---



---

---

---

# Contents

<b>Table of Contents</b>	i
<b>List of Figures</b>	ii
<b>List of Tables</b>	v
<b>1 Introduction</b>	1
<b>2 Silicon Vacancy Centers in Diamond</b>	5
2.1 Diamond as a host lattice . . . . .	5
2.2 Classification of diamond . . . . .	6
2.2.1 Classification by impurities . . . . .	6
2.2.2 Classification by crystallinity . . . . .	7
2.3 Silicon-vacancy center . . . . .	8
2.3.1 Luminescence properties . . . . .	9
<b>3 Photoluminescence Setup</b>	15
3.1 Confocal Setup . . . . .	15
3.2 Surface Imaging . . . . .	17
3.3 Spectrometer . . . . .	18
3.4 HBT . . . . .	18
<b>4 Fabrication of Nanodiamonds</b>	21
4.1 HPHT . . . . .	22
4.2 CVD . . . . .	22
4.3 Wet-Milling . . . . .	24
4.3.1 Wet-Milled HPHT Nanodiamonds . . . . .	25
4.3.2 Wet-Milled CVD Nanodiamonds . . . . .	26
4.3.3 Doubly Wet-Milled Implanted Nanodiamonds Implanted With Silicon .	26
4.4 Iridium Substrate . . . . .	28
4.4.1 Preparation of The Substrate . . . . .	29
4.5 Listing of available samples . . . . .	30
<b>5 Quality of Nanodiamonds</b>	31
5.1 Quality-improving Post-Processing Treatments . . . . .	32
5.1.1 Annealing and Oxidation . . . . .	32
5.1.2 Surface Treatment With Gas And Plasma . . . . .	32
5.2 Raman Measurements . . . . .	33

5.2.1	Surface Contamination . . . . .	34
5.2.2	Defect Concentration . . . . .	35
5.2.3	Lattice Strain . . . . .	35
5.3	Transmission Electron Spectroscopy Measurements . . . . .	36
5.3.1	Crystallinity and Grain Boundaries . . . . .	36
<b>6</b>	<b>Spectral Distribution</b>	<b>38</b>
6.1	Photoluminescence spectra . . . . .	38
6.1.1	Zero-phonon-line . . . . .	38
6.1.2	Sideband . . . . .	43
6.1.3	Cryostatic Measurements . . . . .	45
6.2	Photon correlation measurements . . . . .	46
6.3	Photostability . . . . .	48
<b>7</b>	<b>Coupling NDs</b>	<b>51</b>
7.1	Additional Experimental Methods . . . . .	51
7.1.1	Nanomanipulator . . . . .	52
7.1.2	Determination of The Position of Nanodiamonds . . . . .	54
7.1.3	The Pick-And-Place Process . . . . .	54
7.2	VCSELs . . . . .	55
7.2.1	Vertical-Cavity Surface Emitting Laser Structure . . . . .	56
7.2.2	SiV center in a Vertical-Cavity Surface Emitting Laser . . . . .	56
7.3	Antennas . . . . .	58
7.3.1	Nanodiamond With Multiple SiV centers Coupled to Antenna . . . . .	58
7.3.2	Nanodiamond With Single SiV center Coupled to Antenna . . . . .	58
<b>Summary and Conclusions</b>		<b>65</b>
<b>Index</b>		<b>65</b>

---

---

# List of Figures

2.1	Face-centered cubic diamond lattice . . . . .	6
2.2	Reduced light extraction efficiency of diamond due to refraction . . . . .	6
2.3	Split-vacancy configuration for SiV centers in diamond . . . . .	9
2.4	Band gap of SiV centers hosted in diamond . . . . .	10
2.5	Huang-Rhys model of vibrational transitions . . . . .	12
2.6	Flourescence spectra of SiV centers at room temperature . . . . .	13
2.7	Flourescence spectra of SiV centers at low temperature . . . . .	14
3.1	Confocal microscopy setup . . . . .	16
3.2	Spectrometer and HBT setup . . . . .	17
4.1	CVD production method . . . . .	23
4.2	Example of CVD nanodiamonds . . . . .	24
4.3	Wet-milling in a vibrational mill . . . . .	25
4.4	Distribution of nanodiamonds ontop of an iridium substrate . . . . .	26
4.5	(a) SEM picture of nanodiamonds sunken into a silicon substrate after annealing at 900 °C for 3 h. Magnification 20 000. (b) SEM image of the microdiamonds after milling on an iridium substrate, but before implantation. In the middle of the picture, there is a reference cross milled into the iridium substrate with a focused ion beam. Its size amounts to 10 µm. It can be seen, that the microdiamonds exhibit sizes of a few micrometer. . . . .	27
4.6	(a) Microscope image of a drop of water on an iridium substrate cleaned with Piranha etch. This picture was used to estimate the contact angle. (b) SEM picture of an 60 nm iridium layer that peeled off the substrate after an ultrasonic bath. . . . .	28
5.1	Raman spectrum of a single nanodiamond . . . . .	34
5.2	TEM imaging of a single nanodiamond . . . . .	36
6.1	Spectral distribution of SiV center ZPLs . . . . .	39
6.2	Sample SiV center photoluminescence spectra for group V and group H . . . . .	40
6.3	Comparison of obtained SiV center linewidths with available data sources . . . . .	41
6.4	Zoom-in onto SiV centers of the group V . . . . .	42
6.5	Calculated dependence between SiV center ZPL and lattice pressure . . . . .	43
6.6	Side band peaks for SiV centers . . . . .	44
6.7	Shift of dominant side band peaks for SiV centers . . . . .	45
6.8	todo fix figure . . . . .	45
6.9	todo fix figure . . . . .	46

6.10	Intensity autocorrelation measurements for group H and group V . . . . .	47
6.11	Time trace of a single emitter. . . . .	48
6.12	Distributions of brigth and dark state intervals . . . . .	49
7.1	(a) Sketch of the pick-and-place process exploiting a nanomanipulator. (b) Image of the nanomanipulator mounted in the FIB. The arrows indicate the degrees of freedom of motion of the nanomanipulator. The custom made work-bench is situated in the middle of the picture. On top of it, there is a $1\text{ cm}^2$ substrate with coated nanodiamonds, the nanomanipulator tip pointing to the middle of it. Behind it, there is the target vertical-cavity surface emitting laser. Perpendicular to the workbench, the objective of the electron microscope can be seen. The pointier cone perpendicular to the image top image edge is the objective of the focussed ion beam. . . . .	53
7.2	(a) Overview of a field of cross markers. The field spans $0.5 \times 0.5\text{ mm}$ (b) White light scan of an area with a cross marker in all four corners. . . . .	53
7.3	ask how to cite	55
7.4	(a) Sketch of the VCSEL showing the different layers.	
	(b) Image of the VCSEL. The circle with the black dots is the hole in the p-contact (diameter $D_s$ , the smaller darker area in the middle is the laser output area (diameter $D_A$ ) . . . . .	56
7.5	(a) Emission spectrum of the used VCSEL at two different currents. (b) Optical output power and voltage of the same VCSEL in dependence of input current. []	57
7.6	(a) SEM image of an array of VCSELs. The three wires are the anodes, which are connected to the top layer (p-contact) of the VCSEL. Therefore, three of the VCSEL structures can be operated. (b) Detail SEM image of the top of the exploited VCSEL Bm4. The circular middle part is the hole in the p-contact through which the top DBR is visible. The active diameter is smaller than that and not visible in the SEM. . . . .	57
7.7	(a) Scan of the VCSEL Bm4 with coupled nanodiamond under excitation with the laser from the confocal setup. The big visible ring is the edge of the cirular hole in the p-contact. The bright spot in the upper left corner corresponds to the transferred nanodiamond containing an SiV center. (b) Scan of the VCSEL Bm2 without nanodiamond under excitation with the laser from the confocal setup. The cirular hole in the p-contact exhibits a constant countrate. . . . .	58
7.8	(a) Spectrum of the preselected diamond for transfer onto VCSEL Bm4 before pick-and-place. The strong line denoted A exhibits a center wavelength of 746.0 nm and a linewidth of 1.9 nm. Line B exhibits a center wavelength of 0 nm and a linewidth of 0 nm put in correct numbers	
	(b) Spectrum of the same SiV center after pick-and-place, excited with the same laser as before. While Line A is almost gone, line B still exists and ist the predominant line of the spectrum. Note: different longpass filters were used for the two measurements. Measurement (a) was performed with a 720 nm longpass filter, measurement (b) with a 710 nm longpass filter. . . . .	59

7.9	(a) Scan of the laser light stemming from the VCSEL Bm4 and the fluorescence light light from the SiV center in the filter window 730 nm to 750 nm. (b) Scan of the laser light stemming from the VCSEL Bm2 without coupled SiV center. The outcome of the two scans is almost identical. . . . .	59
7.10	Reflectivity of the Distributed Bragg reflector (DBR) of the VCSEL, and spectrum of the SiV center measured during VCSEL excitation. The reflectivity of the DBR and the VCSEL emission spectra are depicted with different scales. The shape of the measurement of the SiV center during VCSEL operation coincides with the shape of the DBR reflectivity. The spectrum of the SiV center is not visible. As the emission from the SiV center is small compared to the intensity of the laser sideband in the same wavelength regime, the SiV centers emission is not detectable. . . . .	60
7.12	<caption> . . . . .	61
7.13	<caption> . . . . .	61
7.14	. . . . .	62
7.15	<caption> . . . . .	62
7.16	<caption> . . . . .	62
7.17	<caption> . . . . .	63
7.18	<caption> . . . . .	63
7.19	<caption> . . . . .	63
7.20	<caption> . . . . .	64
7.21	<caption> . . . . .	64
7.22	<caption> . . . . .	64

---

---

# List of Tables

2.1	Classification of diamond synthesized by chemical vapor deposition . . . . .	8
4.1	Samples grown with diamondoid seeds . . . . .	24
4.2	Listing of available wet-milled samples . . . . .	30

---

---

# Chapter 1

## Introduction

“Every competent physicist can “do” quantum mechanics, but the stories we tell ourselves about what we are doing are as various as the tales of Sheherazade, and almost as implausible.”

David J. Griffiths

The International System of Units (SI, abbreviated from the French Système international d’unités) emerged in the late 18<sup>th</sup> century as a coherent metric system of measurement with rationally related units and simple rules for combining them [?]. Since its inception it was improved and augmented continuously in an ongoing effort to accommodate continued scientific and technological progress. The current SI system is comprised of seven base units: The kilogram (kg), the second (s), the Ampere (A), the Kelvin (K), the mole (mol) and the candela (cd). Currently a redefinition of four of base units (kilogram, mole, Kelvin, Ampere) in terms of fundamental constants is under way [?, ?, ?]. The proposed change will improve the definitions of these base units to make them easier to realize experimentally, particularly for the measurement of electrical quantities [?]. It will also eliminate the last remaining base unit definition which relies on a historic material artefact, the international prototype of the kilogram. As a result all base units will, for the first time, be tied to one or more fundamental constants of nature.

As these developments are put into motion, similar discussions regarding the SI base unit for luminous intensity, the candela, have emerged. It has been suggested that it can be improved by leveraging recent advances in classical radiometry and photometry as well as the development of novel quantum devices and techniques [?].

At the time of writing the definition of the candela read:

The candela is the luminous intensity, in a given direction, of a source that emits monochromatic radiation of frequency  $540 \times 10^{12}$  Hz and that has a radiant intensity in that direction of  $638^{-1} \text{W sr}^{-1}$ .

Traditional applications relying on this definition in conjunction with accurate photometric and radiometric measurements are light design, manufacturing and use of optical sources, detectors, optical components, colored materials and optical radiation measuring equipment [?]. In the classical regime of optical radiation high flux levels dominate. Here primary optical radiation scales for sources and detectors are generally based on cryogenic radiometry estab-

lishing a link to the SI units of electricity [?]. Other calculable sources such as synchrotrons and blackbody radiators can serve as primary source scales in the ultraviolet and deep-UV regions by establishing traceability to SI units of thermometry, electricity and length [?, ?].

Scaling down to the quantum world of radiometry is associated with a loss of measurement accuracy. In this regime dedicated photon counting techniques are required to deal with the challenge of low flux levels. Since they rely on counting photons directly, they can provide efficient and traceable measurements and improved uncertainties. For high-accuracy absolute radiometry in this regime predictable single or quasi-single-photon sources and photon detectors as well as associated new quantum-based calibration methods and standards are called for. To promote the development of such technologies a reformulation of the candela has been proposed in terms of *countable* photon units [?, ?, ?, ?, ?]. Here we emphasize the distinction between *countable* and *calculable* sources of photons. The latter being available as blackbodies or synchrotron radiators.

A straightforward quantum-based reformulation has been suggested based on [?, ?]:

$$P = nh\nu, \quad (1.1)$$

where the radiant intensity per steradian  $P = 638^{-1}\text{W sr}^{-1}$  in a given direction and the photon frequency  $\nu = 540 \times 10^{12}\text{ Hz}$  are assumed to be exact with their numerical values inherited from the present definition of the candela. The anticipated proposed changes to the SI system will define Planck's constant  $h = 6.626\ 070\ 15 \times 10^{-34}\text{ J s}$  as an exact numerical constant [?]. As a consequence the number of photons per second per steradian in a candela  $n$  becomes a constant defined as:

$$n = \frac{P}{h\nu} \approx 4.091\ 942\ 9 \times 10^{15} \text{ counts s}^{-1} \text{ sr}^{-1}. \quad (1.2)$$

Given this definition of the radiant intensity of a candela in terms of countable photons, a possible formulation of the quantum candela could read:

The candela is the luminous intensity, in a given direction, of a source that emits photons of frequency  $540 \times 10^{12}\text{ Hz}$  at a rate of  $4.091\ 942\ 9 \times 10^{15}$  photons per second per steradian in that direction.

This definition would incur a change of 0.0014 % from the current value of the candela, an acceptable change, taking into account the fact that current experimental realizations of the candela are limited to uncertainties of 0.02 % [?]. Proposals such as this are regularly reviewed by the Consultative Committee for Photometry and Radiometry ensuring that the current best measurement practices and existing as well as emerging needs of the user community of the candela are met [?].

While a proposed formulation of a quantum-candela can be considered a small change to the SI system, a shift towards quantum based radiometric SI units is likely to become a critical enabler driving the development of accurate and traceable measurement methods on the single-photon level. In order for the definition of the quantum-candela to have practical meaning, photon counting detectors are required. To ensure proper calibration of such devices, reliable deterministic single photon sources are required. As novel instruments and associated calibration standards emerge, our ability to work with individual photons in a wide range of

applications will improve [?, ?, ?, ?]. The quest for single photon sources is supported by large research projects such as "Single-Photon Sources for Quantum Technology" funded by European Metrology Research Program.

Advances in radiometry are particularly important for fields like quantum communication and quantum computing. They are heavily reliant on deterministic reliable single-photon sources and well-calibrated detectors capable of resolving single photons. As such they have acted as major driving forces in their development [?, ?]. Amongst others, some well known applications include quantum key distribution [?, ?, ?] or transmission in a quantum network [?, ?, ?].

At present several candidates for on-demand single-photon sources are available: One consists of a laser beam attenuated such that the mean number of photons in the beam becomes close to one [?, ?, ?]. However, the mean photon number cannot be controlled perfectly and a non-zero probability remains that multiple photons are present.

Quasi-single photon states can be realized more efficiently using photon-pairs, consisting of a signal and an idler photon. Pairs are created when a photon interacts with a non-linear optical medium in a process called spontaneous parametric down-conversion (SPDC) [?, ?, ?, ?, ?, ?, ?]. The deciding feature of the process is the strong time-correlation between the signal and idler photons. If both photons are injected into individual signal paths, an detection event in one of the paths heralds the existence of a photon in the other path. SPDC pairs can thus be used to construct single-photon sources. Unfortunately, due to the poor efficiency of the SPDC process, the probability of generating pairs is unfavorable [?, ?]. Thus efforts have been undertaken to improve the efficiency [?, ?, ?].

Quantum dots emit photons by recombination of electron-hole pairs created by optical excitation or via an electric current [?, ?, ?]. The choice of semiconducting material determines the electronic structure of the system and thus the characteristics of the emitter. Similarly single-photons can be obtained as a result of radiative transitions between energy levels of single atoms or molecules trapped in an optical cavity [?]. While these sources have desirable properties such as high-collection efficiency, the practical usefulness is limited due to their technological requirements, amongst others a high vaccuum is needed to operate these sources [?].

For a wide range of single photon sources, significant progress has been made towards improving purity, indistinguishability and collection efficiency [?, ?, ?, ?, ?].

However, a single photon source suitable for the calibration of single-photon detectors is difficult to realize [?]. Ideally, a standard single photon source should be emmitting with a quantum efficiency of 100 % indicating that the entire exitation energy is transformed into radiation without losses. At the same time single photons should be emitted with a probability of one and subsequently collected with perfect efficiency.

Very recently, steps towards realizing an ideal deterministic single photon source have been taken. In particular it has been demonstrated that color centers in nanodiamonds involving silicon [?, ?] and nitrogen [?] are promising candidates for the realization of standard single photon sources [?, ?]. Single photon sources were absolutely calibrated by a classical detector and a calibrated spectrometer. Thus a unbroken traceability chain to the SI system has been achieved. The photon flux of the source can be controlled via the settings of the pump laser repetition rate. In this way a direct link between the high photon flux levels of the classical

regime and low photon flux levels in the quantum world has been established. For the nitrogen vacancy center a photon flux rate of  $\approx 1.4 \times 10^5$  photons per second was established.

In this thesis we focus on the silicon-vacancy center hosted in nanodiamond and its properties as a single photon source. In doing so we aim to add momentum to the application of single photon source as high accuracy calibration devices and subsequently, to the development of photon counting detectors and the adoption of the quantum-candela.

The SiV center in diamond is an ideal candidate for single photon calibration purposes. It is very efficient and stable narrow linewidth emitter, emitting single photons with high intensity. Conveniently, SiV centers operate at room temperature under normal pressure and hence do not require extremely sophisticated experimental setups. As an alternative to hosting SiV centers in bulk diamond, they can be implanted in nano-sized diamond grains offering increased collection efficiency. Grains containing individual SiV centers can be identified and preselected according to their properties. As a result individual emitters can be made mobile using pick-and-place techniques. The ability to relocate emitters is convenient since it unlocks applications requiring selected single emitters such as coupling to antennas or the use as hybrid integrated single photon sources in conjunction with vertical-cavity surface-emitting laser (VCLS).

In this thesis we synthesize nanodiamonds with SiV centers using a variety of different techniques. Chemical vapor deposition, high-pressure, high-temperature synthesis as well as wet-milling methods are used to produce a sizeable set of samples. To investigate the samples, i.e. to study the optical properties of embedded SiV centers we rely on optical excitation. In particular, confocal microscopy is used to collect emitted fluorescent single-photons. An attached spectrometer or a Hanbury Brown and Twiss setup offer further insights into the properties of the SiV center as a single photon source. We examine a large number of individual SiV centers produced with different methods, allowing us to establish distributions of selected SiV center properties. To our knowledge, this is the largest coherent examination of this type to date. After charting the luminescence properties of emitters, we examine the possibilities of coupling SiV centers to antennas and study the effect. Furthermore, we explore the use of SiV centers in combination with a VCLS.

The thesis is structured as follows: chapter 2 introduces the reader to color centers and diamond as a host material. A detailed discussion of SiV centers and their most important luminous properties is presented. Figure 3 familiarizes the reader with the essential experimental setup and methods deployed in this thesis to study SiV centers. Various relevant methods of synthesizing SiV centers in nanodiamonds are presented and discussed in Figure 4. Table 5 is dedicated to the important topic of gauging the quality of the fabricated samples. The results of investigating the luminous properties of our SiV center samples is presented in section 6. The possibility of coupling single SiV centers to photonic structures is investigated in Figure 7. Finally we summarize and discuss our findings of this thesis in chapter 7.3.2.

---

---

## Chapter 2

# Silicon Vacancy Centers in Diamond

In the following we introduce color centers, i.e. optically active point-defects, present in a diamond lattice. We focus on color centers combining silicon impurities and lattice vacancies (SiV) in particular since their experimental study is at the focus of this thesis. We start by presenting the most important properties of diamond and emphasize its suitability as a host for optical applications with color centers. A classification of diamond with respects to defects and impurities as well as crystallinities serves as a preparation for the introduction of methods to synthesize diamonds containing SiV centers presented in ?? . Finally, we discuss SiV centers in detail and focus on their most important optical properties as reliable single-photon sources at room temperature. In particular, we zoom in on the key features of its luminescence spectrum, the zero-phonon-line and the phonon side band. Our discussion partially follows the presentation in [?, ?, ?, ?].

### 2.1 Diamond as a host lattice

Diamond is a metastable modification of carbon which is, in fact, stable under normal pressure and at room temperature [?]. Carbon atoms form strong  $sp^3$ -bonds with each other in a tetrahedral arrangement of neighboring atoms. The resulting  $sp^3$ -hybridized lattice is of exceptional mechanical stability, making diamond the hardest known material [?]. The crystal structure can also be interpreted as a face-centered cubic (fcc) lattice with two carbon atoms in the primitive Bravais cell, situated at  $(0, 0, 0)$   $a$  and  $(\frac{1}{4}, \frac{1}{4}, \frac{1}{4})$   $a$  with  $a = 3.567 \text{ \AA}$  denoting the lattice constant [?]. Figure 2.1 illustrates the structure.

The valence and conduction bands of diamond are separated energetically by a large direct band gap of 7.3 eV while its indirect band gap amounts to 5.5 eV [?, ?]. As a result diamonds are transparent for light of all wavelengths larger than 230 nm [?]. This transparent quality makes diamond an ideal host material for various optically active lattice defects or impurities. These induce a wide range of discrete energy levels accommodated by the sizable band gap. The absorption of optically active impurities or impurity complexes gives rise to the color of diamonds, thus these impurities are commonly termed color centers [?]. Due to the exceptional mechanical stability of diamond color centers too are very stable, another important property enabling optical applications.

A property of diamond, detrimental to some optical applications, is its large refractive index

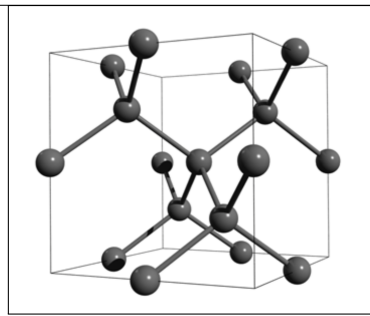


Figure 2.1: Face-centered cubic diamond lattice. Note the tetraedal arrangements of carbon atoms. Figure reproduced with permission from [?].

with values of 2.49 at 360 nm and 2.4 at 800 nm respectively [?]. Thus, a portion of the fluorescent light escaping from the diamond is reflected back into it, effectively reducing the efficiency of light extraction. If nanodiamonds smaller than the wavelength of the light to be collected are used, internal reflection is suppressed and the extraction efficiency can be increased [?].

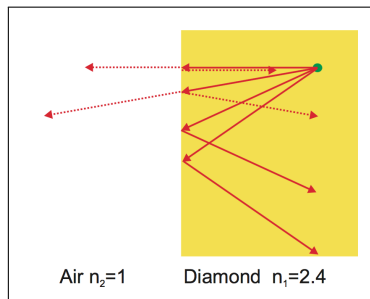


Figure 2.2: Light from a fluorescent emitter inside the diamond (green dot) undergoes reflection at the diamond-air interface. Figure reproduced with permission from [?].

## 2.2 Classification of diamond

Two major approaches for classifying diamond are commonly encountered. First, classification according to the presence or absence of certain impurities or impurity complexes. Second, classification based on different diamond crystallinities observed. In the following both classification systems are briefly introduced.

### 2.2.1 Classification by impurities

Impurities or complexes of impurities in the diamond lattice can be optically active and thus change the optical properties of diamond. Most strikingly perhaps is the appearance of color in otherwise colorless diamond due to a sufficient concentration of such defects. Using IR absorption spectroscopy the degree of nitrogen impurities can be determined. It is used to subdivide diamonds into distinct groups named Type I and Type II [?, ?]. The groups are further subdivided as follows:

- Type Ia: With a nitrogen concentration of up to 3000 ppm most natural occurring diamonds belong to this group [?]. Nitrogen appears arranged predominantly in aggregate clusters forming complexes of impurities. These complexes are optically active, absorbing light in the blue range of the visible spectrum. Consequently Type Ia diamonds often exhibit a yellow to brownish coloration.
- Type Ib: With concentrations of up to 500 ppm nitrogen atoms appear predominantly in isolation, replacing individual carbon atoms in the diamond lattice. In addition to absorbing visible blue light, green is being absorbed as well. Type Ib diamond thus exhibits intensified the yellow or brownish coloration. While only 0.1% of naturally occurring diamond fall into this class, almost all synthetic diamonds created using the high-pressure, high-temperature (HPHT) method are of Type Ib [?].

While Type I diamond exhibits an appreciable concentration of nitrogen, Type II diamonds lack nitrogen entirely. Type II diamond is divided into two subgroups according to the presence or absence of boron as follows:

- Type IIa: Can be considered pure as they lack boron impurities and other optically active defects [?]. They thus are colorless. Up to 2% of naturally occurring diamond and most diamonds synthetically created using the chemical vapor deposition (CVD) method are of Type IIa [?].
- Type IIb: Contains appreciable concentrations of boron atoms replacing individual carbon atoms in the diamond lattice. Boron defects are optically active absorbing visible light ranging from red to yellow. Depending on the Boron concentration blue to grey colorations are observed. Furthermore, diamond is turned from an insulator to a efficient p-type semiconductor in the presence of boron impurities [?].

We remark that for many modern applications of diamonds the presented "classic" categorisation of diamond is not enough. In these cases a precise quantification of the concentration and nature of various relevant impurities is called for [?, ?].

In this section we also briefly touched upon the CVD and HPHT methods, two approaches to synthetically produce diamonds. Both are relevant for this thesis and are explained in detail in ?? .

### 2.2.2 Classification by crystallinity

Up until now, the discussion assumed that diamond forms a lattice consisting of one giant single crystal. However, other crystallinities are possible and can be used to classify diamond. They range from mono or single crystals to polycrystalline, nanocrystalline or even ultra-nanocrystalline diamond films [?]. This classification is particularly useful for synthesized diamond as will be discussed in ?? . Table 2.1 summarizes the different sizes of diamonds or diamond films which can be achieved using variations of the CVD method.

Diamond films consist of isolated diamond grain of random orientation with sp<sup>2</sup> hybridized grain boundaries and graphit-like inclusions [?]. Carbon present in non-diamond phases, e.g. graphite or amorphous carbon gives rise to detrimental light absorption while crystal boundaries lead to increased scattering losses. As the size of diamond crystallites get smaller, the

ratio of non-diamond carbon to diamond carbon increases. Thus losses are most pronounced for the smallest grain diamond films.

Table 2.1: Classification of diamonds synthesized using CVD [?].

Crystallinity	Grain size
monocrystalline	arbitrary
polycrystalline	50 nm to 10 $\mu\text{m}$
nanocrystalline	10 nm to 50 nm
ultra-nanocrystalline	< 10 nm

## 2.3 Silicon-vacancy center

A color center is an optically active point-defect in a crystal lattice, capable of absorbing and emitting light. Defects can consist of one or several vacant lattice sites, foreign atoms replacing lattice atoms or a combination thereof. If the presence of a defect induces discrete energy levels located in the band gap of the host material, the color center can be interpreted as its own quantum system. In other words, the color center can be viewed as a single isolated and localized artificial atom embedded in a host matrix. As such it is able to absorb light and emit single photons by means of fluorescence.

Compared to alternative single photon sources like single atoms [?], Ions [?] or individual quantum dots [?, ?], color centers offer a couple of advantages due to their solid state environment. As a result of the high mechanical stability of the host lattice color centers exhibit increased photo-stability, in particular compared to organic molecules as light sources. Furthermore the host lattices offers protection for color centers from detrimental interactions with aggressive free molecules [?]. Lastly, color centers can be handled and investigated at room temperature, thus significantly reducing the experimental efforts necessary to study them.

Of particular interest are color centers as single photon sources when hosted in diamond. With its transparency, exceptional stability and minimal phononic interactions at room temperature the diamond lattice is an ideal host matrix for color centers [?, ?]. While more than 500 different color centers in diamond are documented, only a small fraction has been investigated with respect to their properties as single photon sources [?]. For an in-depth review of color centers and their versatile applications see [?, ?]. The two arguably most prominent examples of well-studied color centers are vacancy centers featuring nitrogen and silicon [?, ?, ?].

The silicon-vacancy (SiV) center in diamond and its properties is at the center of this thesis. The SiV center has been established as an efficient single photon source at room temperature. It shows very narrow emission lines with record count rates up to  $6.2 \times 10^6$  cps (counts-per-second) [?]. The emission of indistinguishable photons and the optical access of electronic spin states have been demonstrated [?, ?, ?, ?], hinting at the possibility of deploying SiV centers as spin-qubits.

A silicon-vacancy center is formed in a diamond lattice by substituting two carbon atoms by a silicon atom and a nearby empty lattice site respectively. The silicon atom occupies its energetically optimal position by sitting in-between two lattice sites. This is called “split-

vacancy” configuration and induces a  $D_{3d}$  symmetry with the two vacancies and the impurity alligned along the  $\langle 111 \rangle$  diamond axis [?], see Figure 2.3.

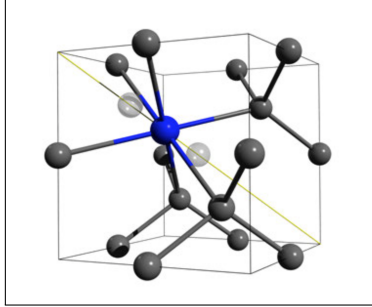


Figure 2.3: Crystal structure of the SiV center embedded into the diamond lattice: The silicon atom (blue sphere) sits in between two vacant lattice sites (white spheres) forming a “split-vacancy” configuration aligned along the  $\langle 111 \rangle$  crystallographic axis (yellow line). Figure reproduced with permission from [?].

The SiV center is known to occur in two different charge states. The first is the neutral state or  $\text{SiV}^0$  with a zero-phonon transition at 1.31 eV (946 nm). It is associated with a  $S = 1$  ground state [?]. The second state is the negatively charged state  $\text{SiV}^-$  where the silicon-vacancy center recruited an additional free electron. It exhibits a zero-phonon transition at 1.68 eV (738 nm). Its ground state has been determined as a  $S = \frac{1}{2}$  state [?, ?]. Due to its outstanding brightness and the location of the zero-phonon-line in the visible range of the spectrum, this thesis focuses on the negatively charged SiV center. For convenience we drop the charge distinction from now on and refer to  $\text{SiV}^-$  centers simply as SiV centers.

SiV centers have been created using CVD in nanodiamonds and single-crystal diamond films [?], see ?? for details. It is also possible to directly implant silicon atoms into pure diamond. High temperature annealing must then be used to animate present lattice vacancies to recombine with silicon impurities in order to form split-vacancy SiV centers [?, ?].

In the following sections we detail the most important luminescence properties of SiV centers in diamond. For a comprehensive review we refer to [?, ?] and references therein.

### 2.3.1 Luminescence properties

The silicon-vacancy center as a quasi-atomic system is capable of absorbing and emitting light. When a ground state electron absorbs a photon of appropriate energy, it is promoted to a discrete higher-energy excited state located within the band gap of the diamond host matrix. Reversing this excitation relaxes the electron back down to the ground state while emitting a so-called fluorescent photon, accounting for the energy difference between excited and ground state. This transition is “spin-allowed”, limiting the life-times of excited states to nano-seconds and thus promoting rapid relaxation and associated fluorescence [?].

Since fluorescence is directly linked to the electronic structure of the SiV center, see Figure 2.4. It follows that photoluminescence spectroscopy can be used to study it using a laser to optically excite the SiV center. In the context of this thesis, optical above-resonant excitation is the method of choice, in particular, when used in conjunction with a confocal photoluminescence setup which will be discussed in ?? . If the excitation energy exceeds the energy of the

lowest excited state, electrons are promoted to higher electronic and vibrational states. Conveniently, these states relax rapidly towards the lowest excited state in non-radiative processes [?]. Once the lowest excited state is reached, a fluorescent transition can follow. It has been shown that above-resonant excitation is feasible for excitation energies ranging from 1.75 eV to 2.55 eV [?, ?, ?]. If the excitation energy is chosen too high, however, the SiV center is ionized. Electrons donated to the diamond conduction band do not participate in fluorescence. Ionization may be reversed if a positively charged SiV center manages to capture a free electron from the conduction band. This charge state conversion is believed to be linked to fluorescence intermittence, more intuitively named as blinking SiV centers [?, ?].

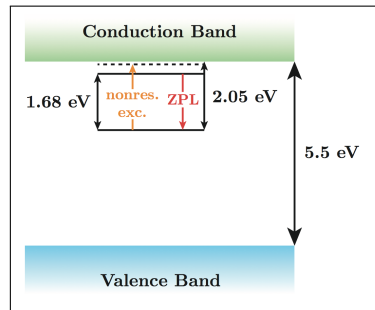


Figure 2.4: Simplified picture of the generous 5.5 eV band gap of diamond with discrete states induced by the presence of SiV centers. The SiV center ground state is situated 2.05 eV below the diamond conduction band. The lowest excited state sits 1.68 eV above the ground state with the zero-phonon-line transition in red connecting the two. Above-resonant optical excitation is indicated in orange. Figure courtesy of [?].

The fluorescence spectrum of SiV centers have two prominent features: A narrow zero-phonon-line and a broad phonon side band. The former is connected to fluorescent photons associated with a purely electronic transition while the latter involves vibrational transitions involving electron-phonon interactions. The phonon side band is typically shifted to higher wavelengths with respect to the zero-phonon-line. The resulting energy deficit can be explained by phonons being created during the relaxation of higher vibrational states. A shift in the opposite direction can also be observed in rare cases if phonons are absorbed during the relaxation process [?].

The relative strength of the zero-phonon-line and the phonon side band is connected to the electron-phonon coupling of the excited color center and thus to lattice vibrations. When a color center is excited, its charge distribution changes. As a result, the equilibrium positions of all particles involved in the color center shift leading to changes in color center geometry. Naturally, the combined changes of charge distribution and geometry of the color center affect the surrounding atoms of the host lattice. Similarly, if the excited state relaxes back to the ground state, the process occurs in reverse. Thus, due to differing atomic arrangements for ground and excited states, the emission and absorption of photons is accompanied by lattice vibrations, i.e. phonons. In other words, the electron-phonon interaction couples the motion of the lattice and electronic transitions of a color center [?, ?].

The Huang-Rhys model allows us to discuss the electron-phonon interaction in SiV centers in more detail. Our discussion follows the presentation in [?]. The model assumes in its simplest form that vibrational modes can be modelled as oscillations of nuclei between their equilibrium coordinates  $q$  associated with the electronic states [?]. Let  $\mathcal{K}_{3A_2}(q)$  and  $\mathcal{K}_{3E}(q)$

denote the harmonic potentials of the ground and excited states respectively:

$$\mathcal{K}_{^3A_2}(q) = \frac{1}{2}\Omega^2 q^2 \quad (2.1)$$

$$\mathcal{K}_{^3E}(q) = C_{^3E} + aq + \frac{1}{2}(\Omega^2 + b)q^2 \quad (2.2)$$

$$= C_{^3E} - C_R + \frac{1}{2}(\Omega^2 + b)(q - \delta q)^2. \quad (2.3)$$

It follows that the vibrational modes of ground and excited states are given as harmonic states with discrete energies  $\hbar\Omega(\nu + 2)$  as well as  $\hbar\sqrt{\Omega + b}(\nu + 2)$  respectively, where  $\nu$  denotes the occupation number and  $\Omega$  the frequency. Further, let  $aq$  denote the linear nuclear displacement of the excited state configuration with respect to the ground state equilibrium where  $q = 0$  holds. The quadratic term  $bq^2$  refers to the vibrational frequency shift due to a redistribution of charge between the electronic states. Given the linear and quadratic electron-phonon coupling strengths  $a$  and  $b$ , the equilibrium displacement of the  ${}^3E$  state can be obtained as:

$$\delta q = \frac{-a}{\Omega^2 + b}, \quad (2.4)$$

while the relaxation energy reads [?]:

$$C_R = \frac{a^2}{2(\Omega^2 + b)} = \hbar S \sqrt{\Omega + b}, \quad (2.5)$$

where  $S$  is referred to as Huang-Rhys factor.

To reason about the probabilities of various transitions between different vibrational levels associated with ground and excited states, the Franck-Condon principle can be applied [?, ?]. It states that transitions between electronic states become more probable if origin and destination states have vibrational levels with similar energy. This implies that the most probable transitions occur between states requiring no change of nuclei positions. Figure 2.5 illustrates the application of the principle for the Huang-Rhys model.

We find that the most probable optical relaxation from an  ${}^3E$  excited state back to an  ${}^3A_2$  ground state originates from the fundamental vibrational  ${}^3E$  state, i.e. the lowest-energy excited state. This state is shifted by  $\delta q$  with respect to the ground state, indicating that the energetically optimal nuclei positions differ from their ground state equilibrium positions. The most probable destination of the relaxation is a higher vibrational level of the  ${}^3A_2$  ground state with similar nuclei positions. From there, electron-phonon interactions continue the relaxation process down to the fundamental vibrational level of the ground state. This non-radiative process allows nuclei to return to their original ground state equilibrium positions. The process of exciting the system from the ground state, proceeds in reverse. The most probable optical excitation promotes an electron from the fundamental  ${}^3A_2$  ground state to a higher vibrational level of the  ${}^3E$  excited state. The optical transition is such that nuclei positions do not change. Note that optical transitions are faster than vibrational transitions since they do not require a change in nuclei positions. Once in the higher vibrational excited state, electron-phonon interactions mediate a transition down to the fundamental  ${}^3E$  excited

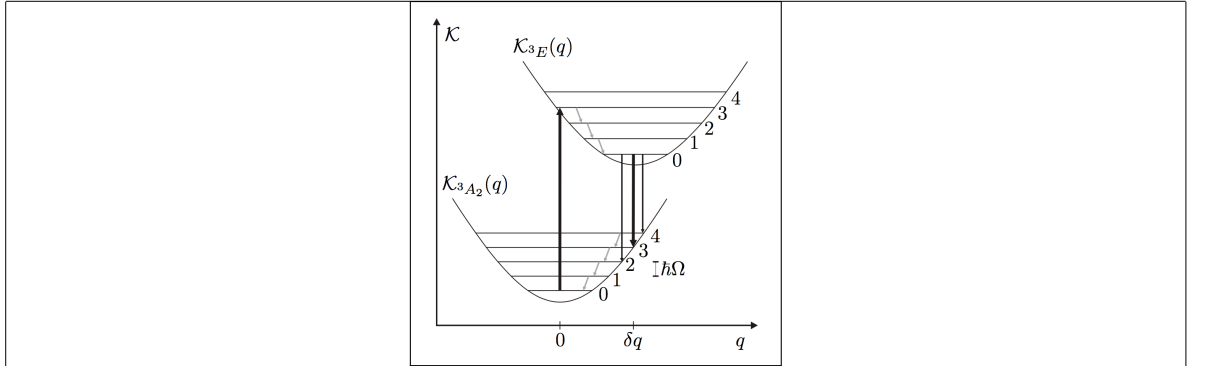


Figure 2.5: Huang-Rhys model of the vibrational transitions in the Frank-Condon picture: The excited state  $\mathcal{K}_{3E}(q)$  is shifted by  $\delta q$  with respect to the ground state potential  $\mathcal{K}_{3A_2}(q)$ . The recombination originating at  $\delta q$  marks the most probable transition (thick black arrow) from the fundamental  $^3E$  vibrational level to one of the vibrational levels of the  $^3A_2$  ground state followed by non-radiative transitions to the equilibrium position  $q = 0$ . The number of vibrational quanta involved in an optical transition are determined by the Huang-Rhys factor  $S$ . The excitation reverses the process. Optical transitions occur between states with identical values of  $q$  and are shown as vertical black arrows. Non-radiative transitions change the value of  $q$  and are shown as angled gray arrows. Figure and caption reproduced with permission [?].

state with an associated change in nuclei positions. From there the relaxation-excitation cycle and its induced periodic changes in nuclei positions repeats.

As discussed, transitions involving phonons mostly originate from the fundamental vibrational level of excited electronic states and end in higher vibrational states of the electronic ground state. Photons emitted during the relaxation process are associated with the phonon side band of the SiV center. The observed red-shift of the phonon side band is directly tied to the phonon energy with higher order sidebands showing multiples of this energy. Note that the The Huang-Rhys factor  $S$  can be interpreted as an indicator of the most probable optical transition involving photons. Thus, it can be used to quantify the strength of the electron-phonon interactions in SiV centers. A small value of  $S$  indicates a weak electron-phonon coupling resulting in negligible phonon side band emissions. If no phonons are involved, the entire emission is concentrated in the zero-phonon-line. Conversely, a large value of  $S$  indicates extensive electron-phonon interactions, leading to a pronounced phonon side band and a weaker zero-phonon-line. This dependence is naturally described by

$$\frac{I_{ZPL}}{I_{ZPL} + I_{PSB}} \quad (2.6)$$

For SiV centers hosted in polycrystalline diamonds the Huang-Rhys factors have been determined to be very small ranging from 0.08 to 0.24 [?, ?, ?]. As a result the zero-phonon-line as the most probable transition dominates the luminescence spectrum making SiV centers excellent narrow-band emitters. Figure 2.6 illustrates the stark difference between the zero-phonon-line and the phonon side band. In contrast,  $S = 3.74$  has been established for nitrogen vacancy centers [?]. A electron-phonon coupling of this magnitude concentrates almost all emission into the phonon side band and leaves the zero-phonon-line almost indetectable.

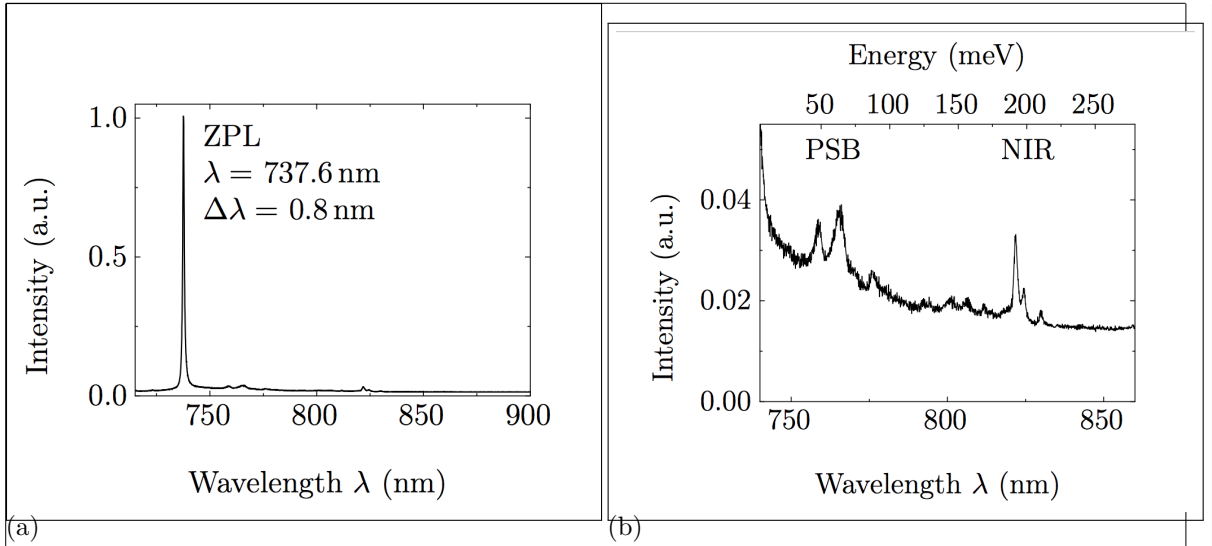


Figure 2.6: (a) The narrow zero-phonon-line dominates the luminescence spectrum. (b) Low intensity phonon side band shows distinct vibrational transitions. Figure reproduced with permission [?].

As an alternative measure for the electron-phonon coupling the Debye-Waller factor can be used. It is closely related to the Huang-Rhys factor and defined as

$$D_w = e^{-S}, \quad (2.7)$$

which can be interpreted as the fraction of total photons that are emitted into the zero-phonon-line.

We remark at this point, that our discussion based on the Huang-Rhys model is assumes that only one vibrational mode couples to the color center which is a strong assumption. In general it is believed that in a solid state host matrix a discrimination between the modes of the undisturbed lattice and quasi-local impurity-induced modes is appropriate [?, ?, ?]. Furthermore, various mechanical properties such as stress in the lattice are reported to affect phonon energies [?]. In addition electron-phonon interactions and thus phonon side band features are believed to depend strongly on various local properties of color centers [?, ?]. Thus it is possible to encounter varying phonon side band features from one SiV center to the next. For a more detailed discussion of these effects we refer the reader to [?, ?] and references therein.

We close this chapter with a short discussion of the luminescence spectra of SiV centers at cryogenic temperatures. Naturally as temperatures approach absolute-zero the phonon side band must disappear. If SiV centers are cooled below  $\approx 110 \text{ K}$  a fine structure is revealed [?]. It includes up to 12 different lines with intensities proportional to the natural abundance of the three stable isotopes of silicon  $^{28}\text{Si}$ ,  $^{29}\text{Si}$ ,  $^{30}\text{Si}$  [?]. Each isotope is associated with 4 lines attributed to doublet levels of ground and excited states which are split by 0.2 meV and 1.07 meV respectively [?, ?, ?]. The splitting itself is believed to be a result of spin-orbit coupling with a weak contribution of the dynamic Jahn-Teller effect [?]. Initial results were based on ensembles of SiV centers, however, recently the splitting was detected for isolated

SiV centers as well [?]. Figure 2.7 shows exemplary spectra representative for ensembles and single SiV center at cryogenic temperatures.

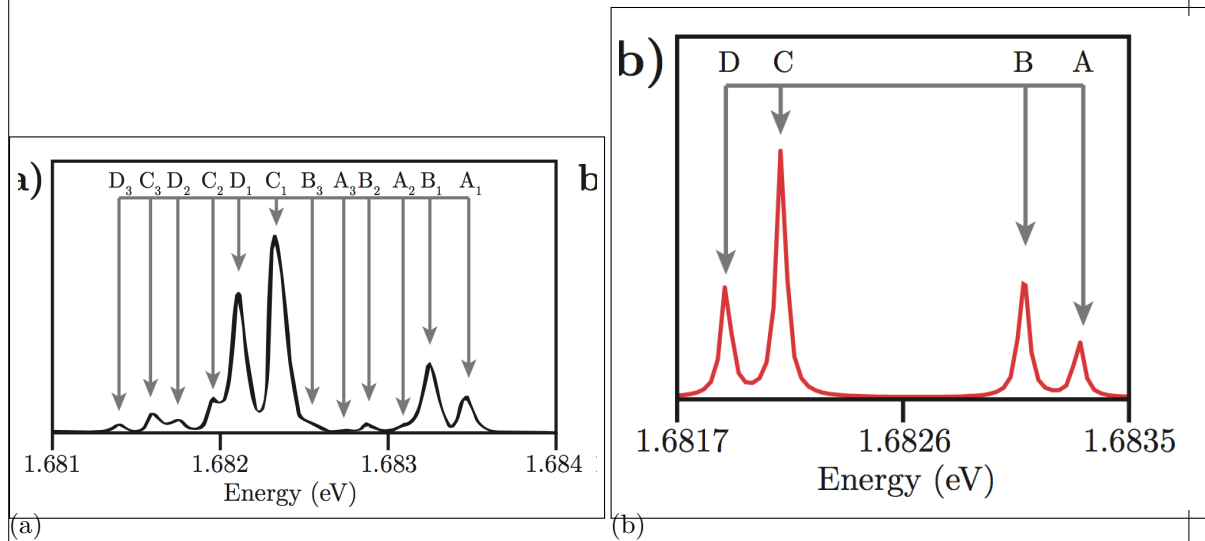


Figure 2.7: (a) Fluorescence spectrum of an ensemble of SiV centers at 10 K. 12 peaks can be seen, 4 for each stable isotope of silicon [?]. (b) Fluorescence spectrum of an isolated SiV center at 15 K. 4 peaks can be seen, 2 for the ground state and 2 for the excited state. Figure reproduced from [?].

---

---

## Chapter 3

# Photoluminescence Setup

### Remark:

Fix: For this axis the resolution amounts to , in the plane of the sample it is.

Fill in missing values described as todos.

The study of SiV centers in nanodiamonds requires dedicated experimental methods and techniques. In the following we detail the experimental setup used to obtain the results presented in later chapters. The core of the setup consists of a confocal microscope connected to either a grating spectrometer or a Hanbury Brown and Twiss interferometer. The former yields fluorescent spectra of SiV centers while the latter enables measurements of the intensity autocorrelation function of individual emitted fluorescent photons.

### 3.1 Confocal Setup

When studying SiV centers experimentally, two capabilities are key: Exciting SiV centers into emitting fluorescent light using a laser and the ability to register resulting SiV center fluorescence. A confocal setup elegantly supports both requirements. Confocal microscopy uses an objective to focus a laser onto a small volume of a sample which can be used to excite SiV centers in a controlled fashion. As the luminescence light returning from the emitter is in the same focus as the excitation laser light, it is effectively collected by the objective, thus the designation "confocal". For an overview of confocal microscopy we refer the reader to [?].

Figure 3.1 illustrates the confocal setup deployed in this work. With the exception of the laser and the sample stage, the whole setup is fixed to a vertical breadboard. The vertical design permits a horizontal sample stage, promoting quick scanning and exchanging of samples. The sample itself resides ontop of a translation stage and is held in place sufficiently by surface friction. It is oriented by an aluminum angle adjustable via a manual rotation stage. The translation stage is moved by two stepper motors (Newport MVP25XL) enabling the sample to be translated horizontally, i.e. in the  $x - y$  plane. Above the horizontal stage, the objective is fixed to another stage which in turn is mounted to a vertical breadboard. In this way, the vertical distance between the sample and the objective can be controlled. As a result the focus of the laser can be adjusted along the  $z$  axis, i.e. the optical axis, allowing to implement a full three-axis scan of samples.

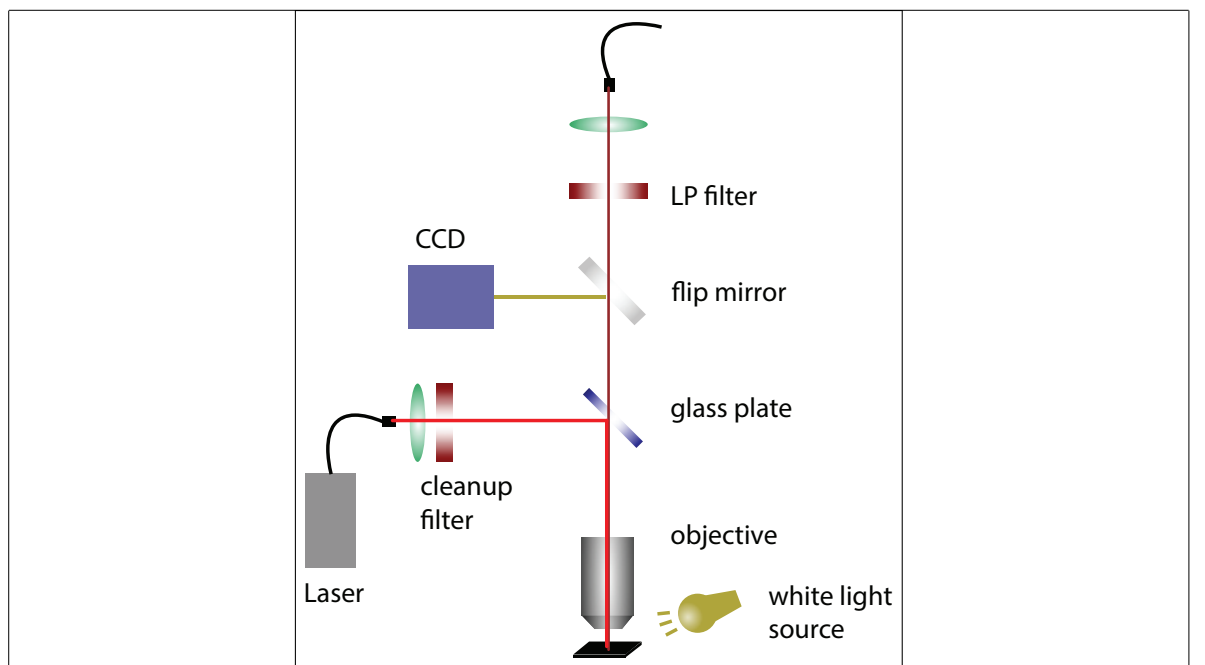


Figure 3.1: Confocal microscopy setup. An excitation laser beam (red) leaves an optical fiber and is directed towards a glass plate. The glass plate reflects  $\approx 10\%$  of the incoming beam towards an objective after which is focused onto the sample. The same objective collects the resulting fluorescent light and redirects it towards the glass plate where  $\approx 90\%$  of the light is allowed to pass. The passing fluorescence light is fed into an optical fiber which connects to the detection part of the setup. A flip mirror can be engaged to bring a CCD camera into the setup in case a white light source is used to illuminate the sample.

The bright red color in the sketch in Figure 3.1 represents the path of the excitation laser beam. The sample is excited with a continuous wave diode laser (Schäfter-Kirchhoff, 58FCM) emitting at a wavelength of 660 nm. The outlet of the laser is a pigtail fiber. The laser light is outcoupled and collimated by an aspheric lens. To suppress sideband emission from the laser, a 660 nm bandpass filter with a filter window of 10 nm is used. After this cleanup filter, the excitation beam hits a mm glass plate (fabricator Halle Germany) redirecting the beam. It is then focused onto the sample by a 100 $\times$  microscope objective (Olympus, LMPlanFLN) with a numerical aperture of 0.8.

The collected light follows the detection beam path depicted in dark red in Figure 3.1. Both the excitation light reflected from the sample surface and the fluorescence light from the color centers pass through the glass plate. Removing the flip mirror behind the beamsplitter from the path directs light towards a single mode fiber (Thorlabs SM600) connecting the confocal setup with either the spectrometer or the HBT setup. Prior to focusing light into the single mode fiber using an aspheric lens, a longpass filter is deployed to eliminate residual excitation light and ambient light. The filter is chosen with a cutoff wavelength of 710 nm or 720 nm. Besides the obvious purpose of guiding the photoluminescence light to the spectrometer and the Hanbury Brown and Twiss setup for spectroscopic investigations, it serves another crucial purpose: Its diameter of about 4.3  $\mu\text{m}$  serves as a pinhole to reject photoluminescence light from depths outside of the focal plane [?]. For this axis the resolution amounts to , in the plane of the sample it is .

thickness

value

value

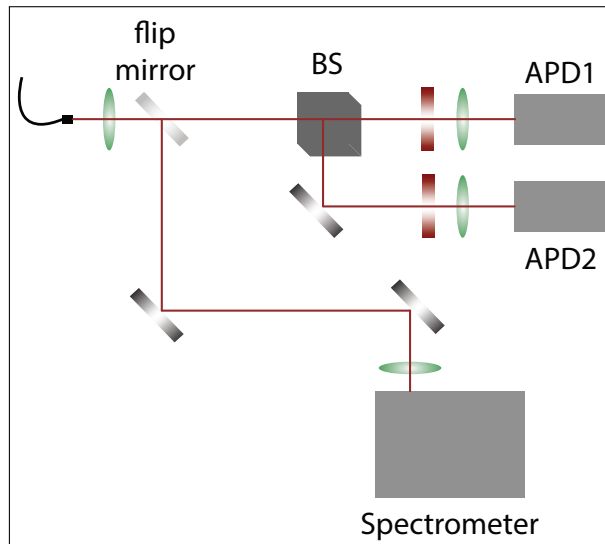
short discussion  
if resolution is enough

We remark that the glass plate in used Figure 3.1 has a high transmission of  $\approx 90\%$ . This leads to a high collection efficiency of fluorescence light at the cost of excitation efficiency since most of the exciting light is not being redirected towards the sample. In contrast to that, certain use cases such as saturation measurements require high excitation intensities. To realize these the glass plate may be replaced by dichroic mirror (DRLP692). A dichroic mirror spectrally separates excitation light from photoluminescence light as it selectively transmits and reflects sight as a function of its wavelength.

In general, if a high excitation is required we opt for a dichroic mirror, otherwise working with the glass plate at lower excitation is the default. This is advised since high intensities carry the danger of damaging SiV centers and can also cause permanent fluorescent intermittence of SiV centers, i.e. blinking, as an unwanted side-effect see ??.

## 3.2 Optical Imaging of The Sample Surface

The setup introduced in the previous section can be modified to investigate the sample surface before starting fluorescence measurements. For this purpose, the sample is directly illuminated at a flat angle from outside the objective with white light from a halogen lamp, see the white light source in Figure 3.1. The flip mirror behind the glass plate is brought into an upright position to guide the light towards a CCD camera. The scattered light from the sample surface is collected by the objective and the surface is imaged on the CCD chip. Thus nanodiamonds and other features on the substrate are made visible. The resolution of this configuration of the setup is limited by .



optical  
diffrac-  
tion,  
shadows

Figure 3.2: Spectrometer and HBT interferometer. Fluorescent light arrives via an optical fiber and is directed towards a flip mirror. The mirror directs the beam either towards a 50:50 beam splitter (BS) into the APDs of the HBT setup, or into a grating spectrometer.

In chapter Figure 7 we introduce applications of SiV centers in nanodiamonds, for which knowing the precise positions of specific nanodiamonds is crucial. Therefore, cross markers are milled into the surface of the substrate on which the nanodiamonds are situated. These

markers of a size of  $10\text{ }\mu\text{m}$  can easily be recognized by optical imaging. The starting point for a scan of an area of interest on the sample is fixed while navigating with the optical image. After flipping the flip mirror, light is directed towards the detection part of the setup enabling systematic scans of the sample.

### 3.3 Spectrometer

Figure 3.2 displays the detection part of the setup. The fluorescence light arrives via a pigtail fiber connecting the confocal setup with the detection setup and is outcoupled with an aspheric lens. A flip mirror is employed to direct the light either to a grating spectrometer or the HBT setup. The optical spectrum of a light source gives insight to the optically active constituents and therefore bears information about the emitter.

As mentioned before, the fluorescence light from the SiV centers is investigated with the grating spectrometer (Princeton Instruments Acton2500i). The incident beam passes through an entrance slit, is then scattered on the grating where the light is spectrally divided and finally hits a detector, imaging the entrance slit on the detector surface. The employed detector is a CCD camera (Princeton Instruments, Spec-10) cooled with liquid nitrogen to a temperature of  $-120\text{ }^{\circ}\text{C}$ . This limits background signals due to thermally generated free charge carriers. The spectrometer is optimized for detection of light up to a wavelength of  $900\text{ nm}$ . and features three gratings: 600 grooves/mm, 1200 grooves/mm, and 1800 grooves/mm. These gratings are mounted on a turret, allowing easy swapping of gratings between measurements.

With the spectrometer's step-and-glue function which is implemented in the spectrometer software (WinSpec) it is possible, to record several spectra over a wide wavelength range which are then stitched together. It is therefore possible to combine a larger wavelength range with a higher resolution. For most measurements the grating with 600 grooves/mm was used. The resolution of the spectrometer using the  $600\text{ grooves mm}^{-1}$  is  $0.13\text{ nm}$  at  $738\text{ nm}$  and the accuracy amounts to  $\pm 0.4$  as stated by the manufacturer. This resolution suffices for the measurements presented in this work.

### 3.4 Hanbury Brown and Twiss Setup

A Hanbury Brown and Twiss setup is used to establish the intensity autocorrelation function ( $g^{(2)}$  function) of an emitter [?, ?]. In this work, the  $g^{(2)}$  function is used to assert the non-classical behaviour of a photoluminescence source, i.e. characterize its behaviour as a single photon emitter. In the photon number representation, it is defined as follows:

$$g^{(2)}(\tau) = \frac{\langle N(t)N(t + \tau) \rangle}{\langle N(t) \rangle^2}.$$

Here,  $N(t)$  denotes the number of photons at a certain time  $t$ ,  $N(t + \tau)$  denotes the number of photon at a time interval  $\tau$  later than  $t$ . The angular brackets  $\langle \rangle$  denote temporal averaging. For a two-level system  $g^{(2)}(\tau)$  can be interpreted as the probability of detecting two photons separated by a time interval  $\tau$ . The physical intuition behind this definition is as follows: The detection of a fluorescent photon emitted from a quantum system is the result of an excited electron relaxing back to its ground state. To emit a consecutive single photon, an additional electron must first be promoted to an excited state, a process which takes a certain

amount of time, see ???. If  $g^{(2)}(\tau) \neq 0$  in the limit of  $\tau \rightarrow 0$  a system is capable of emitting several photons simultaneously. This is known as photon bunching and is typical for classical light sources. In contrast,  $g^{(2)}(\tau) \rightarrow 0$  for  $\tau \rightarrow 0$  is an indication that no two photons can be detected simultaneously. This property is termed photon antibunching and is a defining characteristic of non-classical light sources such as single photon source. For an in-dept review of the intensity auto-correlation function we refer the reader to [?, ?].

The aim of the HBT setup is to record the time delay between two consecutive photons as a prrequisites to compute  $g^{(2)}(0)$ . A sketch of the HBT setup is shown in Figure 3.2. The photons are detected with single photon avalanche photo diodes (APDs, PicoQuant  $\tau$ -SPAD100). APDs are the semiconductor analog to photomultiplier tubes, i.e. an incoming photon creates secondary charge carriers through ionization. The secondary charge carrier is accelerated by a bias voltage to create more secondary charge carriers, resulting in an avalanche effect. Therefore, the signal of a single photon is intensified and detected as an electrical current pulse. These avalanche photo diodes have a nominal detection efficiency of up to 70% at an optimal wavelength of about 670 nm and a dark count rate of under 100 cps. If a charge carrier created by the avalanche is temporarily trapped and later liberated, it induces a so-called afterpulse. To avoid detecting these artifacts as real events, the APDs have a dead time of about 70 ns. In the ideal case, one APD would be enough to measure the time delay between two consecutive photons. However, the second of two consecutive photons could hit the detector during its dead time. To circumvent this problem, two APDs are employed and the detection beam is split with a non-polarizing 50:50 beamsplitter cube. Each beam then goes through a bandpass filter and is focused on the avalanche photo diode with an aspheric lens. As the beam path is slightly different for each APD, a small optical path difference is introduced, however, this difference only results in an offset of the  $g^{(2)}$  function and does not alter the physical nature of the result. The bandpass filters serve two purposes: First, they limit optical crosstalk between the avalanche photo diodes. The detection process in an avalanche photo diode produces light due to recombination of charge carriers. Crosstalk between two avalanche photo diodes occurs, if one of the photons produced by recombination in one avalanche photo diode escapes and is detected in the other one [?]. Secondly, the bandpass filters serve to reduce background during the  $g^{(2)}$  measurement process or to spectrally divide emission from several emitters. Therefore, it is possible to find single emitters, which are not spatially separated enough to be separated by the spatial resolution of the setup. In particular, emitters can be individually investigated if their ZPLs exhibit wavelengths which are spectrally well separated. Bandpass filters suited for the respective wavelengths are used to selectively investigate light associated with distinct ZPLs.

When the APD fires, it outputs a digital TTL (transistor-transistor logic compatible) signal. The arrival times of the signals (so-called time tags) are recorded with a time tag unit (produced by dotfast-consulting) with a temporal resolution of 78.125 ps. The timing uncertainty of the photon detection process introduces variations of the digital signal's time tag from the actual detection time. This is called timing jitter and adversely affects the recorded time tags and consequently the value of  $g^{(2)}(0)$ . In the past it has been shown to significantly obfuscate the detection of anti-bunching behaviour in single photon source and thus relevant corrections need to be taken into account [?, ?], see ??.

As stated earlier, the time delay between two consecutive photons is necessary for the reconstruction of the  $g^{(2)}$  function. The time delays are fed into a histogram which is then fitted to receive the continuous  $g^{(2)}$  function. As a suitable fit function a numerical convolution between the  $g^{(2)}(\tau)$  derived for a three-level system and detector timing jitter can be used [?, ?, ?].

In the Hanbury Brown and Twiss-setup the arrival time of photons are recorded with two APDs, each of which keeping a list of arrival times as raw data. To get a single array of arrival times of the photons, which can then be binned to obtain the  $g^{(2)}$  function, the arrays of time tags of the two APDs have to be correlated. For that, the time difference between each entry in one array and all consecutive time tags in the other array are determined and binned according to the timing resolution of the time tag unit. After normalizing and fitting these data,  $g^{(2)}(0)$  can be obtained determining whether a emitter characterizes as a single photon source.

---

---

## Chapter 4

# Fabrication of Nanodiamonds

### Remark:

die section mit den silicon implanted nanodiamonds muss von dir ueberarbeitet werden. Die hab ich deshalb vorerst ausgelassen. Es gibt 3 teile (einfuehrung, preliminary tests und final procedure). Ich hab den eindruck, dass sich da konzeptionell vieles wiederholt und das man das ganze vielleicht in einer section unterbringen kann und die feineren unterscheidungen einfach beilaeufig erwaehnt.

section iridium substrate sollte auch nochmal durchgelesen werden. Ich habs zwar nochmal ueberarbeitet, aber ich denke da koenntest du noch den einen oder anderen erklaerendne statz springen lassen. Insbesondere das listin in preparation of substrate ist nicht gerade selbsterklaerend.

Die tabelle mit dem ueberblick ueber alle samples hab ich in eine eigene section geschoben. Die is ja wichtig, weil in den results immer wieder die sample id genannt werden. Wennnd as im inhaltsverzeichnis auscheint, find ich das praktisch.

“Diamond forms under high temperature and pressure conditions that exist only about 100 miles beneath the earth’s surface.”

Gemological Institute of America Inc.

Due to its extraordinary properties, diamond has transcended its sole purpose as a rare gem and developed into an important tool enabling various applications in industry and research. This change has been driven largely by the development of methods allowing to cheaply produce synthetic diamond. While synthetic diamonds are typically small and without the splendeur generally associated with diamond, they can be produced on-demand and are thus arguably more useful than rare gemstones. In this chapter we introduce the two most common methods for the fabrication of diamonds in a laboratory setting: The high-pressure, high-temperature and the chemical vapor deposition method. The aptly named high-pressure, high-temperature (HPHT) process mimics the conditions under which diamond is formed in nature and is widely used to synthetically produce diamonds for industrial applications such as utilization of diamond as a abrasive. While HPHT diamonds are utilized in this work, most reported measurements are based on diamond produced with the CVD method in which diamonds are grown using a hydrocarbon gas mixture. Both processes have incommon that defects and impurities are a naturally occurring. For a more extensive list of diamond

production processes refer to [?]. In the context of this thesis nano-sized diamonds are required. They can be obtained by milling larger sized HPHT or CVD diamonds down to the desired grain size in a vibrational mill. The obtained nanodiamonds are small enough that individual specimen have a chance of hosting a singleton SiV center. These can be identified and used for further exploration.

## 4.1 High-Pressure High-Temperature Diamond

The HPHT method was the first process to successfully synthesize diamond in 1879. Today, it is still widely used due to its relatively cheap production costs for small diamonds [?]. In the HPHT process, diamond is synthesized from graphite under temperatures of up to  $1.5 \times 10^3$  °C pressures between  $5 \times 10^4$  bar and  $10^6$  bar [?]. Under these extreme conditions, carbon transitions from its graphite to its diamond phase because the latter becomes energetically favorable [?, ?, ?, ?]. The machine used for this kind of synthesis is a press. For some forms of this method, a metallic catalyst solvent is added lowering the required pressures and temperatures by causing graphite to dissolve earlier. At the same the catalyst promotes the crystallisation process. Several press designs exist, all of which relying on creating and maintaining high pressures and a high temperatures. While it is possible to grow big ( $> 10$  carat) high-quality diamonds with the HPHT process, its cost quickly increases and thus becomes unfavorable.

In this thesis, HPHT nanodiamonds produced by Davydov et al. [?] are spectroscopically investigated.

## 4.2 Chemical Vapor Deposition Diamond

In contrast to the HPHT method, diamond is crystallized from carbon available in the gas phase in the CVD method. The process still requires respectable temperatures in the range of 700 °C to 1300 °C but makes due with the low pressures of less than 1 bar available in a vacuum growth chamber [?].

The chamber contains a vapour consisting of a mixture of atomic hydrogen and methane. The gas can be forced into the plasma phase using strong microwaves or hot filaments [?, ?, ?]. While the hot filament is easy to implement, it has the disadvantage that atoms which are etched from the filament during the growth process are likely to contaminate the diamond. To minimize the introduction of defects other than SiV centers in the diamond, growing diamonds in a microwave plasma is preferred. In it methane molecules dissociate and release carbon. In the presence of a substrate such as iridium containing suitable seeds, carbon can crystalize forming diamond. Figure 4.1 illustrates the setup. In a plasma containing atomic hydrogen, the formation of diamond is favored over the formation of graphite. This is due to the fact that the atomic hydrogen preferentially etches *sp*<sup>2</sup> bonded carbon, i.e. graphite.

Typically, single crystal diamond substrates are required to grow single crystal diamond. HPHT substrates are suitable to start a crystallization process. This approach is referred to as homoepitaxial growth. An alternative approach is to utilize non-diamond substrates such as iridium or platinum to trigger heteroepitaxial growth [?, ?]. This method is utilized for all the CVD nanodiamonds grown and investigated in this thesis. It relies on small

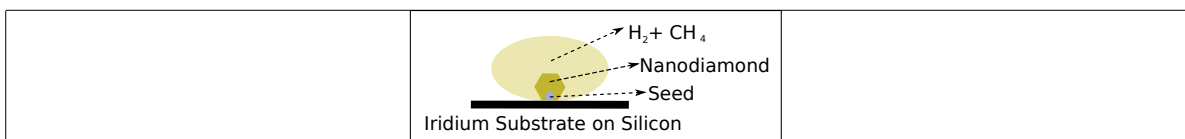


Figure 4.1: Sketch of the CVD method. A hydrogen-carbon plasma acts as a donor for carbon atoms which may crystallize to form diamond ontop of a suitable iridium substrate. An initial diamond seed facilitates the process.

diamond crystals deposited in the substracte acting as seeds for the diamond crystallization process. Seed diamond crystals are commercially available, and are usually particles produced by a so-called detonation process. In a detonation process, the high pressure produced by shockwaves of a detonation is used to create very small diamond particles of a size down to a few nanometers.

Growth on a substrate is favored, if the lattice constant of the substrate and the diamond to be grown are similar. The lattice constant of iridium is 0.384 nm [?, ?] and thus close to the lattice constant of diamond with 0.356 nm [?]. Therefore, we opted to grow diamond on a stratified substrate, consisting of iridium layers of 60 nm to 150 nm thickness. The iridium layers themselves were grown onto an yttria-stabilized zirconia (YSZ) buffer layer, which in turn was grown on a silicon wafer [?]. If the lattice constant of the substrate and the diamond are not matched, stress in the diamond lattice is induced. Therefore, the iridium substrate not only facilitates diamond growth, but also reduces unfavorable stress in the nanodiamonds. The detrimental effects of stress on the diamond lattice and its implications with respect to hosted SiV centers are briefly discussed in section 6.

To produce nanodiamonds of controlled size, the growth process is stopped when the diamonds grown onto the seed crystals are large enough. If the growth process is continued, the individual crystals grow together to form diamond films. Such diamond films are used as starting material for the wet-milling process described in Table 4.3.

One of the advantages of the CVD process is that silicon is incorporated automatically into diamonds, SiV centers can thus be formed *in-situ* as the diamond is grown. The presence of silicon atoms required to be absorbed into the diamond lattice is explained by the plasma etching the edges of the silicon waver underneath the growth substrate. To further increase the silicon content in the chamber, sacrificial silicon can be introduced.

After nanodiamond growth, the nanodiamonds are either investigated directly on the growth substrate or transferred to an ultrasonic bath to obtain a solution which is coated onto other substrates for further exporation.

In this thesis, two types of nanodiamonds samples were investigated. The first batch, henceforth referred to as CVD samples, was grown by the group of M. Schreck, Augsburg Universityusing detonation diamond seeds of a size smaller than 3 nm(produced by the company Microdiamant, product Liquid Diamond monocrystalline, MSY 0-0.03 micron GAF). For the growth process, 1 % of methane was added to the hydrogen environment in the growth chamber. The growth process was performed with a pressure of 30 hPa for 30 min to 60 min, yielding nanodiamonds of a diameter of about 100 nm to 200 nm. A sample of the produced diamonds is given in Figure 4.2.

The second type of samples consist of CVD nanodiamonds grown onto molecular analogs of diamond crystals. A subgroup of these molecular diamonds are called diamondoids and are carbon crystals based on the carbon cage molecule adamantane  $C_{10}H_{16}$ . The molecular

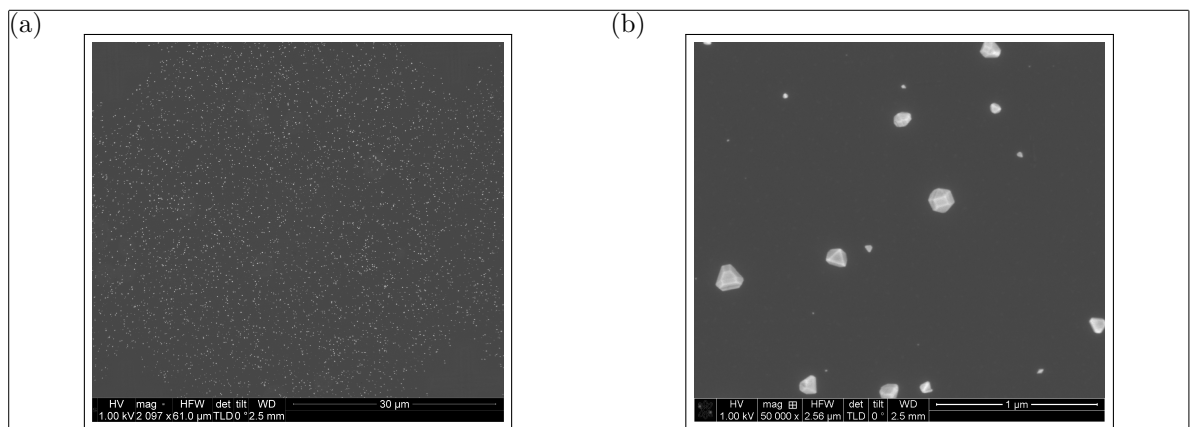


Figure 4.2: SEM images of CVD diamonds (sample insituvcvd) produced by M. Schreck's group at Augsburg University. The average size of these nanodiamonds is 100 nm. (a) Overview image, white dots are nanodiamonds. (b) Detail image, it can be seen that nanodiamond shape and size is varied.

diamonds used for this work are adamantane in cyclohexane, mercapto adamantane in cyclohexane, and cyclohexane. Each of these seed crystals was used in different growth processes. During the growth process, either 1% or 3% methane was added to the hydrogen plasma and either silicon (Si) or silicon dioxide ( $\text{SiO}_2$ ) was injected to promote the formation of *in-situ* incorporated SiV centers, see Table 4.1.

Table 4.1: Summary of the samples grown on diamondoid seed crystals.

Sample name	Seed crystals	Methane conc.	Silicon source
160211_E	Mercapto adamantane in cyclohexane	1%	$\text{SiO}_2$
160211_F	Cyclohexane	1%	$\text{SiO}_2$
160212_C	Cyclohexane	3%	Si
160212_D	Adamantane in cyclohexane	3%	$\text{SiO}_2$
160212_E	Mercapto adamantane in cyclohexane	3%	SiOs
160212_F	Cyclohexane	3%	$\text{SiO}_2$

### 4.3 Wet-Milled Nanodiamonds

In addition to growing nanodiamonds of a specific size directly via a CVD process, macroscopic diamond starting material can be crushed to obtain small diamond particles. In contrast to nanodiamonds directly grown by a CVD process, the process is divided into two sub-processes: At first a macroscopic diamond is produced using one of the methods introduced in this chapter. Then macroscopic diamond is continuously milled into smaller diamond particles.

The wet-milled nanodiamonds investigated in this thesis were kindly provided by A. Muzha, group of A. Krueger, Julius-Maximilians Universität Würzburg. During the wet-milling process small metal beads in an aqueous solution are driven by the vibrations of a vibrational mill. The moving beads continuously collide with the present diamonds and thus keep break-

ing them into smaller and smaller particles. A sketch of the process is shown in ???. Steel contamination introduced by the beads can be eliminated in a post-processing treatment with acid.

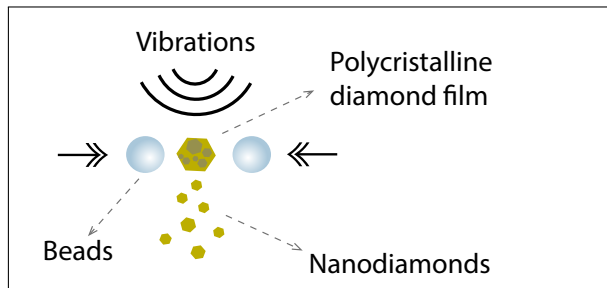


Figure 4.3: Sketch of a vibrational wet-mill. A macroscopic polycrystalline nanodiamond is progressively broken down into smaller polycrystalline nanodiamonds by metal beads.

The big advantage of the milling process is that it enables the production of a large quantity of diamond nanoparticles. When producing nanodiamonds directly via a CVD process, the number of produced nanodiamonds in one process scales with the surface of the substrate on which the nanodiamonds are grown. In contrast, the quantity of milled nanodiamonds scales with the volume of the starting material. Another advantage of the wet-milling process is that the nanodiamonds are already in an aqueous solution after milling. Therefore, it can be used to spin-coat the nanodiamonds directly onto any substrate. Samples created in this fashion can directly be used for further investigation and do not require additional processing.

If the starting material for the wet-milling process is a polycrystalline diamond film, it is likely to break along distinct crystal boundaries. However, due to imperfections in the growth process, particles may break down such that progressively smaller milled diamond grain remain polycrystalline. As a result, the final nanodiamonds contain crystal boundaries themselves, indicative of reduced crystal quality. To improve diamond quality nanodiamonds are treated with post-processing steps including annealing in vacuum and oxidation in air. A detailed description of these processes and their effects is given in Table 5.

In general any diamond, independent of production method, can be used as starting material for the milling process. In the following sections, available samples are distinguished by the respective starting material and milling method.

#### 4.3.1 Wet-Milled HPHT Nanodiamonds

We investigated nanodiamonds wet-milled from a HPHT starting material to median sizes of about 45 nm, 80 nm and 260 nm. They were then drop-cast onto an iridium substrate and implanted with  $^{28}\text{Si}^{1+}$ . The implantation itself was performed by D. Rogalla, Ruhr-Universität Bochum (RUBION - Zentrale Einrichtung für Ionenstrahlen und Radionuklide). All HPHT nanodiamonds were oxidized in air at 450 °C for 3 h. Resulting samples available for explorations are designated hphtimp45, hphtimp80, hphtimp260 and listed in Table 4.2.

Complete  
implanta-  
tion  
param-  
eters

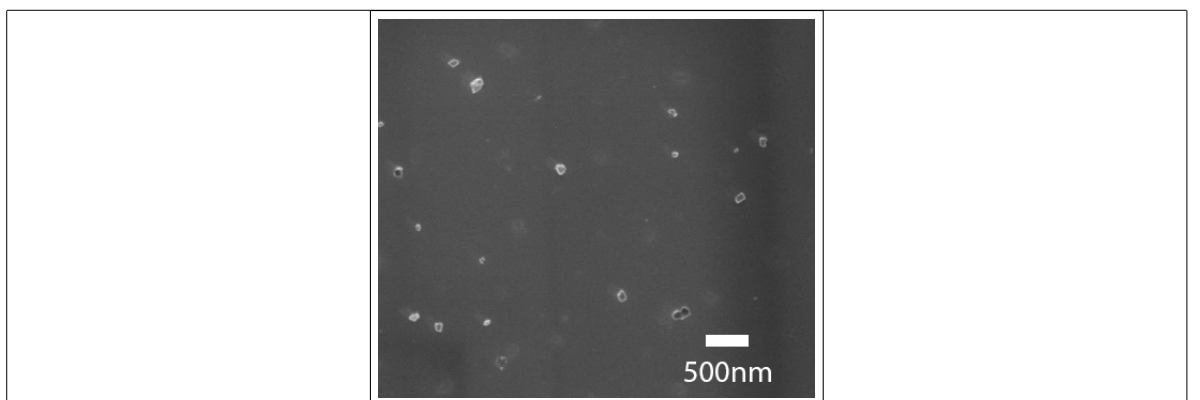


Figure 4.4: Pictures of milled nanodiamonds (sample insitu100) showing the distribution of the nanodiamond crystals on the iridium substrate.

#### 4.3.2 Wet-Milled CVD Nanodiamonds

In the following paragraphs, details of the production processes of nanodiamond produced by wet-milling a CVD diamond film in a vibrational mill are given. For an overview of the samples refer to Table 4.2. The starting material for the wet-milled nanodiamonds was a nanocrystalline diamond film [?] directly grown on a silicon wafer by CVD. A microwave hydrogen plasma containing 1% methane was used to grow on purified 5 nm nanodiamond seeds (produced by PlasmaChem). To induce *in-situ* SiV center creation, sacrificial Silicon pieces are placed in the growth chamber. During diamond growth the silicon pieces are etched by the plasma leading to individual atoms being incorporated into the diamond lattice. The diamond film is then wet-milled in a vibrational mill with steel beads. The high amount of steel containment due to the steel beads is removed by extensive acid treatment. We also investigated nanodiamonds milled with silicon nitride beads, and found that the choice of material of the beads does not result in any noticeable difference in dependent measurements. The median diameters of the diamonds are 50 nm, 70 nm and 100 nm as determined by laser diffraction spectroscopy. ?? shows milled nanodiamonds ontop of an iridium substrate. The aqueous solution containing the nanodiamonds is drop cast onto an iridium film on a Silicon substrate. The iridium film of a thickness of 130 nm is grown onto a buffer layer of yttria-stabilized zirconia (YSZ) which in turn is grown onto a Silicon wafer. The iridium surface has the advantage that it acts as an antenna and therefore enhances the collection efficiency of fluorescence light [?]. For a discussion on the properties of the substrate see section 4.4. Post-process treatment consist of annealing in vacuum at 900 °C or consecutive oxidation in air at a temperature of 450 °C, or a combination of the two. The duration for either treatment method was 3 h to 6 h.

#### 4.3.3 Doubly Wet-Milled Implanted Nanodiamonds Implanted With Silicon

In addition to SiV centers that were implanted during diamond growth, we investigated nanodiamonds with SiV centers implanted after diamond growth. Here a polycrystalline Element Six diamond film (electronic grade) served as the starting material. In bulk material, the implantation causes the SiV centers to form in a specific depth dependent on the implantation

energy, leaving most of the diamond vacant of SiV centers. As a consequence, a big portion of nanodiamonds milled from such a bulk material would not host any SiV centers. To obtain diamond particles with a homogeneous distribution of SiV centers, the process of fabricating implanted nanodiamonds is the following: First, the diamond film is milled to diamond particles a few microns in size. Next, these microdiamonds are spin-coated onto iridium substrates and implanted with  $^{28}\text{Si}^{1+}$ . To eliminate lattice damage and unnecessary vacancies resulting from the implantation process, diamonds were annealed in vacuum and subsequently oxidized. At last, the micrometer sized diamond particles are milled to the desired smaller sizes.

### Preliminary Tests

The starting material was an Element Six electronic grade diamond film. The diamond was milled in a wet-milling process to sizes on the order of micrometers, which were then coated onto a silicon substrate. The microdiamonds were implanted with  $^{28}\text{Si}^{1+}$  at an implantation energy of 1.7 MeV, and fluences of  $10^9 \text{ cm}^{-2}$  to  $10^{12} \text{ cm}^{-2}$ <sup>1</sup>. After implantation, the microdiamonds on the silicon substrate were annealed for 2 h at 900 °C and oxidized in air for another 2 h at 450 °C. However, we encountered the problem that the silicon sublimated and re-nucleated during annealing, causing the diamonds to sink into the silicon surface (Figure 4.5a). Iridium is less prone to damage by high temperatures and withstands annealing procedures up to our standard annealing temperature of 900 °C without problems. Therefore, we used a sample with microdiamonds on a silicon substrate which was not annealed to shake the nanodiamonds off the silicon substrate in an ultrasonic bath, and consecutively coated the microdiamonds on an iridium substrate. After annealing and oxidizing the nanodiamonds on the iridium substrate, the iridium surface was intact.

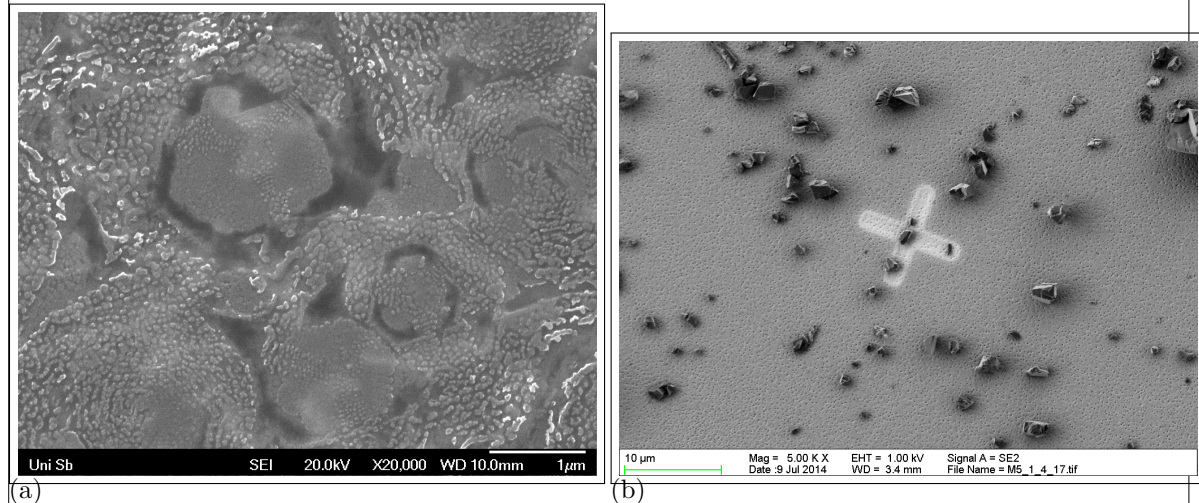


Figure 4.5: (a) SEM picture of nanodiamonds sunken into a silicon substrate after annealing at 900 °C for 3 h. Magnification 20 000. (b) SEM image of the microdiamonds after milling on an iridium substrate, but before implantation. In the middle of the picture, there is a reference cross milled into the iridium substrate with a focused ion beam. Its size amounts to 10 μm. It can be seen, that the microdiamonds exhibit sizes of a few micrometer.

<sup>1</sup>Implantation performed by D. Rogalla, Ruhr-Universität Bochum (RUBION - Zentrale Einrichtung für Ionenstrahlen und Radionuklide).

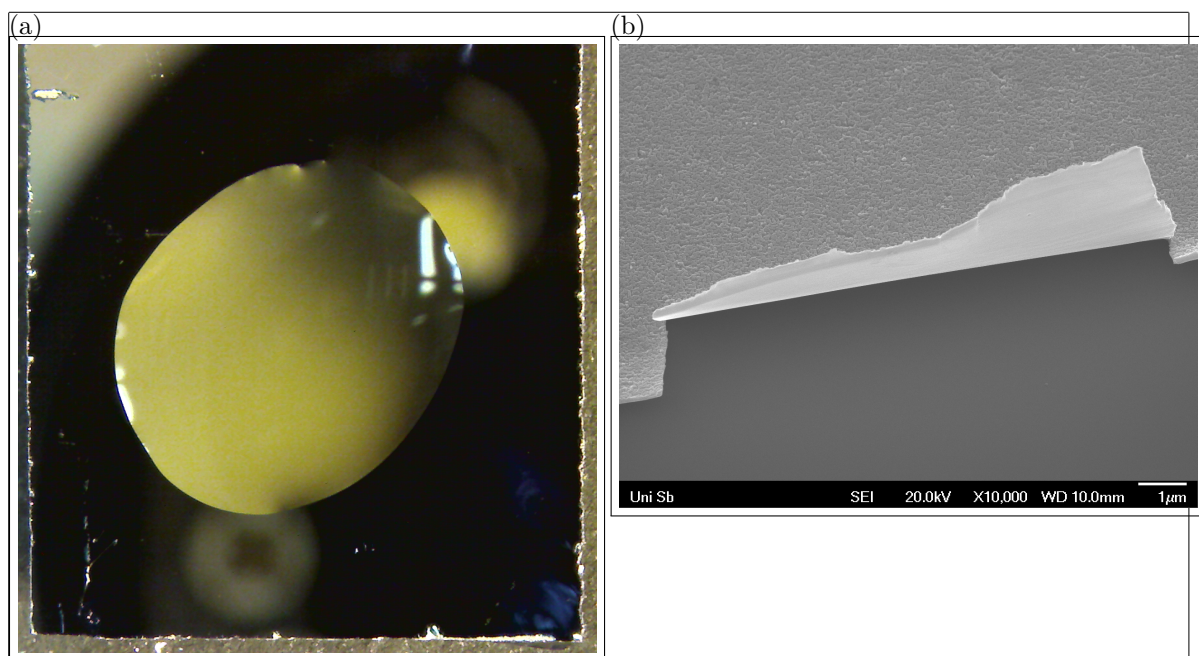


Figure 4.6: (a) Microscope image of a drop of water on an iridium substrate cleaned with Piranha etch. This picture was used to estimate the contact angle. (b) SEM picture of a 60 nm iridium layer that peeled off the substrate after an ultrasonic bath.

### Final Procedure

For the milling process in a vibrational mill, a minimum amount of diamond material is necessary. When starting with a diamond film, this threshold is easily reached, however, a big quantity of microdiamonds is needed to meet the requirements. Therefore, production was carried out at a larger scale after the preliminary tests. The microdiamonds were directly spin-coated onto iridium substrates, implanted with  $^{28}\text{Si}^{1+}$  (implantation energy 900 keV, fluence  $10^{11} \text{ cm}^{-2}$ ) <sup>2</sup> The microdiamonds were then annealed in vacuum for 3 h at 900 °C and oxidized in air for 3 h at 450 °C. At last, they were milled again to sizes of about 40 nm, 45 nm, 240 nm and 260 nm. The diamonds of sizes 40 nm and 240 nm were annealed in vacuum at 1200 °C.

how  
much?

time?

## 4.4 Iridium Substrate

As mentioned in section 4.2, we used a silicon substrate with an iridium layer on top for most experiments in order to match the lattice constants of substrate and diamond. We also use the same substrates for the experiments with wet-milled diamonds, as using iridium has several advantages:

- The high hydrophilicity of iridium enhances the homogeneity of the nanodiamonds on the substrate after spin-coating or drop-casting. The hydrophilicity is further improved by treating the substrate in a Piranha etch (50:50 mixture of sulfuric acid  $\text{H}_2\text{SO}_4$  and

<sup>2</sup>Implantation performed by J. Klug at rubitec - Gesellschaft für Innovation und Technologie der Ruhr-Universität Bochum mbH.

hydrogen peroxide  $H_2O_2$ ) by removing oxide layers on the surface. The treatment with Piranha etch also has the advantage that all organic contamination is removed. Measurements after applying the Piranha cleaning yielded an estimation of the contact angle of slightly more than one degree. To determine the contact angle with water, the volume of a water drop is compared to the surface it covers after dropping it onto an iridium substrate, see Figure 4.6a. From that an estimation of the contact angle is deduced.

- During the post-processing steps, it is of major importance, that the substrate can withstand high temperatures. As described in section 4.3.3, during the preliminary tests with implanted nanodiamonds on a silicon substrate we encountered difficulties with diamonds on a silicon substrate as the sunk into the surface after annealing. In contrast, iridium withstands the high temperatures required for annealing without damage.
- Iridium acts both as a mirror and as an antenna for the fluorescence light emitted by the SiV center [?]. Therefore, the collection efficiency of the fluorescence light is enhanced.

At this point we comment upon a minor complication we experienced when using iridium surfaces. If the iridium layer is too thin, it tends to peel off the substrate, see Figure 4.6b. We encountered this problem during a cleaning procedure in the ultrasonic bath. However, this disadvantage is easily circumvented by using a thicker iridium layer. For our measurements, we used an iridium layer of a thickness of 130 nm, for which we did not encounter any adhesion problems.

#### 4.4.1 Preparation of The Substrate

As a preparatory step preceding drop-casting, the iridium substrate is cleaned. The standard cleaning procedure is comprised of the following cleaning steps in an ultrasonic bath. Each step is in effect for a duration of 3 min to 7 min:

- Distilled water with a drop of dishwasher detergent
- Isopropanol (99.9 % p.a.)
- Acetone (99.9 % p.a.)
- Distilled water

Thereafter, the substrates are put into a Piranha solution (50 % sulfuric acid  $H_2SO_4$ , 50 % hydrogen peroxide  $H_2O_2$ ) to enhance the surface hydrophilicity and therefore obtain a homogeneous distribution of diamonds on the surface. They are then put again into distilled water and blow-dried with compressed air to avoid residue from the water. The substrates were then either drop-casted or spin-coated with aqueous diamond solutions. For the former, the substrates are heated to a temperature of 60 °C and drops of a volume of about 5 µL are dropped onto the substrate. If substantially more than 5 µL is needed, then several drops of about 5 µL are dropped onto the substrate consecutively. A single large drop is ill-advised since the solution would flow off the substrate before drying. For spin-coating, a spin coater was built on-site used. Here, drops of 5 µL are dropped on the substrate and the spin-coater set to a velocity of 2500 rpm for 3 min.

Table 4.2: Listing of available wet-milled samples. The first column indicates the names of the samples, the second the mean diameter of the nanodiamonds, and the third designates how the silicon was incorporated into the diamond.

Sample name	Size	Si incorporation	Post-processing
hphtimp45	45 nm	<i>implanted</i>	oxidized in air at 450 °C
hphtimp80	80 nm	<i>in-situ</i>	annealed in vacuum for 1 h at 1000 °C and at 900 °C for 3 h
hphtimp260	260 nm	<i>in-situ</i>	oxidized in air at 450 °C
insitu50	50 nm	<i>in-situ</i>	series of individual samples with diverse post-processing steps
insitu70	70 nm	<i>in-situ</i>	series of individual samples with diverse post-processing steps
insitu70n	70 nm	<i>in-situ</i>	no post-processing subset of insitu70
insitu70o	70 nm	<i>in-situ</i>	oxidized in air at 450 °C subset of insitu70
insitu100	100 nm	<i>in-situ</i>	series of individual samples with diverse post-processing steps
insitu100ao	100 nm	<i>in-situ</i>	annealed in vacuum at 900 °C, consecutively oxidized in air at 450 °C subset of insitu100
implanted250ao	250 nm	implanted	annealed in vacuum at 900 °C, consecutively oxidized in air at 450 °C
hphtimp260	40 nm	implanted	annealed in vacuum at 1200 °C, consecutively oxidized in air at 450 °C
hphtimp260	50 nm	implanted	oxidized in air at 450 °C
hphtimp260	240 nm	implanted	annealed in vacuum at 1200 °C, consecutively oxidized in air at 450 °C
hphtimp260	260 nm	implanted	oxidized in air at 450 °C

## 4.5 Listing of available samples

---

---

## Chapter 5

# Quality of Nanodiamonds

### Remark:

Ich hab das kapitel jetzt nochmal ueberarbeitet indem ich den aufbau vom SiV papier hier uebernommen hab. Das gibt nochmal einen besseren ueberblick. Es gibt aber noch loecher die du nochmal dezidiert stopfen solltest. Besonders die section mit den post-processing methoden ist noch nicht auf dem niveau der anderen sections in dem kapitel.

- In der introduction werden qualitaetsprobleme genannt und ein paar methoden die da helfen sollen. Hier muss noch kurz erwähnt werden warum die methoden helfen.
- In der ersten section sind annealing und oxidation zusammen. Im text steht aber nur was annealing oder? Falls oxidation dann erst in der naechsten section kommt, sollte man die ueberschriften ändern. Ich kenn mich halt nicht aus, d.h. das passt noch nicht. Es muss auch klar werden welche probleme diese methoden potentiell loesen und warum.
- Was die surface treatments bewirken sollen bzw. wie die die qualitaetsprobleme minimieren? Da ist auch von shells die rede und ich hab keine ahnung was das fuer dinger sind. Hier fehlt auch noch was.
- Wenns um TEM messungen geht, dann ist hier auch von nanodiamond boundaries die rede. Hier sollte jetzt auch eine diskussion boundaries einfließen, bzw. was fuer negative effekte die haben koennen.

In this thesis we perform measurements of single SiV centers in wet-milled nanodiamonds. To this end, we require high quality diamond nanoparticles containing a single SiV center each. In this context we use the term quality as a measure of how close diamond crystals are to their pristine form. The presence of lattice imperfections such as additional vacancies, lattice strain, impurities or the inclusion of graphite or amorphous carbon is known to adversely affect crystal quality [?, ?, ?].

Surface contamination like graphite and amorphous  $sp^2$  hybridized carbon atoms manifest themselves as additional peaks in the Raman spectrum. Strain in the diamond lattice broadens the first order Raman peak and causes it to shift to higher or smaller wavenumbers. Similarly, high concentrations of lattice defects cause additional peaks, a broadening of the first order Raman peak and a shift towards smaller wavenumbers.

To improve crystal quality and to reduce the mentioned distracting effects the following methods are deployed here: Annealing in a vacuum, oxidation in air as well as surface treatments involving plasmas.

To study the effectiveness of these treatments and to gauge the quality of our nanodiamond samples we rely on Raman spectroscopy and TEM imaging. The former is used to detect strain, quantify defect concentration and the presence of carbon in non-diamond phases, while the latter enables imaging of individual nanodiamonds revealing details in crystallinity such as crystal boundaries.

Hier fehlt  
jew-  
eils ein  
kurzer  
satz  
was die  
dinger  
bewirken  
sollen.

## 5.1 Quality-improving Post-Processing Treatments

### 5.1.1 Annealing and Oxidation

During silicon implantation the diamond lattice gets damaged by the penetrating ions.  $sp^2$  bonds, carbon interstitials and vacancies disrupt the metastable equilibrium of the diamond phase. Hence, there is a tendency for damaged diamond to "tip over" to the thermodynamically stable form of carbon, i.e. graphite. At temperatures above about 500 °C, vacancies in the diamond lattice become mobile and diffuse towards the surface[?]. Literature suggests, that annealing at 900 °C for 1 h is sufficient to remove most of the damage following implantations, that however some damage remains even after annealing at 900 °C for 1 h. To reduce the damage in the diamond lattice, we anneal the implanted diamonds at 900 °C to 1200 °C for 3 h to 6 h in vacuum ( $10^{-6}$  Pa).

The surface of the nanodiamonds is contaminated with graphite and amorphous  $sp^2$  hybridized carbon . The vacancies which diffuse towards the surface during annealing further increase the amorphous carbon content on the surface of the nanodiamonds []. We apply oxidation in an oven under ambient air at a temperature of 450 °C for 3 h to 6 h.

warum

### 5.1.2 Surface Treatment With Gas And Plasma

We wanted to know whether surface treatment with different gasses had an influence on the emission properties, so we treated them with hydrogen ( $H_2$ ), oxygen ( $O_2$ ), ozone ( $O_3$ ) all both at room temperature and at 500 °C; and also with  $H_2$  plasma. However, we found that most nanodiamonds treated in this way only showed luminescence which immediately bleached when illuminated with a cw 660 nm laser even at low excitation powers of 200  $\mu$ W, or no luminescence at all. We double-checked with a CCD-image of the surface to be sure that there are nanodiamonds in the focus. This bleaching occurred so quickly, that after a scanning no spectrum could be taken. The only samples which did yield spectra with measurable ZPLs were the ones treated with  $H_2$ . However, also these SiV centers were not single ones. Therefore, we did not further investigate these samples.

One sample showed shells around the nanodiamond after oxidizing in air. We attribute this effect to a contamination in the oven. When we illuminated these nanodiamonds in the SEM for several moments, the shell went away. We therefore deduced that the shell is organic material. To get rid of the shells on the whole sample, we treated it with oxygen-argon plasma for 3 min<sup>1</sup>. After the first treatment, the shells were smaller, but not gone. So we

<sup>1</sup>Treatment performed by J. Schmauch, group of R. Birringer, Saarland University

put them into the oxygen-argon plasma again for 3 min, however, the shells were bigger than before any treatment. We tried another approach to get rid of the shells with ozon treatment for 4 h at 360 °C. Before ozon treatment there the diamond Raman line and other Raman lines visible. After surface treatment, more lines appeared and all of these other lines got more intense. There are probably organic contaminations on the sample in which functional groups got introduced by the ozon treatment. We did not further investigate this sample and defined it as broken.

## 5.2 Raman Measurements

Raman spectroscopy of various samples gives insight to crystal quality and surface contamination of nanodiamonds. Raman scattering is the inelastic scattering of a photon  $\hbar\omega_i$  on a molecule or crystal lattice in the initial state  $|i\rangle$  with energy  $E_i$ . The molecule or crystal transitions into a higher energy state  $E_f$  and the scattered photon with frequency  $\omega_s$  loses the energy  $\Delta E = E_f - E_i = \hbar(\omega_i - \omega_s)$ . Therefore, energy is exchanged between the photon and the excited matter, changing the rotational or oscillation energy of the involved molecule or the oscillation energy, i.e. phonons of the crystal lattice. The Raman shift is typically referenced in wavenumbers. It is given by:

$$\Delta\omega = \left( \frac{1}{\lambda_{ex}} - \frac{1}{\lambda_R} \right) \quad (5.1)$$

As every solid exhibits characteristic phonon modes tied to the properties of its lattice structure, Raman spectroscopy can be used to characterize diamond. Raman measurements of wet-milled nanodiamonds give insight into the issues of surface contamination, lattice strain and defect concentration: Surface contamination like graphite and amorphous sp<sup>2</sup> hybridized carbon atoms cause additional peaks in the Raman spectrum. A high defect concentration may lead to additional peaks, a broadening of the first order Raman peak and a shift to smaller wavenumbers. Strain in the diamond broadens the first order Raman peak and causes a shift to higher wavenumbers [?, ?, ?].

For the Raman measurements the same layout of the setup described in ?? is used. As excitation light source, a 532 nm continuous wave diode laser is used (IO). It provides single frequency mode laser light, a prerequisite for Raman investigations. The beamsplitter is a dichroic mirror (DRLP645), the laser light is additionally filtered out with a 532 Notch filter in the detection path in front of the single mode fiber instead of a longpass filter. With these adaptions, the combination of the confocal unit and the spectrometer serves as a Raman spectrometer. As the diamond Raman line is very narrow, the 600 grooves/mm grating is used as a starting point. Detailed measurements are realized using 1200 grooves/mm and 1800 grooves/mm gratings.

type

Since the size of single nanodiamonds is on the order of tens of nanometers, low signal intensities can become an issue when taking Raman measurements. To overcome this problem we pursue two different approaches:

- a) Nanodiamond Clusters: Collective measurements are carried out at several areas on the sample insitu70. Since this sample is densely covered with nanodiamonds, collective

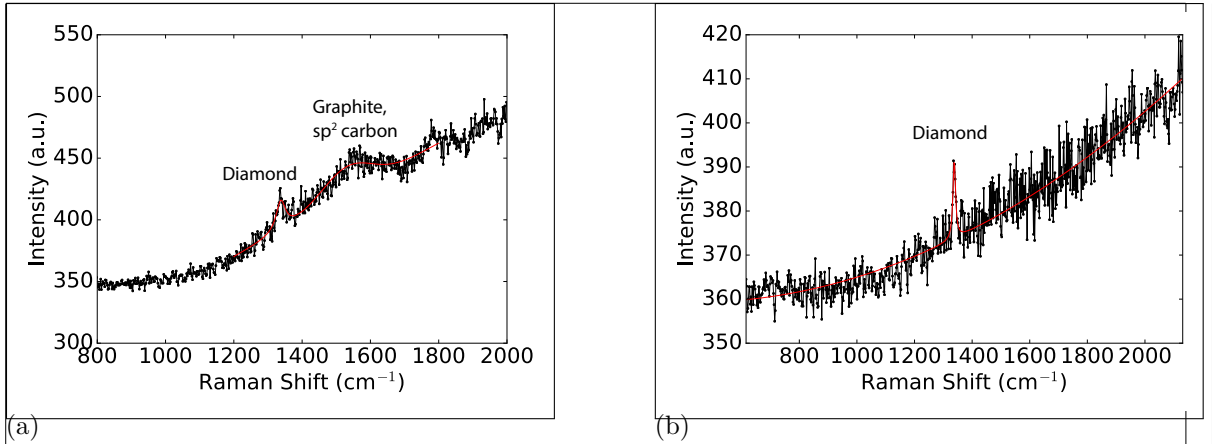


Figure 5.1: Raman measurements, black: data, red: fit. (a) Raman measurement before oxidation, sample insitu70. The diamond Raman peak is situated at  $1338\text{ cm}^{-1}$ . The broad feature around  $1580\text{ cm}^{-1}$  corresponds to the graphite G-band. (b) Raman measurement after oxidation, sample insitu70o. The G-band has vanished, indicating removal of graphite and amorphous  $\text{sp}^2$  hybridized carbon.

measurements of clusters of nanodiamonds (Figure 5.1a) achieves higher signal intensities.

- b) Big Nanodiamonds: Raman measurements are carried out on the implanted sample implanted250ao. For this sample, diamond particles are big enough to yield sufficient intensities on single nanodiamonds.

### 5.2.1 Surface Contamination

We test the impact of oxidation treatment as described in ?? on surface contamination. Figure 5.1a shows a measured Raman spectrum of a sample without oxidation treatment (insitu70n). To verify reproducibility, the measurement is performed on three different spots of the sample. The narrow peak in Figure 5.1a corresponds to the first order diamond Raman peak and will be further analyzed in ?? . The spectrum also shows a broad peak with a Raman shift of about  $(1582 \pm 5)\text{ cm}^{-1}$ . This shift corresponds to the G-band due to amorphous  $\text{sp}^2$  hybridized carbon atoms and graphite. The exact G-band position and linewidth is sensitive to parameters such as the clustering of the  $\text{sp}^2$  phase, bond-length and bond-angle disorder, presence of  $\text{sp}^2$  rings or chains, and the  $\text{sp}^2/\text{sp}^3$  ratio [?]. The nanodiamond Raman spectra are considerably modified after oxidation in air at  $450\text{ }^\circ\text{C}$ . To verify this, we perform Raman measurements on three different spots of a sample produced in the same process as the above mentioned, which is additionally oxidized (insitu70o). While the G-band peak is present in every measurement performed on a non-oxidized sample, it is not present in any of the oxidized samples (Figure 5.1b), indicating successful removal of  $\text{sp}^2$  hybridized carbon and surface graphite.

### 5.2.2 Defect Concentration

Several effects impact the first order diamond Raman line: 1. defects in the diamond lattice, 2. hydrostatic pressure, 3. uniaxial or more complicated stress configurations. In the measurement on nanodiamond clusters the width of the diamond Raman peak of sample insitu70 varies between  $15\text{ cm}^{-1}$  and  $30\text{ cm}^{-1}$  without oxidation treatment, but is only  $9\text{ cm}^{-1}$  to  $11\text{ cm}^{-1}$  after the oxidation process. A possible reason for this change of the width is improved crystal quality [?]. In the measurement on big nanodiamonds we measured a Raman line at  $(1308 \pm 5)\text{ cm}^{-1}$  (denoted line R1) which exhibits a broad linewidth of  $(25 \pm 5)\text{ cm}^{-1}$ . One plausible explanation for both the position and the linewidth of the Raman line are defects in the diamond lattice[?].

### 5.2.3 Lattice Strain

We investigated how strain in the diamond lattice manifests itself in both measurements on nanodiamond clusters and on big nanodiamonds. In the Raman measurement on nanodiamond clusters, the position of the diamond Raman peak is the same for oxidized (insitu70o) and non-oxidized (insitu70n) samples, indicating that oxidation does not affect strain in the diamond. However, the Raman shift of both non-oxidized and oxidized samples amounts to  $(1338 \pm 5)\text{ cm}^{-1}$ , as compared to the literature value of  $1332.5\text{ cm}^{-1}$  of pristine diamond [?] (given uncertainties are governed by spectrometer resolution). This shift indicates the presence of strain in the diamond particles.

Performing the Raman measurement on big nanodiamonds we found one diamond Raman line at  $(1308 \pm 5)\text{ cm}^{-1}$  (line R1), one at  $(1345 \pm 5)\text{ cm}^{-1}$  (line R2) and one at  $(1348 \pm 5)\text{ cm}^{-1}$  (line R3), indicating a broad distribution of strain among the individual diamond particles (uncertainties governed by spectrometer resolution). Only line R1 can be explained with a high defect concentration in the diamond lattice due to its shift to smaller wavelengths. However, a more consistent model which explains all occurring shifts is the presence of strain in the diamond nanoparticles. From the linewidths in the measurement on big nanodiamonds, the strain in the diamond is calculated using the equation for hydrostatic pressure [?]

$$\omega(P) = \omega_0 + a_1 P + a_2 P^2, \quad (5.2)$$

where  $\omega_0 = 1332.5\text{ cm}^{-1}$ ,  $a_1 = 2.83\text{ cm}^{-1}\text{ GPa}^{-1}$  and  $a_2 = -3.65 \times 10^{-3}\text{ cm}^{-1}\text{ GPa}^{-1}$ . The calculation yields a pressure in the investigated diamonds of  $-8.56\text{ GPa}$  tensile stress and  $4.26\text{ GPa}$  and  $5.50\text{ GPa}$  compressive stress. Pressure uncertainties due to the Raman line measurements are smaller than one Pascal and are therefore neglected. Under hydrostatic pressure, the triply degenerate first order Raman peak remains degenerate, while under uniaxial and more complex stress configurations (biaxial stress, shear stress etc.) mode splitting occurs [?]. As mentioned above, we observe broad linewidths up to  $(25 \pm 5)\text{ cm}^{-1}$ . The broad linewidths of the Raman lines may be attributed to uniaxial strain, as mode splitting manifests itself in a broadening of the peak due to limited spectrometer resolution. Therefore, we conclude that both hydrostatic and uniaxial strain is present in the nanodiamonds.

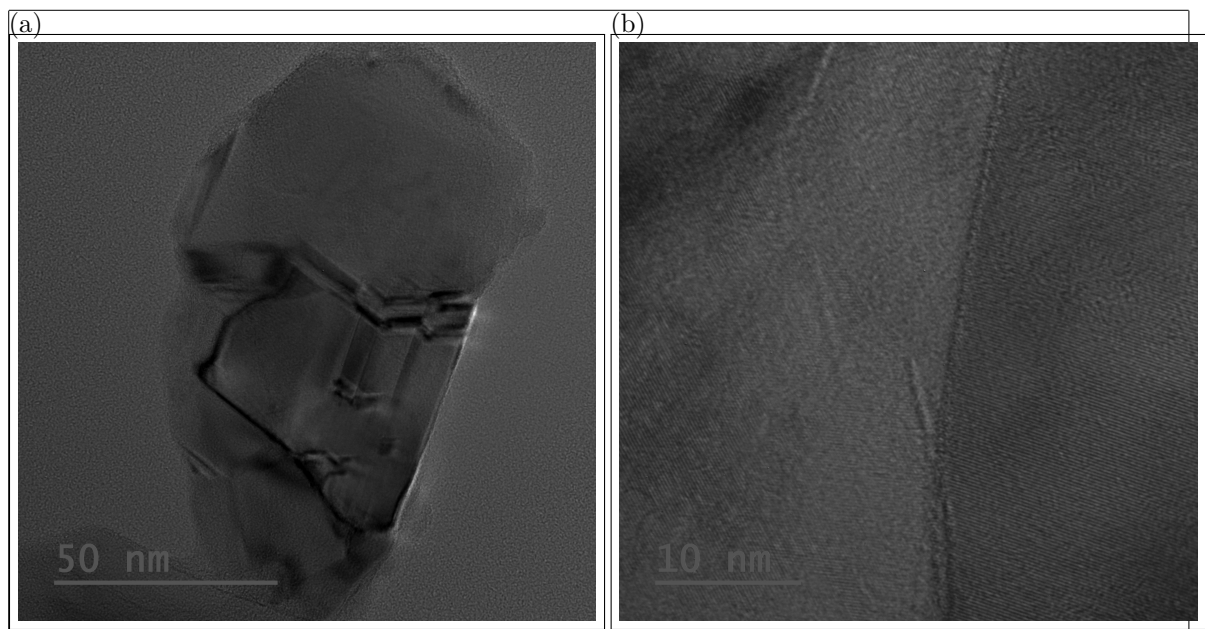


Figure 5.2: Transmission electron microscopy (TEM) pictures of sample insitu100. (a) Image of a single nanodiamond particle. Several crystal boundaries can be seen within the diamond particle. (b) Close-up image a diamond particle. The vertical line is a crystal boundary, to the left and right the more or less horizontal layers of one crystalline region can be seen.

### 5.3 Transmission Electron Spectroscopy Measurements

Transmission electron microscopy (TEM, also sometimes conventional transmission electron microscopy or CTEM) is a microscopy technique in which a beam of electrons is transmitted through a specimen to form an image. The specimen is most often an ultrathin section less than 100 nm thick or a suspension on a grid. An image is formed from the interaction of the electrons with the sample as the beam is transmitted through the specimen. During transmission electron microscopy a beam of electrons is transmitted through a sample, forming an image of the transmitted sample. Since electrons have higher de Broglie wavelengths than photons, a higher resolution is obtainable, allowing the surface of nanodiamonds to be resolved. Thus, the crystallinity of single nanodiamonds can be studied directly.

#### 5.3.1 Crystallinity and Grain Boundaries

Sample insitu100 was investigated using TEM by J. Schmauch, group of R. Birringer, Saarland University. Smaller nanodiamonds would have been too small for the carbon grid which serves as a sample holder in the TEM, and might have fallen through the grid and bigger particles would have been too big to be transmitted by the electron beam, making the imaging impossible. In Figure 5.2 there are TEM images, one of them exhibits a single diamond particle and the other is a close-up image of a crystal boundary. From Figure 5.2a it can be seen that the diamond particle contains several crystallites and crystal boundaries. The edges of the crystallites are the sharp features within the diamond particle, the crystal boundaries the smoother features. In Figure 5.2b the crystal layers which are more or less horizontal and in

### 5.3. TRANSMISSION ELECTRON SPECTROSCOPY MEASUREMENTS 5. QUALITY

more or less the middle of the picture there is a vertical line which is the edge of a crystallite. So it is clear that the investigated sample does not contain beautiful single crystal diamond particles, which means a reduction of the crystal quality of the diamond particles.

---

---

## Chapter 6

# Spectral Distribution of SiV centers in Nanodiamonds

In this chapter we report on our results regarding luminescence properties of SiV centers. The samples used in our investigation consists of a large set of CVD nanodiamonds containing *in-situ* SiV centers of a size in the range of 70 nm to 100 nm. Throughout the chapter we refer to samples using their distinct sample-id as listed in ??.

The obtained fluorescence spectra of SiV centers show that both the center wavelength of the ZPL as well as the linewidth of the zero-phonon-line vary strongly among different samples. Our measurements over a large set of SiV centers indicate a strong correlation between the center wavelength of the zero-phonon-line and the corresponding linewidths, resulting in a previously unreported bimodal distribution. We assert single photon emission from these SiV centers across the whole range of zero-phonon-line positions and linewidths. Furthermore we detect fluorescence intermittency, i.e. blinking. The obtained data for the bright and dark times indicate an exponential decay of the dark state and a log-normal decay of the bright state, the latter of which has to our knowledge not been reported as of yet.

### 6.1 Photoluminescence spectra

To identify nanodiamonds containing SiV centers, we performed confocal scans of the samples. To reduce bias in the measurements, not only the brightest spots of the confocal scans are investigated, but also those which barely exceed background fluorescence. SiV centers are further investigated by measuring photoluminescence (PL) spectra, single photon statistics and photostability. As discussed in chapter 2, the typical luminescence spectrum of an SiV center is composed of a prominent zero-phonon-line peak and weak sidebands. Investigations of both are reported independently in the following paragraphs.

#### 6.1.1 Zero-phonon-line

The center wavelength and the linewidth of the zero-phonon-line (ZPL) of SiV luminescence spectra for samples insitu50, insitu70, and insitu100 are determined by fitting a Lorentzian

fit to the ZPL. Both spectra from single and multiple SiV centers are taken into account. In Figure 6.1 the linewidth for each measured ZPL is plotted against its center wavelength.

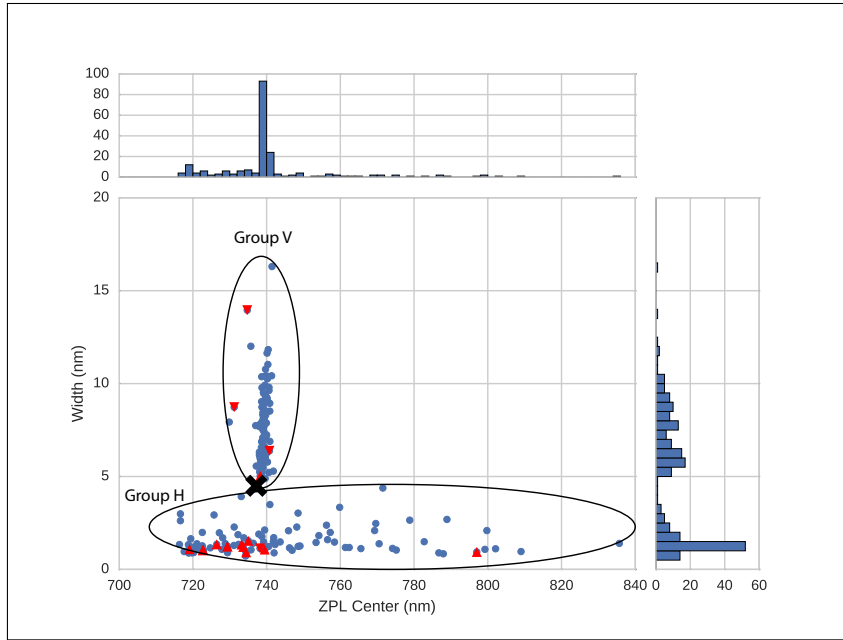


Figure 6.1: Distribution of the ZPL center wavelength versus the linewidth of the ZPL of the investigated SiV centers in milled nanodiamonds containing *in-situ* incorporated SiV centers for samples insitu50, insitu70, insitu100. The data separates into a horizontal (group H) and a vertical (group V) cluster. The bold black cross marks the position of an ideal SiV center in unstrained bulk diamond [?]. The red triangles indicate emitters with an antibunching dip in the  $g^{(2)}(0)$  measurement. Upwards pointing triangles represent blinking emitters (fluorescence intermittency), while triangles pointing down represent non-blinking emitters (see section 6.3).

What immediately strikes the eye is a pattern that to our knowledge has not been reported to date: The observed ZPLs partition into two groups, denote a horizontal lobe (group H) and a vertical lobe (group V). The two lobes are separated by a gap, i.e. a region with a pronounced lack of data points. Single emitters are identified both in group H and group V, marked as red triangles in Figure 6.1. Further details on single emitters are given in section Figure 6.2. The two groups are defined by their characteristic center wavelengths and linewidths: In group H very prominent ZPL peaks are found showing linewidths in the range of 1 nm to 5 nm and center wavelengths in the range of 715 nm to 835 nm. Figure 6.2a shows a representative spectrum of a single emitter in group H (denoted emitter H1), exhibiting a ZPL line width of 1.4 nm and a center wavelength of 726.5 nm. In contrast, in group V, the spectra exhibit broader ZPL linewidths of approximately 5 nm up to 18 nm. Their ZPL center wavelengths, however, are distributed within the very narrow range of 738 nm to 741 nm. Figure 6.2b shows a spectrum of a single emitter of group V (denoted emitter V1) with a ZPL linewidth of 6.4 nm and a center wavelength of 740.8 nm. For comparison, the room temperature ZPL of SiV centers in unstrained bulk diamond exhibits a linewidth of 4 nm to 5 nm and a center wavelength of 737.2 nm marked with a black cross in Figure 6.1 [?, ?].

To determine how much the ZPLs contribute to the total observed emission of emitter H1 and emitter V1, we determine the Debye-Waller factors for both. The Debye-Waller factor

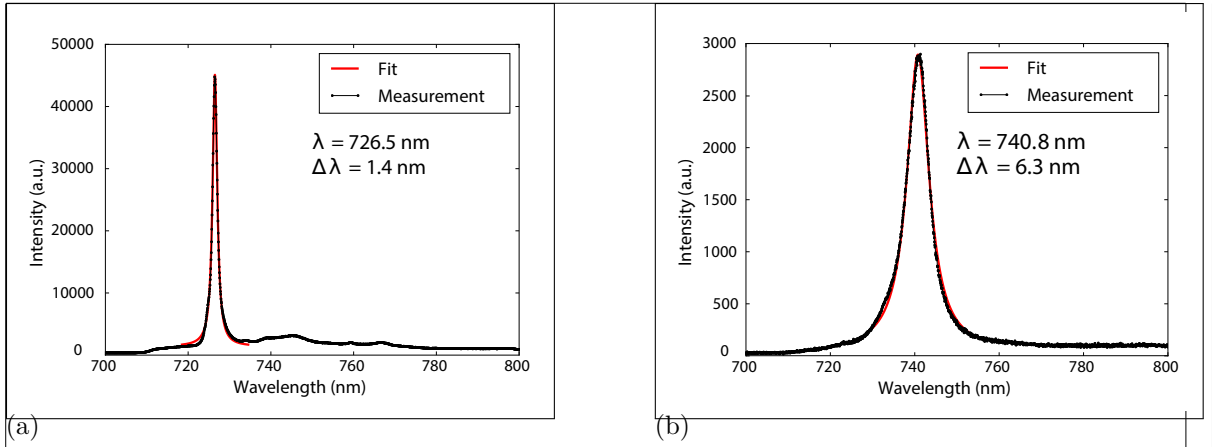


Figure 6.2: Representative photoluminescence spectra of sample insitu100ao measured at room temperature. (a) Spectrum of group H of Figure 6.1, denoted emitter H1. (b) Spectrum of group V of Figure 6.1, denoted emitter V1. The red lines are Lorentzian fits to the peaks.

is defined by  $DW = I_{ZPL}/I_{TOT}$  and is therefore suited as a measure for sideband intensity. The Debye-Waller factor for emitter H1 amounts to  $0.81 \pm 0.01$  (given uncertainty due to fit). This Debye-Waller factor corresponds to a Huang-Rhys factor  $S = -\ln(DW)$  [?] of  $0.21 \pm 0.01$ , which is in good agreement with the values reported in [?]. The error is mainly due to background corrections. When zooming in onto the spectrum of emitter V1 we do not find distinct sidebands peaks, i.e. almost all emission for this emmiter is allotted to the ZPL. Considering resolution limits of the spectrometer, darkcounts and fluorescence background, we evaluate the Debye-Waller factor to be larger than 0.97. It is the largest Debye-Waller factor amongst all our milled SiV centers. The two mentioned Debye-Waller factors should not be interpreted as single representative emitters for the respective groups, they rather serve as an orientation of the spread of the Debye-Waller factors of both groups. It has to be pointed out, that we did not find any systematic difference of the Debye-Waller factor between group H and group V.

To provide context for the novel findings presented in Figure 6.1, we compare our results to various earlier findings. Furthermore, we discuss an additional comparison to an investigated control sample fabricated using silicon implantation. The results are presented in Figure 6.3.

Samples for which previous data has been taken are:

1. nanodiamonds produced by bead-assisted sonic disintegration (BASD) of polycrystalline CVD diamond films (blue rings in Figure 6.3 [?]; data taken from [?])
2. nanodiamonds produced directly via a CVD process with *in-situ* incorporated SiV centers; measured in a spectral filter window of 730 nm to 750 nm (blue squares in Figure 6.3; data reused from [?] with permission)
3. nanodiamonds produced in the same manner as the CVD sample in 2 (blue downwards pointing triangles in Figure 6.3; produced by M. Schreck [?]; spectroscopic measurement performed with setup described in ??)

All previous data from different nanodiamond material fit nicely with the ZPL distribution presented in Figure 6.3, confirming the findings of Figure 6.1.

We verify that the observed luminescent defects are indeed silicon related by performing con-

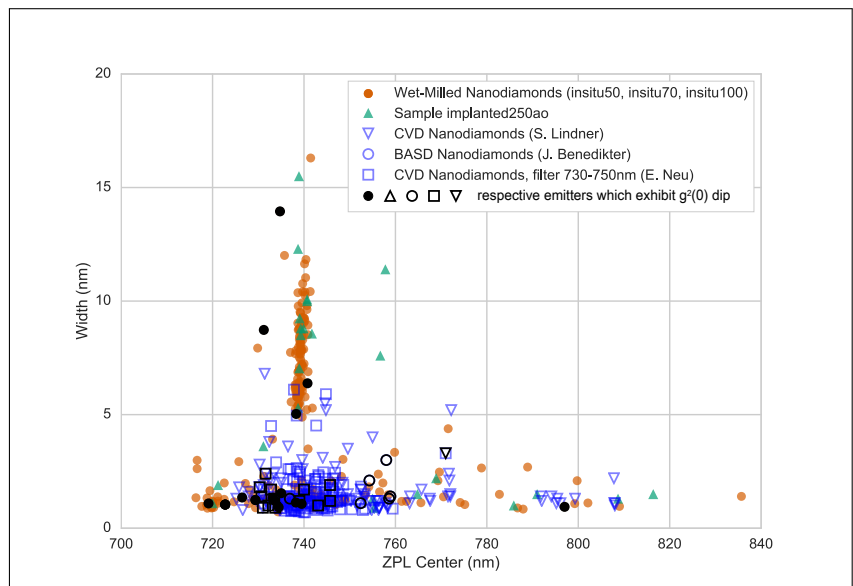


Figure 6.3: Comparison of the distribution of the linewidth vs. the center wavelength of the ZPL of the investigated SiV centers in milled nanodiamonds (samples insitu50, insitu70, insitu100) with data measured on sample implanted250ao (implanted with Silicon); with data measured in our group on CVD nanodiamonds produced by M. Schreck [?]; with data measured on nanodiamonds reported by J. Benedikter in [?]; and with data measured in CVD diamonds by E. Neu in a filter window between 730 nm and 750 nm [?]. Black symbols represent emitters exhibiting a dip in the  $g^{(2)}(0)$  function, indicating a single or very few SiV centers

trol experiments with silicon implanted samples (sample implanted250ao). By doing so we rule out the possibility that the two lobes in the distribution are a result of artifacts. Such artifacts include other elements incorporated into the nanodiamonds during the growth process: Residue from previous processes performed in the diamond growth chamber or material from chamber parts may be incorporated during nanodiamond growth. Figure 6.3 shows that the implanted SiV centers cover roughly the same spectral range as the *in-situ* incorporated centers from around 720 nm to 820 nm as the *in-situ* incorporated centers. This correlation provides strong evidence for the silicon related origin of the defects.

To provide a theoretical interpretation, the ZPL center wavelength shift is investigated in further detail and compared to results from density functional calculations. Zooming in to group V (Figure 6.4a) it becomes clear that only six of the measured data points in group V are situated at a shorter center wavelength than the point attributed to an ideal SiV center in unstrained bulk material. The shortest wavelength shift is at 729.9 nm. At the same time, much more data exhibit a center wavelength bigger than the ideal SiV center. This asymmetry suggests that a red-shift of the ZPL of an SiV center is significantly more likely than a blueshift.

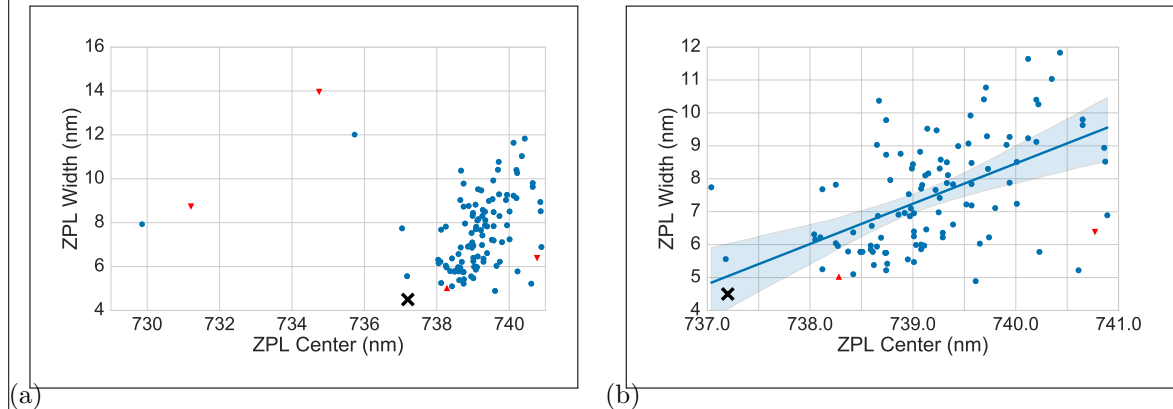


Figure 6.4: (a) A zoom into group V. While many data points exhibit higher center wavelengths (i.e. a redshift) than the ideal SiV center in bulk, only few exhibit shorter center wavelengths (i.e. a blueshift). (b) Zooming further into group V, a clear trend of broader ZPL linewidths for larger ZPL center shifts is visible. The line is a linear regression to all datapoints between 737 nm and 741 nm which exhibit a linewidth bigger than 4 nm.

Several mechanisms contribute to the center wavelength shift, predominantly hydrostatic- and material strain. As explained in ??, we measured the Raman shift of samples insitu70 and implanted250ao. These measurements indicate strain in the diamond lattice in the range of  $-8.56 \text{ GPa}$  to  $4.26 \text{ GPa}$ . Figure 6.5 shows results from density functional calculations. The shift of the ZPL is modelled in dependence of pressure in the diamond lattice both for hydrostatic stress and for uniaxial stress. Figure 6.5 illustrates that the assumption stated in ??, namely that the strain in the nanodiamonds is due to hydrostatic and uniaxial stress, corresponds well with the measured ZPL shifts in group V.

With higher uniaxial pressure, the ZPL becomes more and more red-shifted. The blueshifted ZPL center wavelengths are explained by hydrostatic stress in the diamond material. The strain calculated from the Raman measurements corresponds well with the results in Figure 6.5 for group V. However, the measured shifts in group H are too broad to be solely explained by strain in the diamond. A potential explanation for the very broad distribution of defect

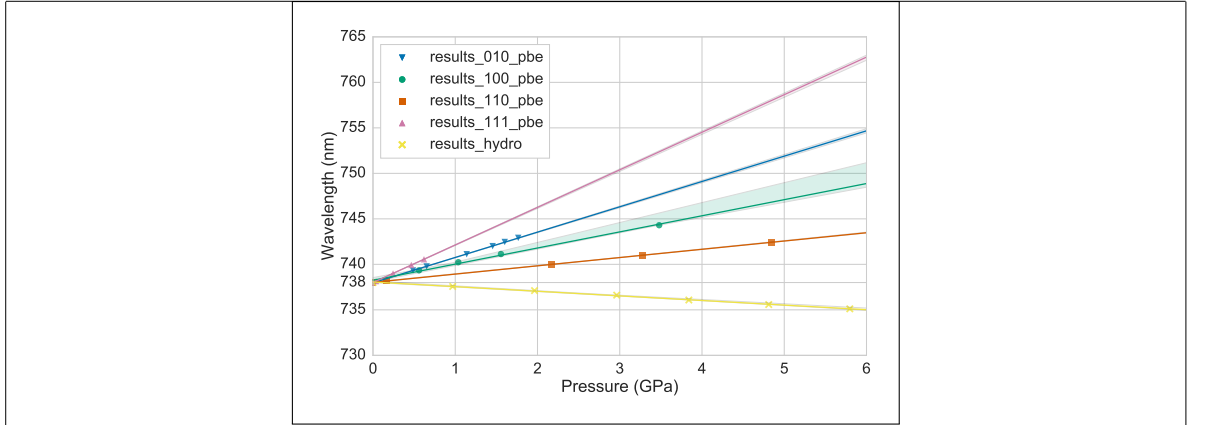


Figure 6.5: Calculations of the wavelength of the SiV center ZPL in dependence of pressure. Markers: calculated pressure with PBE functional; Lines: linear fits to the calculated points, the shaded area around the lines representing the one sigma (68%) confidence intervall. Yellow: hydrostatic pressure; other colors: uniaxial pressure, for different orientations. All calculations are performed with a PBE functional. Hydrostatic-type pressure causes a moderate blue shift whereas uniaxial strain causes larger redshift with different magnitudes depending on the direction of the strain

center ZPL center wavelengths could be the association of SiV centers with a further nearby defect, such as a vacancy, or a modified SiV complex such as SiV:H [?].

Zooming in to group V, another effect becomes visible (Figure 6.4b): With increasing ZPL center wavelength, the linewidth becomes broader. As discussed above, a red-shift of the ZPL is linked to increasing uniaxial strain. Thus we conclude that the ZPL linewidth too is affected by strain in the diamond lattice. Here, a modified electron-phonon coupling [?] causes increased uniaxial stress, resulting in larger linewidths. A similar effect has been previously observed for SiV centers at cryogenic temperatures [?].

To conclude, we are able to explain the distribution of ZPL center wavelengths in group V very consistently with theoretical predictions based on perturbative shifts due to strain in the diamond lattice. On the other hand, we have to assume that group H is comprised of modified SiV centers, the structure of which is currently unclear.

### 6.1.2 Sideband

It is known that the photoluminescence spectra of SiV centers in nanodiamond are dominated by the zero-phonon-line. As a result phonon side band contributions remain small, a fact expressed in large Debye-Waller factors of over 70 % established previously [?, ?]. Our own measurements are consistent with these of emitter H1 and emitter V1 results. We also find distinct sideband peaks in many SiV center photoluminescence emission spectra. The investigated emitters exhibit two different structures of sideband spectra: The spectra in group V exhibit one strong sideband peak, spectra in group H exhibit several weaker sideband peaks. Figure 6.6a and Figure 6.6b illustrate the respective observations.

Most of the spectra in group V exhibit a characteristic shape, composed of the ZPL and one strong sideband peak. 70 % of the photoluminescence spectra with one distinct sideband peak exhibit a shift of the sideband peak from the ZPL between 37 meV to 43 meV. The range of

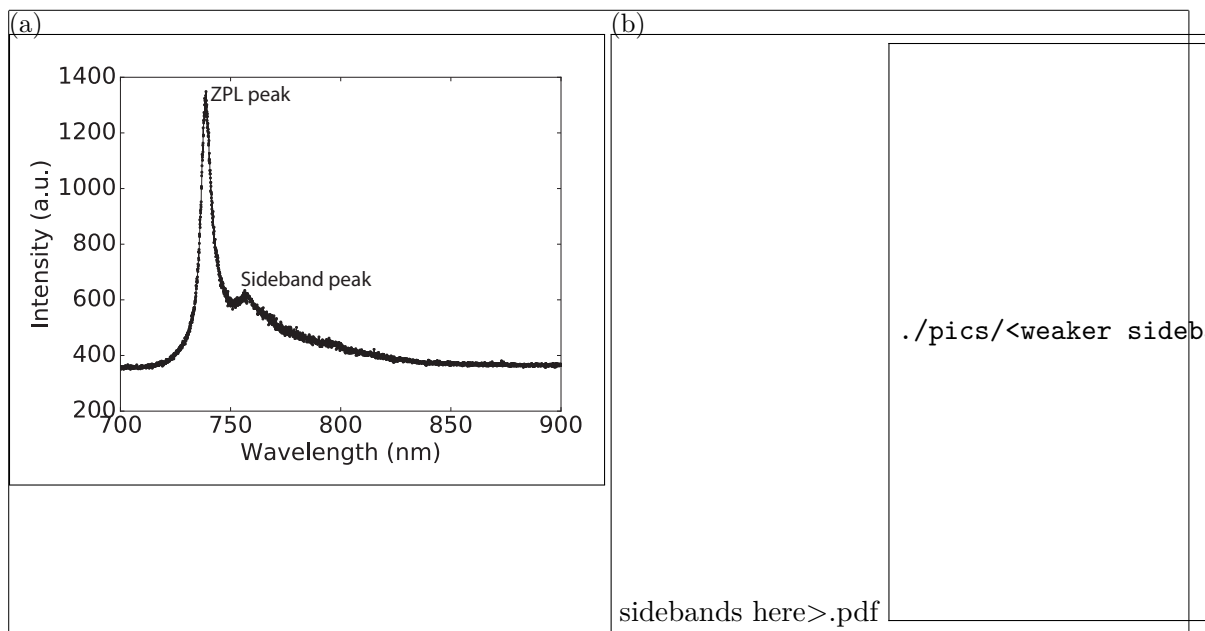


Figure 6.6: Representative spectra of emitters showing single (a) and multiple (b) side band peaks. The former belong to group V, while the latter are members of group H.

line shifts for the prominent sideband peak coincides with a well-known feature at 42 meV, associated with SiV centers [?, ?], but also to a larger number of optically active defects [?]. The occurrence of this 42 meV sideband feature for a large number of defects and the absence of isotopic variations [?], favors an assignment as non-localized lattice vibration. We furthermore observe that the dominant sideband peak shifts towards smaller distance from the ZPL for increasing ZPL center wavelength, i.e. increasing strain. Figure 6.7 presents a linear fit to data for emitters in group V.. The low phonon energy of the sideband feature and its shift with strain might arise from a local “softening” of the crystal lattice in the vicinity of a defect [?].

A recent study [?] suggests that the 42 meV mode, similar to other broad phonon side band features, originates from a resonance attributed to phonons causing the dynamical Jahn-Teller effect with SiV centers [?]. As the Jahn-Teller coupling varies with strain it is also expected that the resonance shifts accordingly.

In the spectra of group V, we do not observe a typical SiV center sideband feature at 64 meV, attributed to a local vibration of the silicon atom, frequently much stronger than the 42 meV sideband peak. A possible explanation is, that the lattice mode at 37 meV to 43 meV is so strong that the local vibrational mode at 64 meV cannot be separated from the tail of the lattice mode.

In group H we observe many spectra which exhibit several peaks within the spectral range of our detection range between 710 nm to 900 nm. The challenge arises to unequivocally distinguish between peaks stemming from a phonon sideband and peaks stemming from shifted, less intense SiV center ZPLs.

Interestingly, we assert a tendency for peaks to accumulate at a shift of around 43 meV, 64 meV, 150 meV and 175 meV. This pattern in the phonon side band of group H is consistent

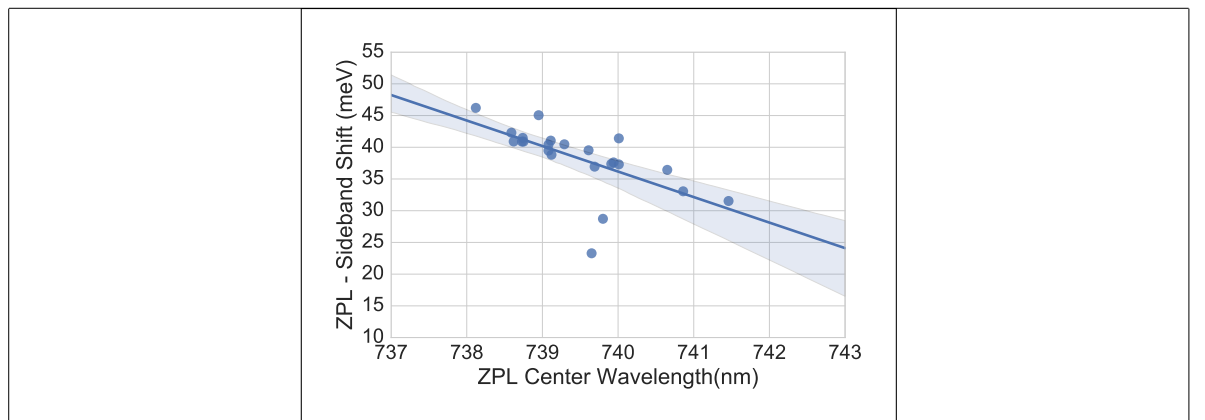


Figure 6.7: Shift of dominant sideband peak from the ZPL in spectra of SiV centers (group V, samples insitu50, insitu70, insitu100) vs. ZPL center wavelength. The linear fit shows that the shift decreases with increasing ZPL center wavelength, i.e. with increasing strain and exhibits a slope of  $(-4 \pm 1) \text{ meV nm}^{-1}$ . The shaded area is the 95 % confidence region.

with side band shifts reported in [?, ?, ?].

The possibility exists, that some these peaks believed to be phonon side bands are actually shifted ZPLs stemming from other SiV centers. To address this question, we perform photoluminescence measurements at cryogenic temperatures.

### 6.1.3 Cryostatic Measurements

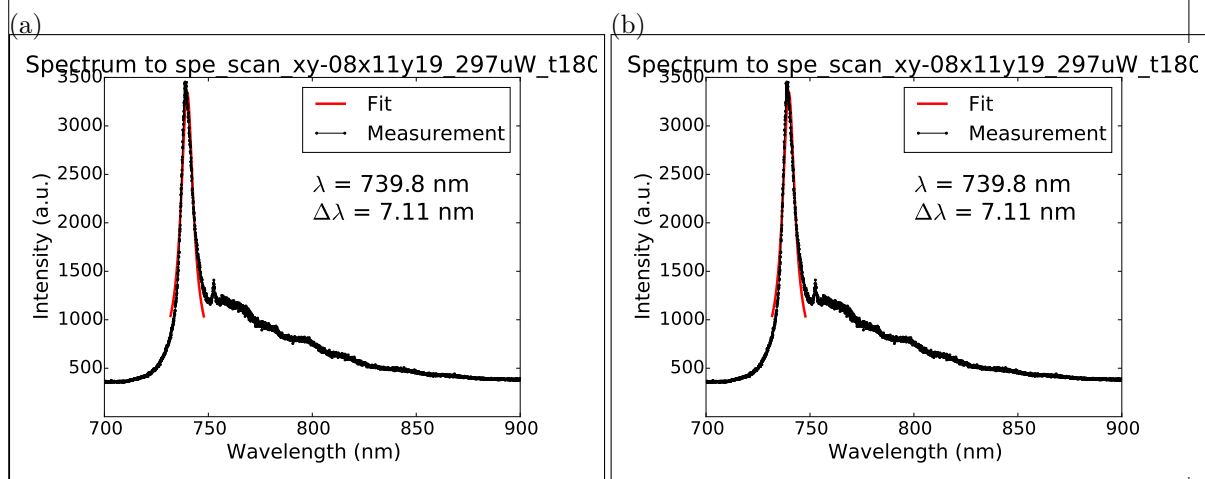


Figure 6.8

#### Remark:

den teil mit den cryogenic measurements musst du nochmal ordentlich aufschreiben. Hier fehlen noch dinge.

- Wie hast du messungen ueberhaupt machen koennen? Das setup in ?? spricht ja

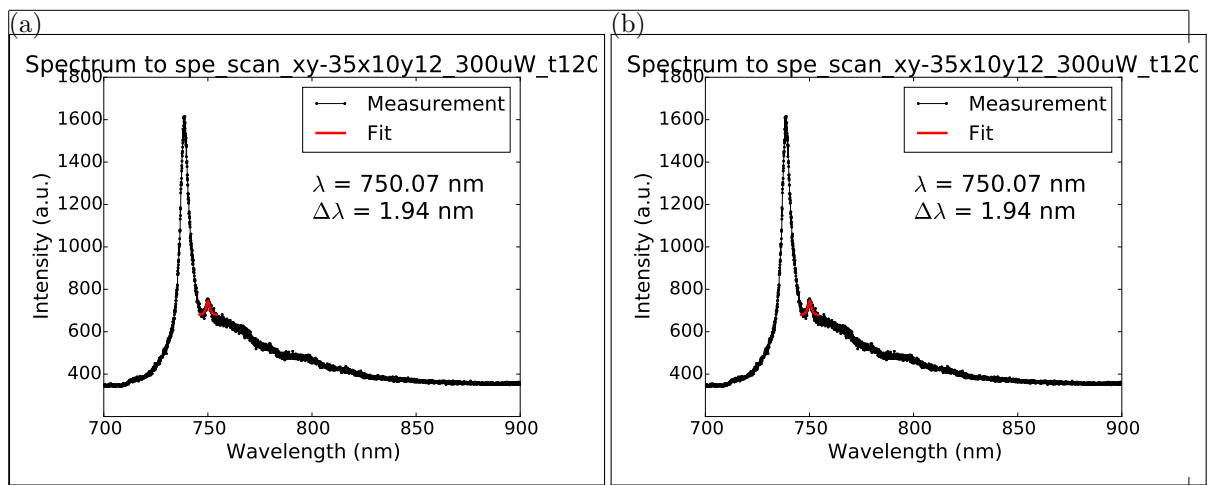


Figure 6.9

nicht von tieftemperaturen. Hast du den aufbau von jemand anderem (janine?) benutzt? Wenn ja dann unbedingt erwähnen. Ansonsten erklären wie sich der genutzte aufbau vom normalen unterscheidet.

- die Bilder die du da bereits eingefügt hast, die versteh ich nicht. Sind das nur Platzhalter und da kommt noch was anderes hin? Ich sehe den Zusammenhang die Geschichte mit der Feinstruktur nicht. Das sollte noch erklärt werden.
- wenn man die 4-fach Aufspaltung nicht sieht und stattdessen mehrere Linien hat, was bedeutet das? Klar ist, man hat kein einzelnes SiV Center am Start. Abgesehen davon, lässt sich noch was anderes sagen? Wenn man den Wood vor lauter Lines nicht sieht, dann heißt das auch, dass man nicht sagen kann ob manche der Phonon Side Band Peaks von anderen SiV Centers kommen oder nicht. Wenn hier keine konklusive Aussage möglich ist, dann sollte das diskutiert werden.
- die Sache mit den multiple lines that were strained ist mir nicht klar. Soll das heißen die waren verschoben und der Grund dafür war strain? Wenn ja, verschoben gegenüber welchem Wert, man erwartet ja 4 Linien für SiV Centers.

We performed some cryostatic measurements to pursue two goals: First, if we see the four-level splitting of the ZPL this is further proof that the dominant peaks of our spectra are indeed all due to SiV centers and do not stem from other impurities. Second, if the sideband peaks vanish at cold temperatures, this is evidence that they are caused by phonons. So we cooled down a sample, but all we saw was a wood of lines. Apparently, there were multiple SiV centers in the nanodiamonds and they were all strained, messing up the four-level line structure.

## 6.2 Photon correlation measurements

**Remark:**

Ich hab hier mal die paperversion hinkopiert. Mir ist aufgefallen, dass du in der diss version noch andere plots mit erklaerungen hattest. Ich schlage vor du fuegst das was in der neuen noch fehlt einfach ein. Dann ist sichergestellt, dass wir den text aus dem paper konsistent erweitern. Der alte text ist auskommentiert vorhanden.

The investigated SiV centers exhibit count rates of a few thousand to a few 100 000 counts per second (cps). We carried out measurements of the photon statistics and found that about 3 % of luminescent nanodiamonds contain single color centers. These measurements show, that the probability of finding a single emitter does not correlate in any way with the center wavelength or the linewidth of the ZPL. We found several single SiV centers with an antibunching dip down to about 0.2 and attribute the residual  $g^{(2)}(0)$  value to background fluorescence from the diamond host. For the utilized nanodiamonds a background measurement without simultaneously measuring SiV center photoluminescence is infeasible, because the laser spot size is bigger than the nanodiamond, i.e. the SiV center will always be excited when the nanodiamond is illuminated. Therefore, the background is estimated from the sideband of SiV center spectra. The measured lifetimes of the single SiV centers are in the range of about 1 ns to 9 ns, which is of the same order as previous research suggests [?, ?]. Figure 6.10 shows the  $g^{(2)}$  functions of the two emitters introduced in ??, emitter H1 and emitter V1.

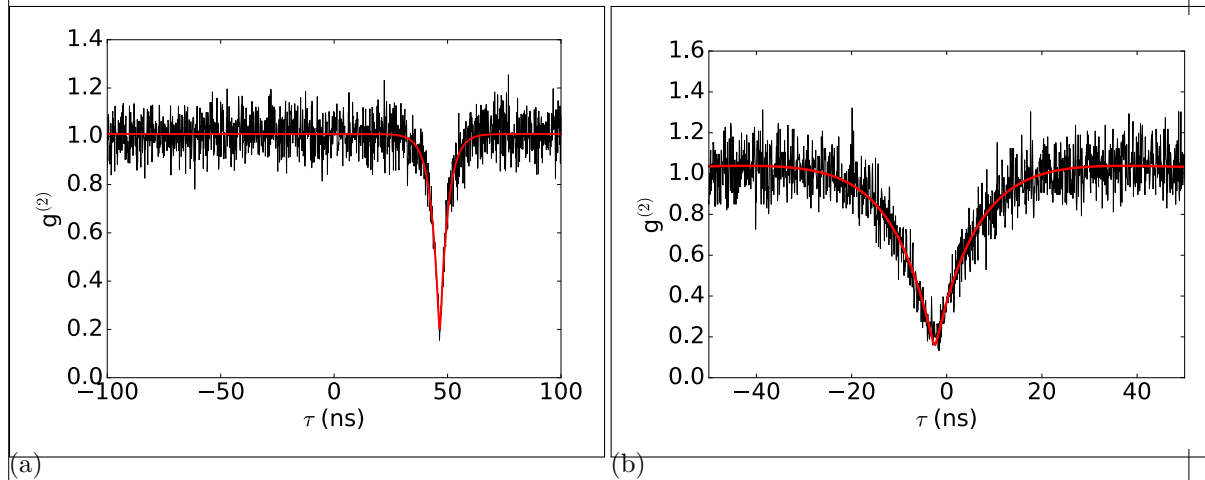


Figure 6.10: (a) Intensity autocorrelation function of an emitter in group H. (b) Intensity autocorrelation function of emitter V1 at an excitation power of 200  $\mu\text{W}$ (saturation power is 1 mW).

Figure 6.10a shows the photon correlation function of an emitter in group H. The shift of the dip to  $\tau = 50$  ns originates from a path length difference of the two detection paths in the Hanbury Brown and Twiss setup. The  $g^{(2)}(0)$  value of the fit is 0.20. The excited state lifetime of the emitter was determined to be  $(3.8 \pm 0.1)$  ns.

Figure 6.10b shows the  $g^{(2)}$  function of emitter V1 at an excitation power of 200  $\mu\text{W}$ , which is 20 % of the emitter's saturation power  $P_{sat} = (1.0 \pm 0.1)$  mW. The  $g^{(2)}(0)$  value yields 0.16. It is a representative  $g^{(2)}$  measurement of single SiV centers. It is well below 0.5, indicating single photon emission. The non-vanishing  $g^{(2)}(0)$  value is caused by background fluorescence of the diamond. The lifetime of the excited state of this emitter is  $(9.2 \pm 0.2)$  ns. It is the highest excited state lifetime we measured within this work.

Several nanodiamond photoluminescence spectra contain multiple narrow distinct peaks at different wavelengths. This circumstance is attributed to nanodiamonds containing more

was soll  
ich als  
saetti-  
gungsleis-  
tung  
angeben,  
emitter  
starb vor  
messende

than one SiV center, each of which is subject to a different ZPL wavelength shift. We choose narrow bandpass filters to perform independent measurements of each individual peaks of such a spectrum. As a result it is possible to measure  $g^{(2)}(0)$  values below 0.5 for each of these narrow peaks. Hence the individual peaks are identified as single emitters with a different ZPL center wavelength.

We do not see a systematic difference regarding the photon autocorrelation functions of group H and group V, both reach similar  $g^{(2)}(0)$  values. Also, the timescales of the excited state lifetimes coincide.

## 6.3 Photostability

### Remark:

Auch hier hab ich einfach mal den gut formulierten text vom paper hineinkopiert. Wenn du aus dem alten text noch sachen einfuegen willst, dann gern. Ich hatte hier den eindruck, dass so ziemlich alles schon da ist, aber vielleicht taeusch ich mich.

As mentioned in the previous section, the single photon count rates observed from the investigated SiV centers varies strongly between a few thousand to a few 100 000 cps. To further investigate the count rate, the luminescence time trajectory of the emitters which exhibit a dip at  $g^{(2)}(0)$  is evaluated. It is found that some of the observed emitters exhibit fluorescence intermittence, also called blinking. Figure 6.11 illustrate the effect. Blinking is attributed to temporal ionization of the color center during optical excitation, forming an optically inactive charge state [?, ?, ?]. Therefore the emitters change between states of higher and lower emission, i.e. brighter and darker states, called blinking levels.

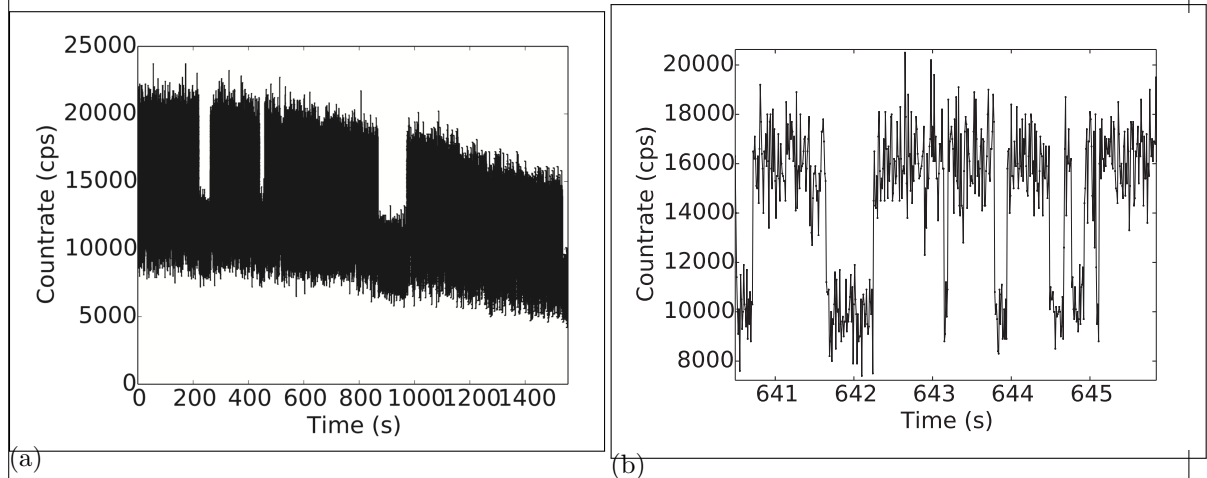


Figure 6.11: (a) Time trace of the single emitter H1, which exhibits strong blinking. The variation of the count rate in the upper state is attributed to a drift of the setup. (b) Detail of the time trace of the same emitter.

The photon count time trace of emitter H1 is shown in Figure 6.11. In the overview picture (Figure 6.11a), a few blinking dips can be seen with time intervals of up to a few minutes. The fact that the count rate never drops down to the dark count rate lets us assume, that there are at least two SiV centers present, one exhibiting fluorescence intermittence and

one exhibiting a stable emission. When zooming in, shorter time intervals are observable (Figure 6.11b). The time intervals range from a few tens of milliseconds up to a few seconds with a few outliers exhibiting very long time intervals up to a few hundred seconds. The bright and dark times exhibit different probability distribution functions and with that, different characteristic time constants. In Figure 6.12 the time intervals of the emitter are shown as small vertical dashed red lines and solid blue lines for the bright and dark state respectively.

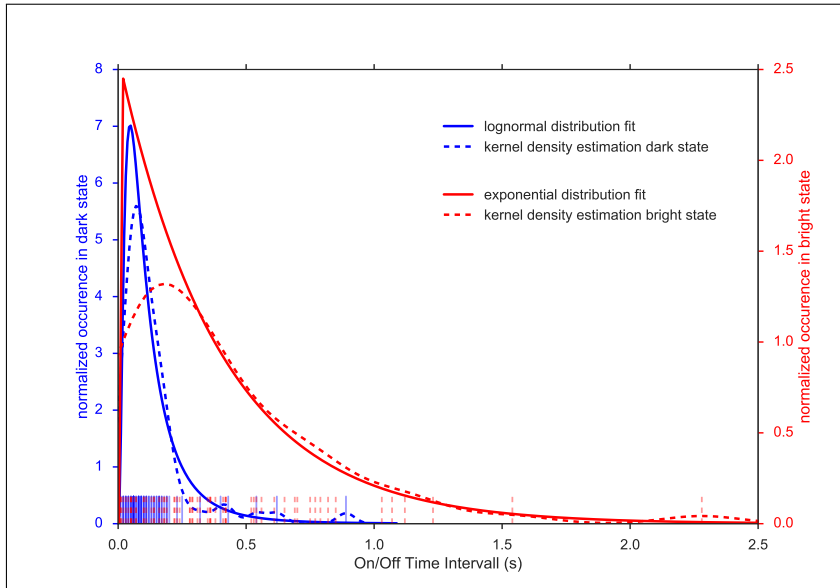


Figure 6.12: Time intervals of the single emitter exhibiting the highest blinking rate in the bright (red) and dark (blue) states. Each flank of the blinking state was individually read out from the photoluminescence time trace. On the horizontal axis small vertical lines represent the individual data points of the bright/dark time intervals. The blue and red dashed curves represent kernel density estimations of the distribution of time intervals of the dark and bright states, respectively. The y-axis is scaled to the normalized kernel density estimate. The red solid line is an exponential fit of the bright state time intervals whereas the blue solid line is a log-normal fit of the dark state time intervals. These fitting functions were chosen because they provide the best agreement with the data using a Kolmogorov-Smirnov test with respect to other functions (p-values: bright state (red) 0.92, dark state (blue) 0.77).

Outliers with very long time intervals are omitted here. The dashed lines are kernel density estimators of the distribution of the respective time intervals. This implies that every data point is represented with a Gaussian function and the resulting functions are added up to model the whole data. The red solid line is an exponential fit of the distribution of time intervals in the bright state. The high p-value of 0.92 confirms the goodness of the fit. The median time interval in the bright state obtained by the exponential fit amounts to 0.09 s. While other literature about solid state quantum emitters reports an exponential probability distribution for both time intervals in bright and dark states[?, ?], we found a log-normal probability distribution for the time interval in the dark state. The solid blue line in Figure 6.12 is a log-normal fit of the distribution of the time intervals in the dark state. A Kolmogorov-Smirnov test yields a p-value of 0.77 for the log-normal fit and is by far the best model to describe the data distribution. For comparison: The p-value of an exponential

fit amounts to 0.36. The median time interval in the dark state obtained by the log-normal fit is determined as 0.10 s, therefore being close to the median time interval in the bright state. Very long time intervals are not shown in the plot for better visualization of the small timescales, however these long time intervals are included in the fit. The longest measured time interval amounted to 41.14 s and occurred in the dark state.

Measurements of blinking time intervals in [?] and [?] report time intervals between about 0.03 s to 1 s, and 0.1 s to 2 min, respectively. These findings are in good agreement with our measurements.

In general, excitation and emission process is mediated by charge separation (i.e. excitons). If an electron or hole is localized far enough that there is sufficiently negligible overlap with the wave function of the remaining carrier, blinking occurs [?]. We explain the observed blinking as a manifestation of the local crystal disorder due to dislocations and impurities which act as a trap for the excited electron and therefore switch the emitter to the dark state. The capture of the electron of the exciton by traps due to local crystal disorders may inhibit recombination and therefore induce the dark state [?]. The assumption that dislocations and impurities are responsible for blinking emitters is in agreement with our findings reported in ??.

Research of blinking rhodamine molecules confirms power law distributed bright state times and log-normal distributed dark state times [?]. The log-normal distribution is explained by a Gaussian distribution of activation barriers of the electron transfer to trap states in the surrounding material [?]. It hints towards a recapture of the electron via multiphonon relaxation channels.

## Chapter 7

# Coupling Nanodiamonds to Photonic Structures

In the last chapter, we saw that the spectroscopic properties of SiV centers vary strongly among individual nanodiamonds. Nanodiamonds are further implemented in photonic structures for the application in metrology as well as in quantum cryptography or quantum computing. Therefore, it is important to have a good knowledge of the spectroscopic properties of the individual SiV center. A preselection of nanodiamonds including an SiV center with optimal properties is performed. These properties contain both spectroscopic parameters as well as technical parameters for the pick-and-place process. Spectroscopic parameters contain narrow linewidth, high countrates and single photon emission, the technical parameters include a size of the nanodiamonds hosting the SiV center bigger than 70 nm and how isolated they lie on the substrate surface. The selected nanodiamond is then transferred to a target structure. In the scope of this thesis, nanodiamonds including SiV centers were coupled to two different kinds of structures:

- Vertical-Cavity Surface Emitting Lasers: The aim is to create a hybrid-integrated single photon source, where an electric current is employed to create single photons. The diamond containing an SiV center is placed directly on the beam output. Hence the SiV center is directly pumped by the laser beam. This system is interesting for metrological applications, as it is the major building block for a portable device ready to calibrate single photon detectors.
- Plasmonic Nanoantennas: The aim is to enhance photoluminescence intensity. As described in previous chapters, not only ZPL position and linewidth, but also the photoluminescence intensity varies strongly among individual SiV centers. However, in metrology a photon flux rate high enough to be measured by a low optical flux detector is needed [?]. This increase in intensity is achieved by coupling the SiV centers in nanodiamonds to plasmonic antennas.

think  
of other  
word

### 7.1 Additional Experimental Methods

To couple nanodiamonds to photonic structures, we pursued several different methods:

1. Directly spin-coat the structures with a nanodiamond solution and consecutively look for a structure containing a nanodiamonds with an SiV center exhibiting the desired spectroscopic properties. This method was tried with the antenna structures, as there are many antenna structures on one substrate (see Figure 7.12a), therefore there is a chance that a suited nanodiamond is incidentally ends up at the right spot. However, it is not suitable for the VCSELs, first because of the morphology of the VCSELs and secondly, because there is a very limited number of VCSELs on one substrate.
2. Use an iridium substrate covered with nanodiamonds containing SiV centers, look for a suited nanodiamond and transfer it with a pick-and-place technique using a nanomanipulator. The nanomanipulator is essentially a thin tip in a scanning electron microscopy. The iridium substrate is preprocessed with markers, to record the position of the preselected nanodiamond. The huge advantage is that the very best suited nanodiamond can be preselected. However, disadvantages of this process include the electron radiation during the pick-and-place process, which might affect SiV center fluorescence light and the further restriction that the nanodiamonds must be big enough to be picked up with the nanomanipulator.
3. Similar to method 2, however the transfer is performed with an atomic force microscope. While this method has the advantage that the nanodiamonds are not irradiated with electrons, the disadvantage is that it is not possible to observe the picking process in real time. The area of the preselected nanodiamond has to be scanned after every pick-up try, which is very time consuming and therefore was not further pursued after some trials.

In the following paragraphs, the pick-and-place technique of method 2 is described in more detail. It is the coupling method most extensively deployed in the scope of this thesis and requires a range of experimental setups. The pick-and-place process was carried out with major help from C. Pauly, group of xxx Mücklich, Saarland University. The nanomanipulator setup was provided by the same group.

### 7.1.1 Nanomanipulator

In general, nanomanipulator is a tip mounted inside an SEM, allowing manipulation and visualization of the manipulation process at the same time. The one used for our experiments was built by the company Kleindiek (model MM3A-EM) and has a changeable tungsten tip (see Figure 7.1b). It is mounted inside a Thermo Scientific™ Helios NanoLab™ DualBeam™ microscope, which combines a focussed ion beam and an electron microscope. The bent nanomanipulator tip has 3 degrees of freedom: up/down and left/right both in an arc up to 240° and 12 mm in/out (see arrows in Figure 7.1b). Before nanomanipulation the tip was "sharpened" with the focussed ion beam by etching away tungsten with gallium ions. This sharpening was performed to meet the size criteria necessary to pick up the nanodiamonds. In Figure 7.3a the sharpened tip is shown (the radius of curvature amounts to 100 nm). The small tip sticking out of the bigger cone is the sharp tip used for pick-and-place.

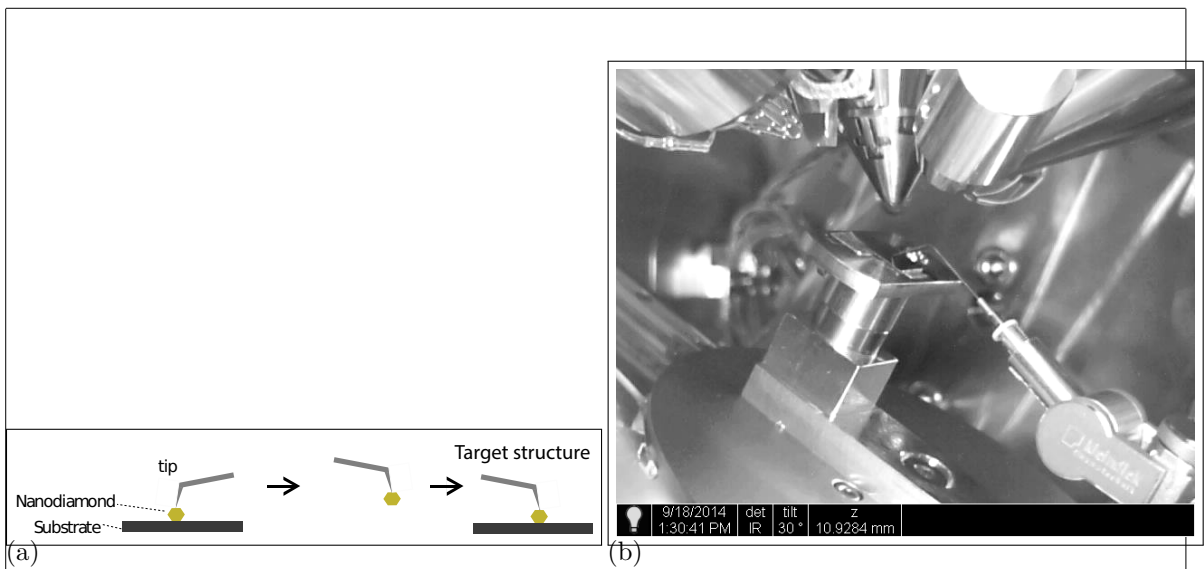


Figure 7.1: (a) Sketch of the pick-and-place process exploiting a nanomanipulator. (b) Image of the nanomanipulator mounted in the FIB. The arrows indicate the degrees of freedom of motion of the nanomanipulator. The custom made workbench is situated in the middle of the picture. On top of it, there is a  $1\text{ cm}^2$  substrate with coated nanodiamonds, the nanomanipulator tip pointing to the middle of it. Behind it, there is the target vertical-cavity surface emitting laser. Perpendicular to the workbench, the objective of the electron microscope can be seen. The pointier cone perpendicular to the image top image edge is the objective of the focussed ion beam.

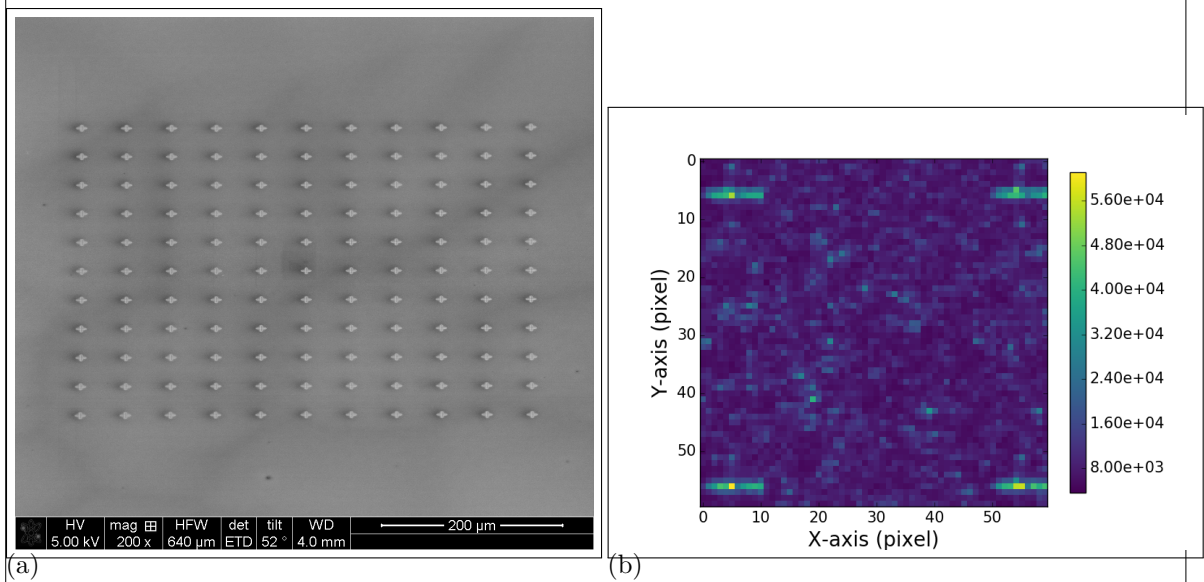


Figure 7.2: (a) Overview of a field of cross markers. The field spans  $0.5 \times 0.5 \text{ mm}$  (b) White light scan of an area with a cross marker in all four corners.

### 7.1.2 Determination of The Position of Nanodiamonds

An nanodiamond pre-characterized in the confocal setup exhibiting the preferred spectroscopic properties has to be found again in the SEM setup where the nanomanipulator is installed. Therefore, we milled cross markers into the iridium coating of the silicon substrate using the focussed ion beam prior to spin-coating the substrate with nanodiamond solution. The crosses' size is  $10 \times 10 \mu\text{m}^2$  are exhibit a nominal depth of 40 nm. Four crosses are the cornerpoints of a  $50 \times 50 \mu\text{m}^2$  square. The  $10 \times 10$  crosses spaned one field of crosses; we usually put 3 fields of crosses on one substrate.

To record the position of a nanodiamond with respect to a cross marker, we used two different methods:

- Scanning the sample in the confocal setup while a white light source illuminates the sample from the side in an acute angle. The edges of the cross markers are visible in the fluorescence scan. After turning the white light lamp off, the same area is scanned once more to record the fluorescence from the SiV centers. An overlay of the two images identifies the position of fluorescent SiV centers with respect to the cross markers. The disadvantage of this method is, that it takes a lot of time, as every scan has to be performed twice. Also, as only fluorescence light scans are performed, no information of the nanodiamonds is accessible. Such information comprises of the size of the individual nanodiamonds and whether the nanodiamonds lie isolated on the substrate surface. These parameters are only available during the pick-and-place process in the SEM. An emitter with optimal optical properties can turn out not to be suited for pick-and-place just before the process itself, hence the time spent to optically characterize an emitter was in vain.
- A more efficient method is scanning the substrate first in a commercial laser scanning microscope . The laser scanning microscope is a confocal microscope where the focus of a laser is used to obtain the height of a structure. It is possible to scan a whole field of cross markers in several minutes. The obtained image is a greyscale image, where the greyscale corresponds to the height deviation of a structure. Therefore, both the crosses and the nanodiamonds appear in darker shades of grey. So in contrast to the previous method, information on the size and isolation of the nanodiamonds is accessible. After scanning the substrate with the laser scanning microscope, it is put into the confocal setup. While observing the surface with the CCD camera (Figure 7.16), a specific cross marker is chosen as the starting point of a fluorescence light scan. Comparing the laser scanning microscope image and a fluorescence light scan, fluorescent dots of the fluorescence light scan are attributed to nanodiamonds in the laser scanning microscope scan (see Figures 7.11a and 7.11b).

fib pa-  
rameter

put in  
a pic of  
white-  
lightscan

specs

verify  
info

### 7.1.3 The Pick-And-Place Process

After we identified nanodiamonds as well-suited for transfer to the target structure, both the substrate with the nanodiamonds and the target structure were mounted inside the SEM. The process was performed using a high resolution mode with a low acceleration voltage of the SEM of 1 keV and a current of 1.7 nA. The tip is approached to the pre-selected nanodiamond from above. As the SEM objective is mounted above the nanomanipulator, the proximity the nanomanipulator tip to the nanodiamond is not observable. The proximity is

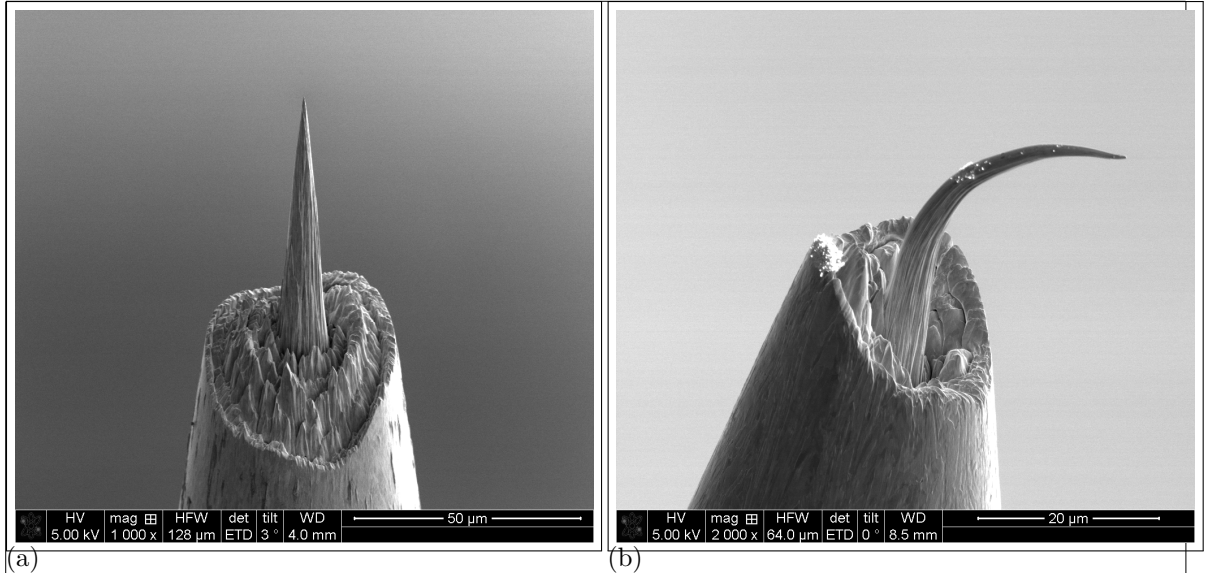


Figure 7.3

indirectly estimated by the shadow the tip casts onto the substrate and the focus. The first method is used for the coarse approachment of the tip to the nanodiamond: The closer the tip gets to the nanodiamond, the closer the shadow of the tip coincides with the nanodiamond position. Exploiting the focus as an estimate for the proximity of the tip is used for fine adjustment during the last stage of the approachment. This is done as follows: At the end of the coarse movement, the tip of the nanomanipulator is still some distance above the nanodiamond. The SEM is focused on the nanodiamond, therefore the nanomanipulator tip is out of focus and appears blurry. As the tip is approached, it moves further and further into focus, its image becoming sharper, until the it touches the nanodiamond. As this is a tricky process, sometimes the tip was approached with too much force and was destroyed in the process (Figure 7.3b).

When performed correctly, due to adhesion, the nanodiamond sticks to the nanomanipulator tip when the both get in contact (Figure 7.14a). The nanomanipulator is then moved to the target structure and the same approachment procedure is applied. Dependent on the material of the target structure, the nanodiamond either sticks to the structure right away due to higher adhesion forces between the nanodiamond and the structure (as is the case for the golden plasmonic antennas). Or the nanodiamond has to be "wiped off" of the nanomanipulator tip in a sideways motion. In either way it is possible to place the nanodiamond within a precision of a few nanometers.

## 7.2 Coupling SiV centers to Vertical-Cavity Surface Emitting Lasers

For metrology, the photon flux rate has to be high enough to be measured by a low optical flux detector [?].

The red AlGaInP-based oxide-confined vertical-cavity surface emitting lasers (VCSEL) are

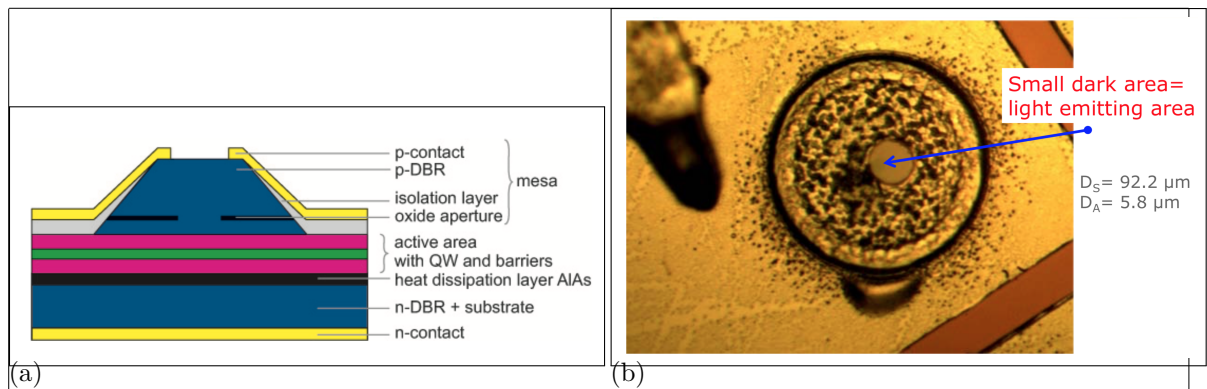


Figure 7.4: (a) Sketch of the VCSEL showing the different layers.

ask how to cite

(b) Image of the VCSEL. The circle with the black dots is the hole in the p-contact (diameter  $D_S$ , the smaller darker area in the middle is the laser output area (diameter  $D_A$ )

compact and perfect candidates for excitation of SiV centers in a hybrid integrated single photon source: They exhibit wavelengths around 650 nm at continuous wave emission. SiV centers exhibit intensity maxima at an excitation at 670 nm and 690 nm [1]. In addition, VCSELs exhibit circular beam profile, have low divergence angle and emit linearly polarized light.

diagram  
einfuegen

### 7.2.1 Vertical-Cavity Surface Emitting Laser Structure

The VCSEL structure (??) consists of an active region between two distributed Bragg reflectors (DBR). The bottom n-type DBR is made of 50 pairs of AlAs/Al<sub>0.5</sub>Ga<sub>0.5</sub>As, the p-type DBR consists of 36 Al<sub>0.95</sub>Ga<sub>0.05</sub>As/Al<sub>0.5</sub>Ga<sub>0.5</sub>As mirror pairs [?]. The active region consists of four GaInP quantum wells (QW). An oxide aperture in a field node of the standing wave serves as a spatial filter for maximum modal gain by confining the current and the optical mode. The active diameter which is defined by the oxide aperture amounts to 5.8 μm. As this region is the area where the laser emission exits the VCSEL, the nanodiamonds have to be put within this area. The used VCSEL exhibits an optical output power up to 1 mW with low threshold current of up to 3 mA at about 655 nm.

ist das  
up to

nachdenke  
wie for-  
mulierung  
richtig  
ist

was it  
single?

### 7.2.2 SiV center in a Vertical-Cavity Surface Emitting Laser

As diamond material we used CVD grown nanodiamonds. They had been grown on an iridium coated silicon wafer (see ??). These nanodiamonds exhibit a nominal size of 200 nm. First, we selected a nanodiamond which exhibited one dominant line at 746.0 nm with a linewidth of 1.9 nm. Consecutively, its position on the substrate was determined using a white light laser scan as described in ?? . It was then transferred to the VCSEL Bm4 described in ?? . After a successful transfer of the pre-selected nanodiamond onto the active area of VCSEL Bm4, the VCSEL was put in the confocal setup. Using the laser from the confocal setup we checked if the pick-and-place process caused any modification of the spectroscopic properties of the SiV center such as a decrease of countrate or a modification of the fluorescence light spectrum. For this, the VCSEL itself was not operated itself. First, the VCSEL surface was

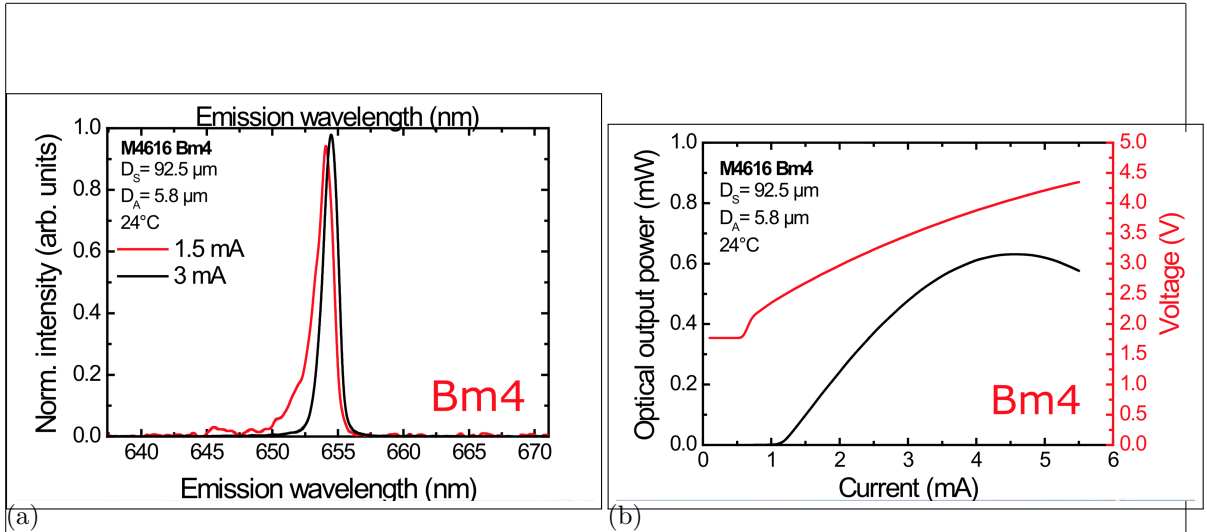


Figure 7.5: (a) Emission spectrum of the used VCSEL at two different currents. (b) Optical output power and voltage of the same VCSEL in dependence of input current. []

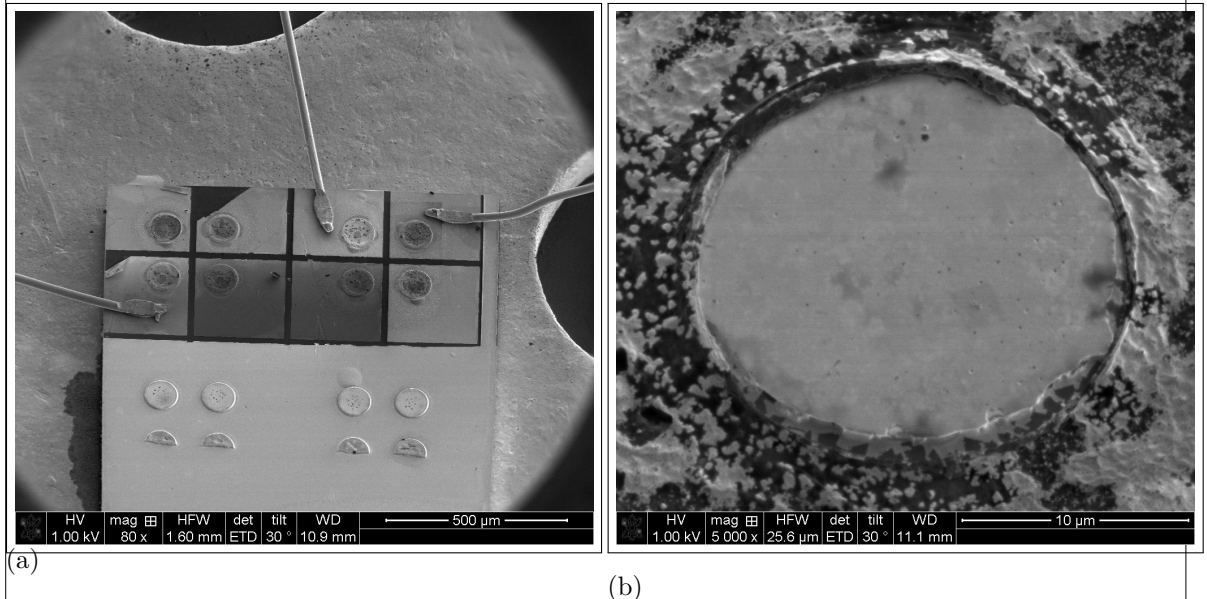


Figure 7.6: (a) SEM image of an array of VCSELs. The three wires are the anodes, which are connected to the top layer (p-contact) of the VCSEL. Therefore, three of the VCSEL structures can be operated. (b) Detail SEM image of the top of the exploited VCSEL Bm4. The circular middle part is the hole in the p-contact through which the top DBR is visible. The active diameter is smaller than that and not visible in the SEM.

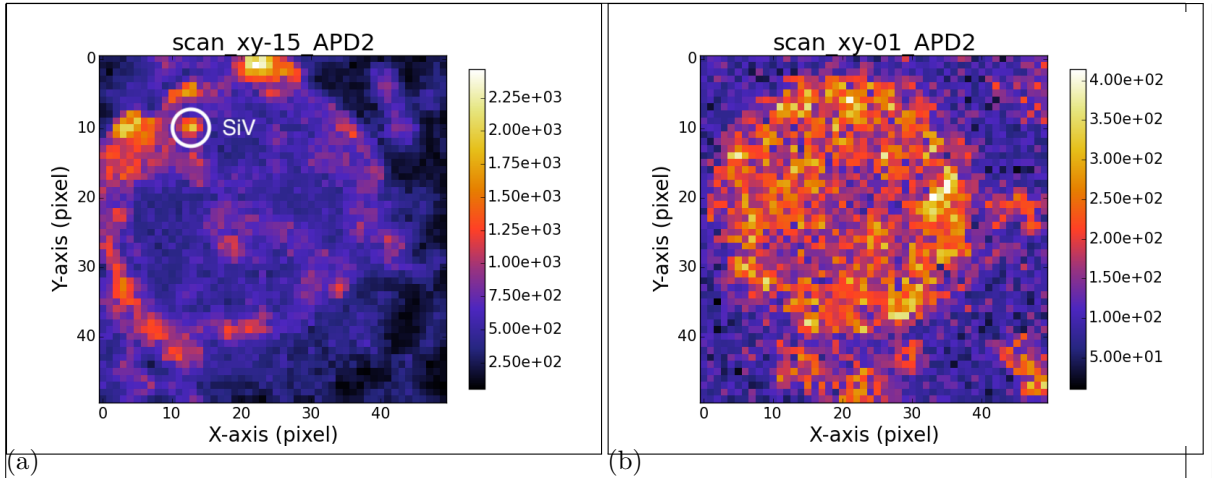


Figure 7.7: (a) Scan of the VCSEL Bm4 with coupled nanodiamond under excitation with the laser from the confocal setup. The big visible ring is the edge of the circular hole in the p-contact. The bright spot in the upper left corner corresponds to the transferred nanodiamond containing an SiV center. (b) Scan of the VCSEL Bm2 without nanodiamond under excitation with the laser from the confocal setup. The circular hole in the p-contact exhibits a constant countrate.

scanned Figure 7.7a. . A bright dot exhibiting a countrate of a few thousand counts per second is visible where the nanodiamond containing an SiV was put. A comparative scan of a VCSEL without nanodiamond only exhibits a background countrate, as expected (Figure 7.7b).

The spectrum of the SiV center in the transferred nanodiamond was investigated before and after the pick-and-place process (Figure 7.8). The original spectrum before nanodiamond transfer exhibits a sharp line at 746.0 nm (denoted line A). After the pick-and-place process, this line is still there, albeit with a low intensity. Another line at 0 nm (denoted line B) which was a minor feature in the spectrum before pick-and-place, is the predominant line after the process. This modification of the spectrum is caused by a reduction of the intensity of line A and constant intensity of line B. The reduction of the intensity of line A may be caused by damage of the color center due to electron radiation. While the energy of the electrons is low compared to the ionization energy of the color center , we observed a reduction of fluorescence light intensity after electron radiation .

check  
number

numbers

put alex  
meyers  
observations in  
appendix

besser  
begruen-  
den, was  
passiert

## 7.3 Coupling Nanodiamonds to Double Bowtie Antenna Structures

### 7.3.1 Nanodiamond With Multiple SiV centers Coupled to Antenna

### 7.3.2 Nanodiamond With Single SiV center Coupled to Antenna

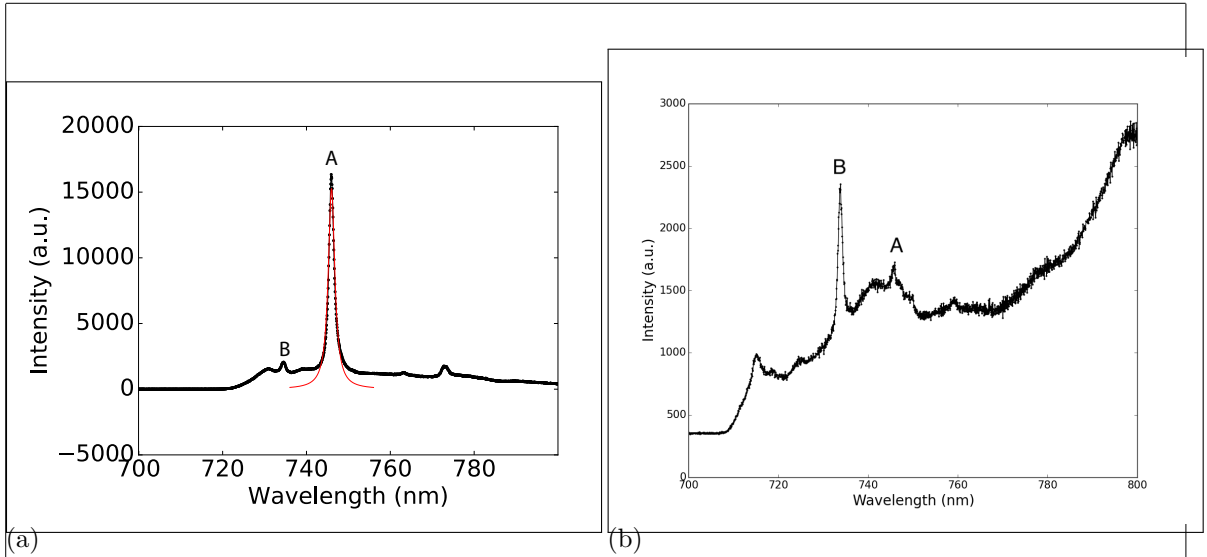


Figure 7.8: (a) Spectrum of the preselected diamond for transfer onto VCSEL Bm4 before pick-and-place. The strong line denoted A exhibits a center wavelength of 746.0 nm and a linewidth of 1.9 nm. Line B exhibits a center wavelength of 0 nm and a linewidth of 0 nm  
put in correct numbers

(b) Spectrum of the same SiV center after pick-and-place, excited with the same laser as before. While Line A is almost gone, line B still exists and is the predominant line of the spectrum. Note: different longpass filters were used for the two measurements. Measurement (a) was performed with a 720 nm longpass filter, measurement (b) with a 710 nm longpass filter.

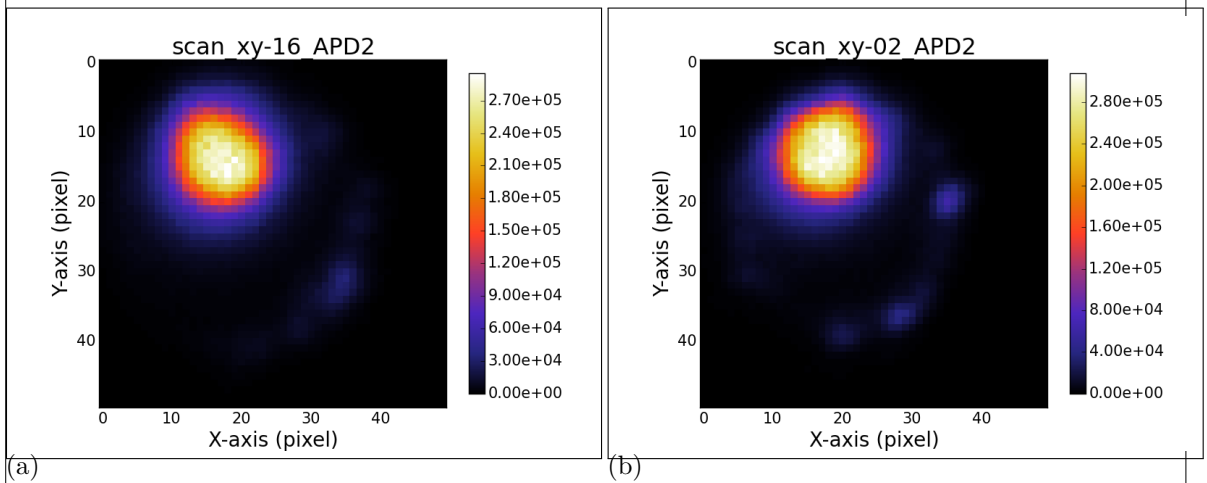


Figure 7.9: (a) Scan of the laser light stemming from the VCSEL Bm4 and the fluorescence light from the SiV center in the filter window 730 nm to 750 nm. (b) Scan of the laser light stemming from the VCSEL Bm2 without coupled SiV center. The outcome of the two scans is almost identical.

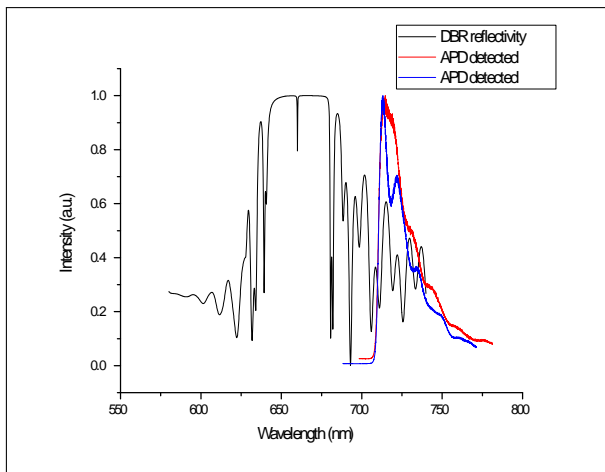
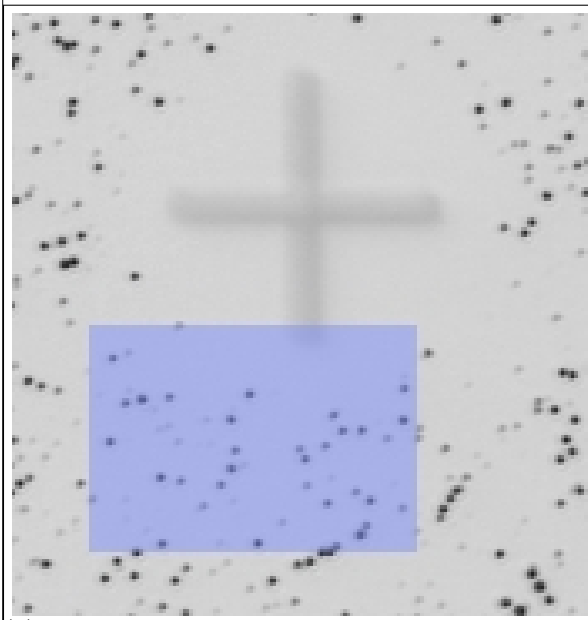
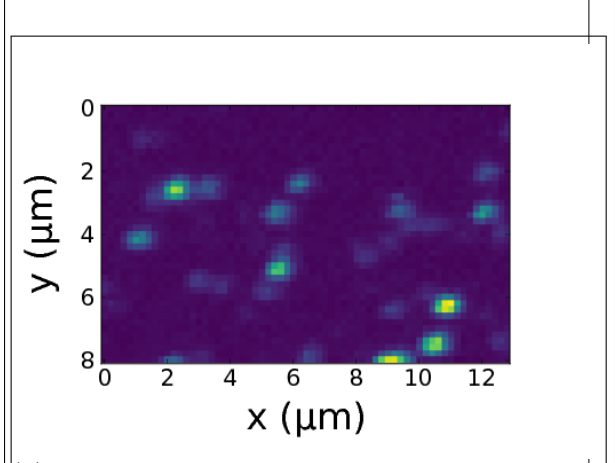


Figure 7.10: Reflectivity of the Distributed Bragg reflector (DBR) of the VCSEL, and spectrum of the SiV center measured during VCSEL excitation. The reflectivity of the DBR and the VCSEL emission spectra are depicted with different scales. The shape of the measurement of the SiV center during VCSEL operation coincides with the shape of the DBR reflectivity. The spectrum of the SiV center is not visible. As the emission from the SiV center is small compared to the intensity of the laser sideband in the same wavelength regime, the SiV centers emission is not detectable.



(a) Picture recorded with a commercial high resolution laser scanning microscope. The area shaded in blue represents the photoluminescence scan in image b)



(b) Photoluminescence scan of a  $8 \mu\text{m} \times 13 \mu\text{m}$

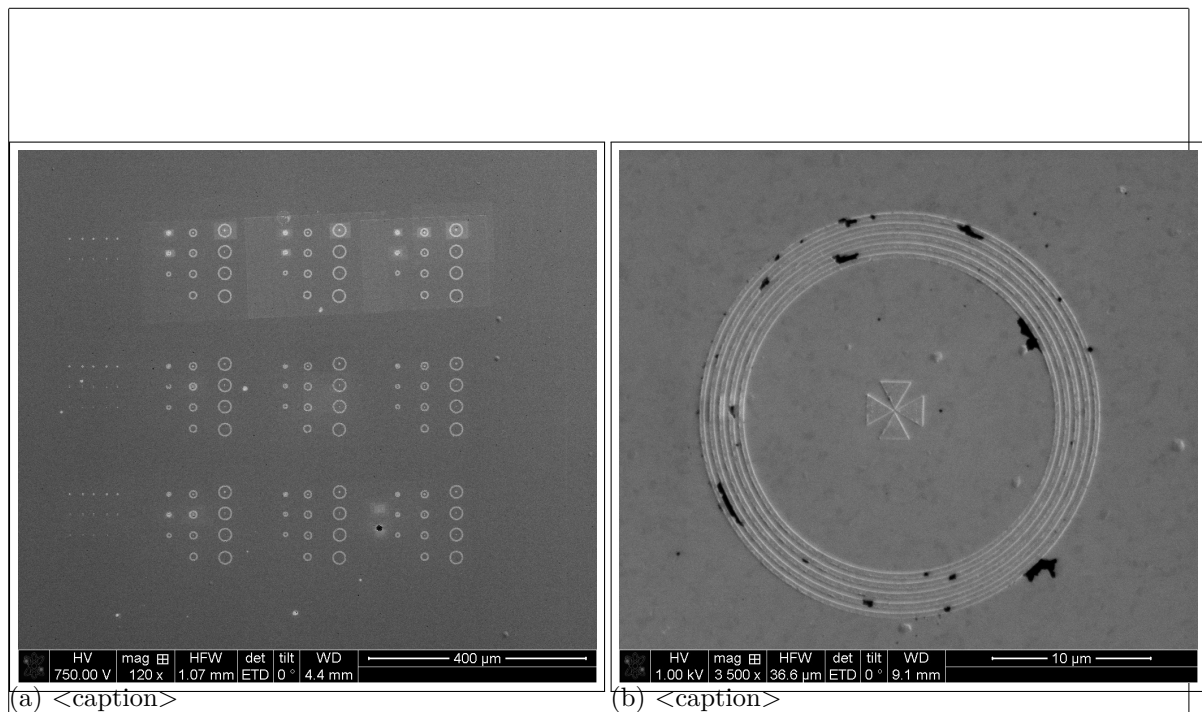


Figure 7.12: &lt;caption&gt;

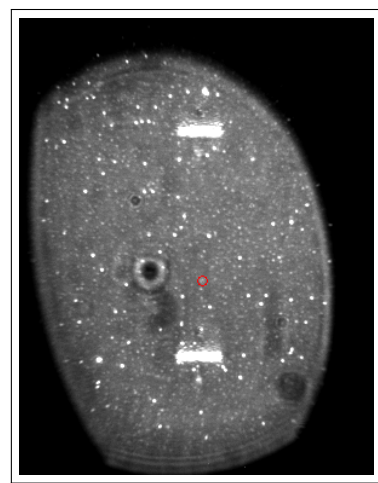


Figure 7.13: &lt;caption&gt;

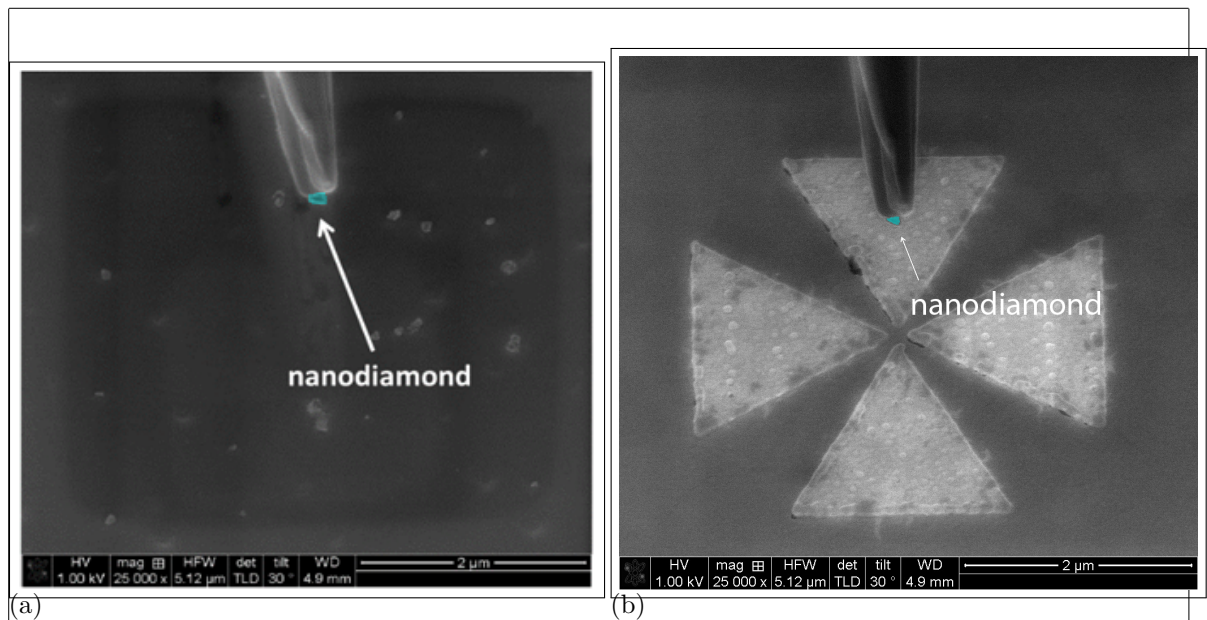


Figure 7.14

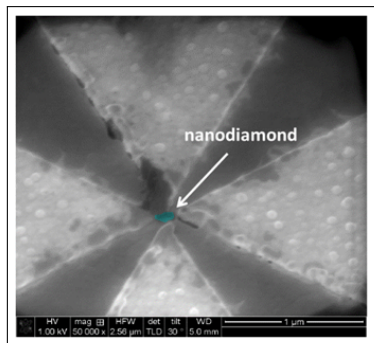


Figure 7.15: &lt;caption&gt;

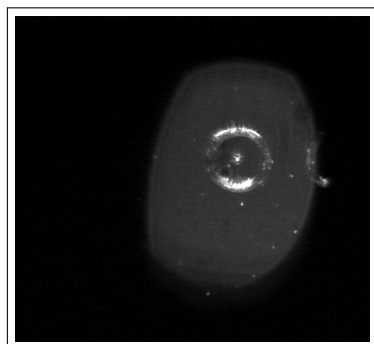


Figure 7.16: &lt;caption&gt;

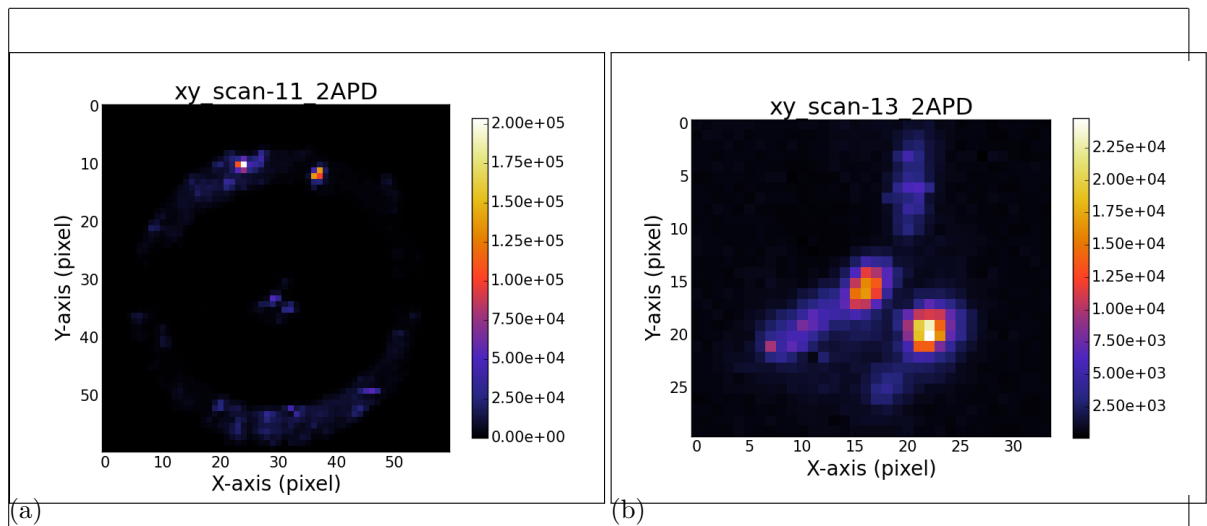


Figure 7.17: &lt;caption&gt;

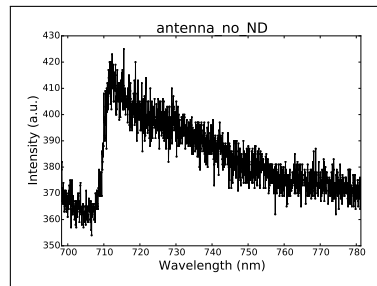


Figure 7.18: &lt;caption&gt;

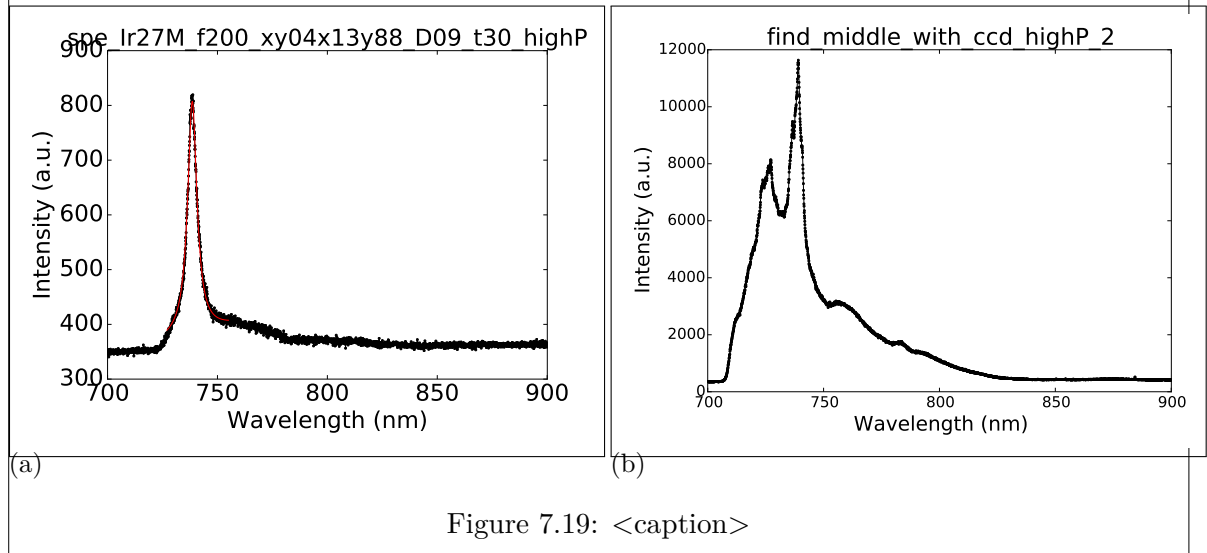


Figure 7.19: &lt;caption&gt;

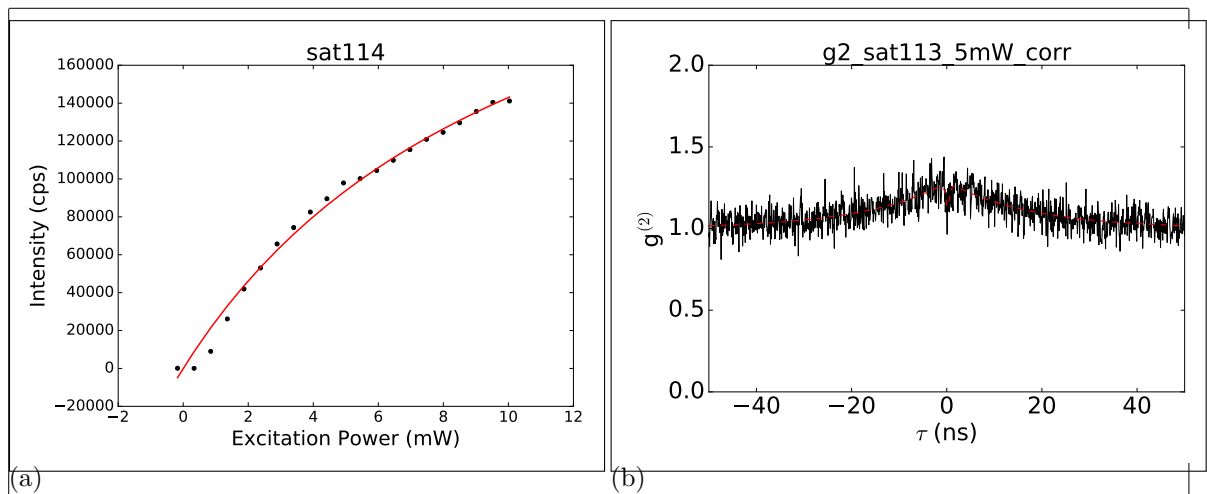


Figure 7.20: &lt;caption&gt;

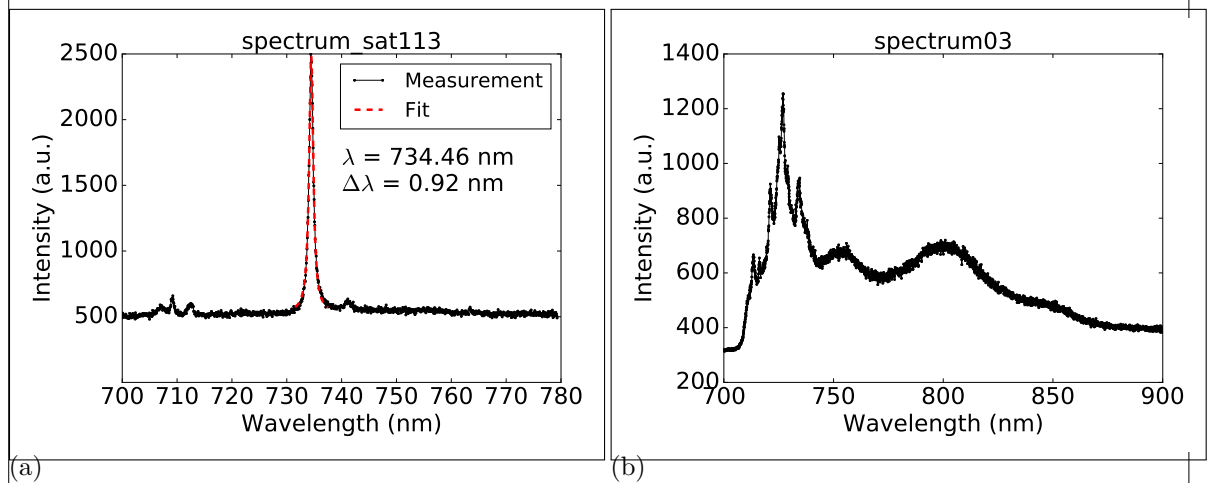


Figure 7.21: &lt;caption&gt;

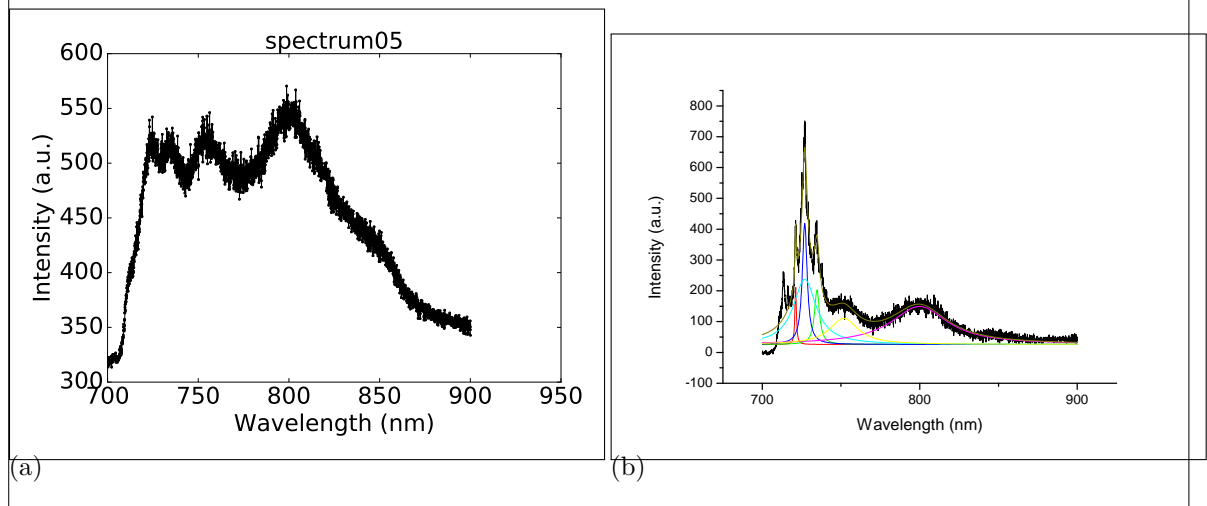


Figure 7.22: &lt;caption&gt;

---

---

## Summary and Conclusions

In conclusion we found a strongly inhomogeneous distribution of SiV center spectra in nanodiamonds. We group the zero-phonon-lines into two groups: Group H consists of ZPLs exhibiting a narrow linewidth from below 1 nm up to 4 nm and a broad distribution of center wavelength between 710 nm and 840 nm. Compared to that, group V comprises ZPLs with a broad linewidth between just below 5 nm and 17 nm and center wavelength ranging from 730 nm to 742 nm. This data is consistent with previously measured SiV spectra [?, ?]. For comparison, an SiV center in unstrained bulk diamond exhibits a linewidth of 4 nm to 5 nm at a center wavelength of 737.2 nm[?, ?]. We show that both the observed blue-shift and the observed red-shift of group V are consistently explained by strain in the diamond lattice. Further, we suggest, that group H might be comprised of modified SiV centers, the structure of which is currently unclear.

We investigated the SiV sidebands: In group V we found one prominent peak at a shift of 42 meV, which corresponds to a well-known feature assigned to non-localized lattice vibrations [?, ?]. In group H we see an accumulation of peaks, at around 43 meV, 64 meV, 150 meV and 175 meV, which are consistent with sideband peaks reported in [?, ?, ?].

We further reported photon autocorrelation measurements which verified the existence of single SiV centers both in group H and group V. Investigating the time trace of the SiV center photoluminescence, we found that some SiV centers exhibit fluorescence intermittence with on times between several microseconds up to 41 s. Furthermore, we see an exponential distribution of bright time intervals and a log-normal distribution of dark time intervals, consistent with research on single molecules [?]. In terms of photostability, there is a big difference between group V and group H: All but one emitters in group H exhibit blinking, where only one of the emitters in group V exhibits blinking.

adding momentum towards the adoption of the quantum candela ...

---

---

# Index

$g^{(2)}$  function, 18

Hanbury Brown and Twiss setup, **18**

intensity autocorrelation function, 18